Development and calibration of semiconductor detectors for dark matter searches

By

VIJAY JANARDHAN IYER

PHYS11201304009

National Institute of Science Education and Research, Bhubaneswar

A thesis submitted
to the Board of Studies in
Physical sciences

In partial fulfillment of requirements
For the Degree of

DOCTOR OF PHILOSOPHY
of

HOMI BHABHA NATIONAL INSTITUTE

July, 2021

ii

Homi Bhabha National Institute
Recommendations of the Viva Voce Committee

As members of the Viva Voce Committee, we certify that we have read the dissertation prepared by **Vijay Janardhan Iyer** entitled **"Development and calibration of semiconductor detectors for dark matter searches"** and recommend that it may be accepted as fulfilling the thesis requirement for the award of Degree of Doctor of Philosophy.

Chairman - Dr. Sanjay Kumar Swain   Date: 05/10/2021

Guide / Convener - Dr. Bedangadas Mohanty   Date: 05/10/2021

Co-guide - Dr. Kartikeswar Senapati   Date: 05/10/2021

External examiner - Dr. Bharatendu Singh   Date: 5/10/2021

Member 1 - Dr. Nishikanta Khandai   Date: 05/10/2021

Member 2 - Dr. Victor Roy   Date: 05.10.21

External Member - Dr. Seema Bahinipati   Date: 5/10/202

Final approval and acceptance of this thesis is contingent upon the candidate's submission of the final copies of the thesis to HBNI.

I hereby certify that I have read this thesis prepared under my direction and recommend that it may be accepted as fulfilling the thesis requirement.

Date : October 5, 2021
Place : NISER, Jatni

(Co-guide) 05/10/2021   (Guide) 05/10/2021

iv

STATEMENT BY THE AUTHOR

This dissertation has been submitted in partial fulfillment of requirements for an advanced degree at Homi Bhabha National Institute (HBNI) and is deposited in the library to be made available to borrowers under rules of the HBNI.

Brief quotations from this dissertation are allowable without special permission, provided that accurate acknowledgement of source is made. Requests for permission for extended quotation from or reproduction of this manuscript in whole or in part may be granted by the Competent Authority of HBNI when in his or her judgment the proposed use of the material is in the interests of scholarship. In all other instances, however, permission must be obtained from the author.

Date : October 5, 2021

Place : NISER, Jatni

(VIJAY JANARDHAN IYER)

DECLARATION

I hereby declare that the investigation presented in the thesis has been carried out by me. The work is original and has not been submitted earlier as a whole or in part for a degree/diploma at this or any other Institution/University.

Date : October 5, 2021

Place : NISER, Jatni

(VIJAY JANARDHAN IYER)

List of publications and presentations

Journal

Papers published as primary author

[1] V. Iyer et al. "Large mass single electron resolution detector for dark matter and neutrino elastic interaction searches". *Nuclear Instruments and Methods in Physics Research Section A: Accelerators, Spectrometers, Detectors and Associated Equipment* 1010 (2021), p. 165489. ISSN: 0168-9002.

Papers communicated to journal (as primary author)

[1] M. F. Albakry et al. "Ionization yield measurement in a germanium CDMSlite detector using photo-neutron sources" (Feb. 2022). arXiv: 2202.07043 [physics.ins-det].

Papers under collaboration review (as primary contributor)

[1] M. Chaudhuri et al. *A novel active veto prototype detector with an inner target for improved rare event searches*. 2022.

Other Publications

[1] I. Alkhatib et al. "Constraints on Lightly Ionizing Particles from CDMSlite". *Phys. Rev. Lett.* 127 (8 Aug. 2021), p. 081802.

[2] I. Alkhatib et al. "Light Dark Matter Search with a High-Resolution Athermal Phonon Detector Operated above Ground". *Phys. Rev. Lett.* 127 (6 Aug. 2021), p. 061801.

[3] D. W. Amaral et al. "Constraints on low-mass, relic dark matter candidates from a surface-operated SuperCDMS single-charge sensitive detector". *Phys. Rev. D* 102.9 (2020), p. 091101. arXiv: 2005.14067 [hep-ex].

[4] T. Aralis et al. "Constraints on dark photons and axionlike particles from the Super-CDMS Soudan experiment". *Phys. Rev. D* 101.5 (2020). [Erratum: Phys.Rev.D 103, 039901 (2021)], p. 052008. arXiv: 1911.11905 [hep-ex].

[5] R. Agnese et al. "Production rate measurement of Tritium and other cosmogenic isotopes in Germanium with CDMSlite". *Astroparticle Physics* 104 (2019), pp. 1–12. ISSN: 0927-6505.

[6] R. Agnese et al. "Search for Low-Mass Dark Matter with CDMSlite Using a Profile Likelihood Fit". *Phys. Rev. D* 99.6 (2019), p. 062001. arXiv: 1808.09098 [astro-ph.CO].

[7] R. Agnese et al. "Energy Loss Due to Defect Formation from ^{206}Pb Recoils in SuperCDMS Germanium Detectors". *Appl. Phys. Lett.* 113.9 (2018), p. 092101. arXiv: 1805.09942 [physics.ins-det].

[8] R. Agnese et al. "First Dark Matter Constraints from a SuperCDMS Single-Charge Sensitive Detector". *Phys. Rev. Lett.* 121.5 (2018). [Erratum: Phys.Rev.Lett. 122, 069901 (2019)], p. 051301. arXiv: 1804.10697 [hep-ex].

[9] R. Agnese et al. "Results from the Super Cryogenic Dark Matter Search Experiment at Soudan". *Phys. Rev. Lett.* 120.6 (2018), p. 061802. arXiv: 1708.08869 [hep-ex].

[10] R. Agnese et al. "Low-mass dark matter search with CDMSlite". *Phys. Rev. D* 97.2 (2018), p. 022002. arXiv: 1707.01632 [astro-ph.CO].

[11] G. Agnolet et al. "Background Studies for the MINER Coherent Neutrino Scattering Reactor Experiment". *Nucl. Instrum. Meth. A* 853 (2017), pp. 53–60. arXiv: 1609.02066 [physics.ins-det].

[12] R. Agnese et al. "Projected Sensitivity of the SuperCDMS SNOLAB experiment". *Phys. Rev. D* 95.8 (2017), p. 082002. arXiv: 1610.00006 [physics.ins-det].

Conference/Symposium

[1] V. Iyer (for MINER collaboration). "Large mass single electron resolution detector for dark matter and coherent neutrino-nucleus elastic interaction searches". In: *XXIV DAE-BRNS High Energy Physics Symposium*. NISER, Jatni, India, 2020.

[2] V. Iyer (for SuperCDMS collaboration). "SuperCDMS SNOLAB". In: *Advances in Astroparticle Physics and Cosmology*. SINP, Kolkata, India, 2020.

[3]   V. Iyer (for SuperCDMS collaboration). "Photo-neutron calibration of SuperCDMS detectors". In: *Proceedings, 64th DAE-BRNS Symposium on Nuclear Physics*. Vol. 64. Lucknow University, Lucknow, India, 2019, pp. 590–591.

[4]   V. Iyer (for SuperCDMS collaboration). "Photo-Neutron Calibration of SuperCDMS Detectors". In: *XXIII DAE High Energy Physics Symposium*. Ed. by Prafulla Kumar Behera et al. IIT Madras, Chennai, India: Springer Singapore, 2021.

[5]   V. Iyer (for SuperCDMS collaboration). "Photo-neutron calibration of SuperCDMS detectors". In: *62nd DAE-BRNS Symposium on Nuclear Physics*. Vol. 62. Thapar University, Patiala, India, 2017, pp. 682–683.

[6]   V. Iyer (for SuperCDMS collaboration). "SuperCDMS SNOLAB". In: *Fermilab 50th Anniversary and Users Meet*. Illinois, USA, 2017.

[7]   V. Iyer (for SuperCDMS collaboration). "Photoneutron calibration of SuperCDMS Soudan detectors". In: *APS April Meeting*. Washington, USA, 2017.

Date : 5 October, 2021

Place : NISER, Jatni

(VIJAY JANARDHAN IYER)

DEDICATED TO

All graduate and undergraduate students who soldier on, despite a lack of mental health awareness, and countermeasures to maintain it, in academic institutions

ACKNOWLEDGEMENTS

A Ph.D. is meant to be a journey, which if you survive, transforms you into an independent thinker with the wisdom to help you navigate through arduous circumstances in life with tranquility. During my journey, I received several life lessons, which once I understood, helped me survive. While I have no intentions of discussing them here, let me provide their cruxes in the words of Rocky Balboa, "*The world ain't all sunshine and rainbows. It's a very mean and nasty place, and I don't care how tough you are, it will beat you to your knees and keep you there permanently if you let it. You, me, or nobody is gonna hit as hard as life. But it ain't about how hard you hit. It's about how hard you can get hit and keep moving forward; how much you can take and keep moving forward. That's how winning is done! Now, if you know what you're worth, then go out and get what you're worth. But you gotta be willing to take the hits, and not pointing fingers saying you ain't where you wanna be because of him, or her, or anybody.*"

Contents

Summary

Dark matter (DM) makes up roughly 27% of the mass-energy budget of the Universe. Over the past two decades direct detection DM experiments have repeatedly returned null results for DM particles in the mass range of 1 GeV to 1 TeV for different DM interaction cross sections. This has shifted the focus to sub-GeV mass range for DM particles. The thesis has three main parts, (i) development of a silicon detector for low mass DM searches, (ii) measurement of the ionization yield in germanium detectors used by SuperCDMS experiment, and (iii) understanding the backgrounds from various cosmologically activated isotopes in direct dark matter experiments.

The ideal requirements in semiconductor detectors used for low mass direct DM search experiments is to build large mass (100 g or more) detectors with single electron sensitivity. One of the challenges in designing such detectors has been reducing their leakage current. The thesis will have a discussion on the development of a 100 g silicon high voltage (Si HV) detector made with a contact free (CF) electrode to reduce leakage current. Its signal-to-noise (S/N) performance is studied which shows a significant improvement when compared to previous detectors of similar mass and dimensions due to the CF electrode. The thesis also discusses the single electron baseline resolution achieved by this detector and how it is an ideal candidate for low mass DM search and coherent elastic neutrino nucleus scattering (CEvNS) experiments. The detector is being used in a reactor-based experiment called Mitchell Institute Neurtino Experiment at Reactor (MINER) at Texas A & M University, USA to measure CEvNS from reactor neutrinos.

Direct DM searches work on the principle of an elastic scattering process between a

DM particle and the detector material. In semiconductor materials, the amount of energy transferred during this process to create electron-hole pairs in the detector is quantified by the term ionization yield (IY). A precise understanding of the IY reduces the uncertainty in measurement of recoil energy and hence the mass of the interacting particle. Super Cryogenic Dark Matter Search (SuperCDMS) is a direct dark matter search experiments that made use of germanium detectors at HV (i.e. 70 V). These detectors are called CDMS low ionization threshold energy or CDMSlite in short. In a detector like the Ge CDMSlite, where the signal gain is obtained at the cost of measuring IY on an event by event basis, an IY model has to be used. In this thesis we discuss the analysis of a dedicated calibration run using two photo-neutron sources ^{124}Sb+^{9}Be and ^{88}Y+^{9}Be to measure the IY in germanium CDMSlite detectors at ~50 mK temperature. The analysis will make use of a likelihood method to extract the yield from data. The likelihood method takes three inputs; (i) A neutron energy distribution from GEANT4 simulations, (ii) A background probability distribution function from data, and (iii) a modified data-driven IY model inspired by Lindhard et. al.

The thesis will also have a brief overview on the possible backgrounds in the Super-CDMS SNOLAB experiment. The main contributors to backgrounds will be discussed. Tritium is a major background source for direct low mass DM searches. There will be a discussion on the production rate estimates of ^{3}H, ^{55}Fe, ^{65}Zn, and ^{68}Ge from the second run of the CDMSlite. Overall, the thesis will have 5 chapters. Chapter one will be an introduction to dark matter and emphasize the need for low mass dark matter search. Chapter 2 will discuss the development and characterization of the Si HV detector. Chapter 3 will focus on the ionization yield measurement in SuperCDMS. Chapter 4 will be an overview about the major backgrounds in dark matter searches. And Chapter 5 will be conclusion and outlook.

List of Figures

List of Tables

List of Abbreviations

ATLAS   A Toroidal LHC ApparatuS

BR   Branching Ratio

CDEX   China Dark Matter Experiment

CDMSlite   CDMS Low Ionization Threshold Experiment

CDMS   Cryogenic Dark Matter Search

CDM   Cold Dark Matter

CEνNS   Coherent Elastic Neutrino Nucleus Scattering

CERN   Conseil Européen Pour La Recherche Nucléaire

CF   Contact Free

CMBR   Cosmic Microwave Background Radiation

CMS   Compact Muon Solenoid

CoGeNT   Coherent Germanium Neutrino Technology

COUPP   Chicagoland Observatory for Underground Particle Physics

CPD   Cryogenic PhotoDetector

CP   Charge-Parity

CRESST   Cryogenic Rare Event Search with Superconducting Thermometers

CRO   Cathode ray Oscilloscope

DAMIC   Dark Matter In CCDs

DAQ   Data Acquisition

DEAP   Dark Matter Experiment Using Argon Pulse-Shape Discrimination

DM   Dark Matter

EC   Electron Capture

EDELWEISS Expérience Pour Détecter les WIMPs En Site Souterrain

ER   Electron Recoil

G4NDL   GEANT4 Nuclear Data Library

GEANT   Geometry And Tracking

HAWC   High Altitude Water Cherenkov

HESS   High Energy Stereoscopic System

HV   High Voltage

iZIP Interleaved Z-sensitive Ionization Phonon

LEND Low Energy Nuclear Data

LFN Low Frequency Noise

LHAASO Large High Altitude Air Shower Observatory

LHC Large Hadron Collider

LMDM Low Mass Dark Matter

LNGS Laboratori Nazionali Del Gran Sasso

LSS Large Scale Structure

LUX Large Underground Xenon experiment

LZ LUX-ZEPLIN

MAGIC Major Atmospheric Gamma-Ray Imaging Cherenkov

NeutronHP Neutron High Precision

News-G New Experiments With Spheres-Gas

NLL Negative Log Likelihood

NR Nuclear Recoil

NTL Neganov-Trofimov-Luke

OF Optimal Filter

PandaX Particle and Astrophysical Xenon Detector

PDF	Probability Distribution Function
PICASSO	Projet D'identification de Candidats Supersymétriques Sombres
PSD	Power Spectral Density
QCD	Quantum Chromodynamics
RMS	Root Mean Squared
S/N	Signal To Noise Ratio
SNO	Sudbury Neutrino Observatory
SQUID	Superconducting Quantum Interference Device
STD	Standard Deviation
SUL	Soudan Underground Lab
SuperCDMS	Super Cryogenic Dark Matter Search
SUSY	Supersymmetry
TENDL	TALYS-based Evaluated Nuclear Data Library
TES	Transition Edge Sensor
TEXONO	Taiwan Experiment On Neutrino
VERITAS	Very Energetic Radiation Imaging Telescope Array System
WIMP	Weakly Interacting Massive Particles
ZEPLIN	Zoned Proportional Scintillation In Liquid Noble Gases

Chapter 1

Introduction

A comprehensive survey of the anisotropy in the cosmic microwave background radiation (CMBR) has been done by several experiments [1, 2]. Using the ΛCDM model (where Λ is the cosmological constant, and CDM stands for cold dark matter), the recent results of this survey by the PLANCK collaboration reveals that the total mass-energy budget of the Universe is divided as follows, baryons and leptons makes up $\sim 5\%$, dark energy makes up $\sim 68\%$, and dark matter (DM) makes up the remaining $\sim 27\%$ [2, 3]. In particle physics, the standard model summarizes the list of elementary particles that make up the baryons and leptons, and their interaction between one another through electromagnetic, strong and weak forces. However, what makes up the remaining 95% of the mass-energy budget of the Universe, i.e. dark energy and dark matter is unknown. The accelerating rate of expansion of the Universe is attributed to dark energy. Dark matter is the discrepancy seen in the masses of galaxies and galaxy clusters observed by astronomers if only their luminous regions are considered and compared to their gravitational masses. This chapter will begin

with a discussion on the evidences that hint towards the existence of DM, followed by a list of general properties they satisfy. This chapter will provide an overview of the different DM detection methods, with a more focused discussion on the direct DM search method. The chapter will conclude with a brief overview of the current state of direct DM search experiments and motivate the search for DM with masses less than 5 GeV.

1.1   Missing mass problem

In 1933, Frtiz Zwicky was the first to report a discrepancy between the observed and expected velocities of galaxies in the Coma cluster based on their luminous size [4]. He attributed the discrepancy to the presence of 'dark' matter, and thus coining the term. This section will have a summary of some major observations that lead to a consensus among the scientific community on the existence of DM in the Universe.

1.1.1   Galaxy rotation curves

One of the first comprehensively documented evidence in favour of DM comes from the observation of galaxy rotation curves. A galaxy is a system of gravitationally bound stars and hot gases that rotate around their center of gravity. They have a bulge at its center where the mass density is maximum and a disc that extends beyond the bulge. By balancing the gravitation force to the centrifugal force, we can relate the rotational velocity v of an object in the galactic disc at a distance R from the center of a galaxy with mass distribution $M(R)$ as,

$$v = \sqrt{\frac{GM(R)}{R}}, \tag{1.1}$$

where G is the gravitational constant. From Eq. 1.1, it can be seen that for any object

in the galactic disc, $v \propto 1/\sqrt{R}$. However, when astronomers started documenting the rotational velocity curves of galaxies, they observed that v was almost constant for values of R well beyond the luminous edge of the galaxies. This can be best summarised by the work of Vera Rubin in Fig. 1.1, where she compiles the galaxy rotation curves of several spiral galaxies around the milky way [5].
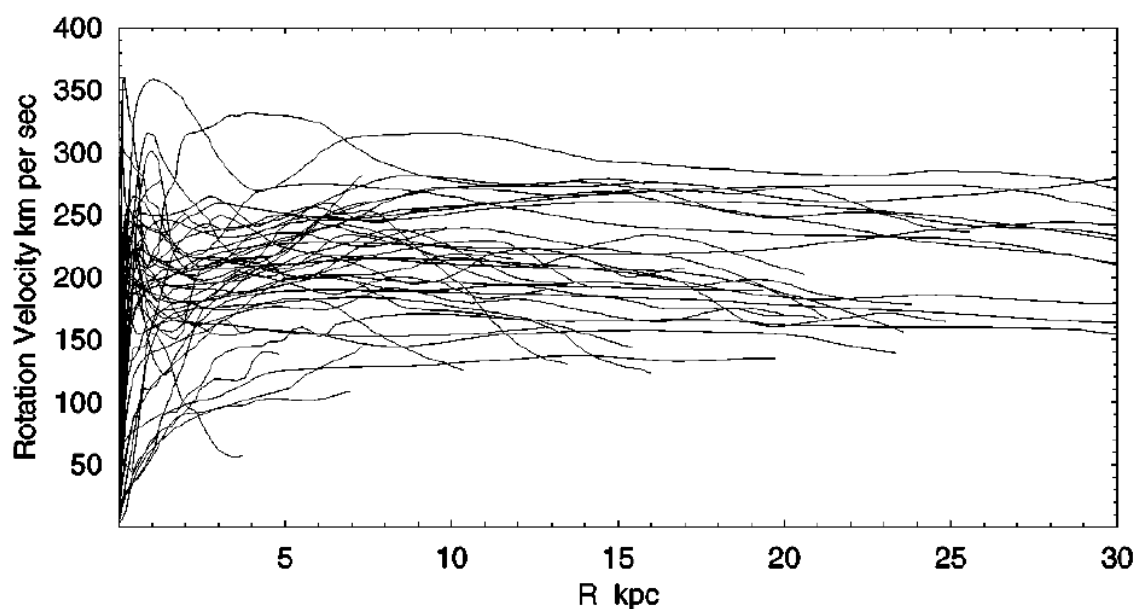
FIGURE 1.1: The rotational velocity distribution as a function of distance from the center of the galaxy is shown for several spiral galaxies nearby the Milky Way. Figure taken from Ref. [5]

This behaviour of the rotational velocity distribution is only possible if there exists more matter in the galaxy i.e. the value of $M(R)$ is under-counted when derived from its luminosity. The additional matter would thus have to be from a non-radiative source i.e. dark matter.
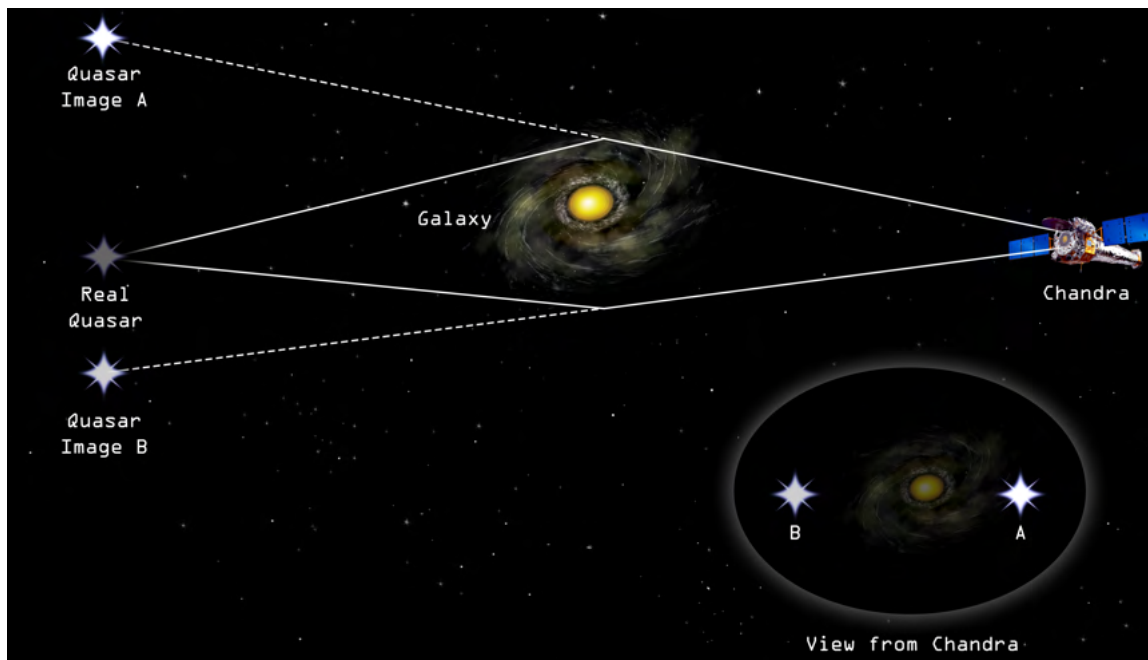
FIGURE 1.2: A schematic of the gravitational lensing effect due to a galaxy. Inset shows the image
              of the source object is split into multiple images to an observer on the other side of the
              lens. Image credit: NASA/CXC/SAO [6]

1.1.2   Gravitational lensing

From general theory of relativity, we know that any object with mass will warp the space-
time continuum. The more massive the mass, the more the distortion of space-time.
Einstein had predicted that this distortion can create a lens-like effect to an observer when
light passes through it [7]. Zwicky expanded upon this idea suggesting that the true masses
of galaxies can be obtained by studying their lensing effect [8]. Over time the study
of gravitational lensing effect around galaxies have evolved with further classifications of
lensing into strong, micro, and weak effects depending on the mass the lens and the distance
of light rays from the lens. Figure 1.2 gives a schematic of the bending of light around
a galaxy. This bending of light from a source on one side of the galaxy, splits the image
for an observer on the other side of the galaxy. Compared to the masses deduced by their

luminosities, astronomers have consistently reported an excess in the masses of galaxies, when obtaining them via gravitational lensing effect [9]. Recently the dark energy survey collaboration released a new detailed dark matter map of the Universe using gravitational lensing [10].
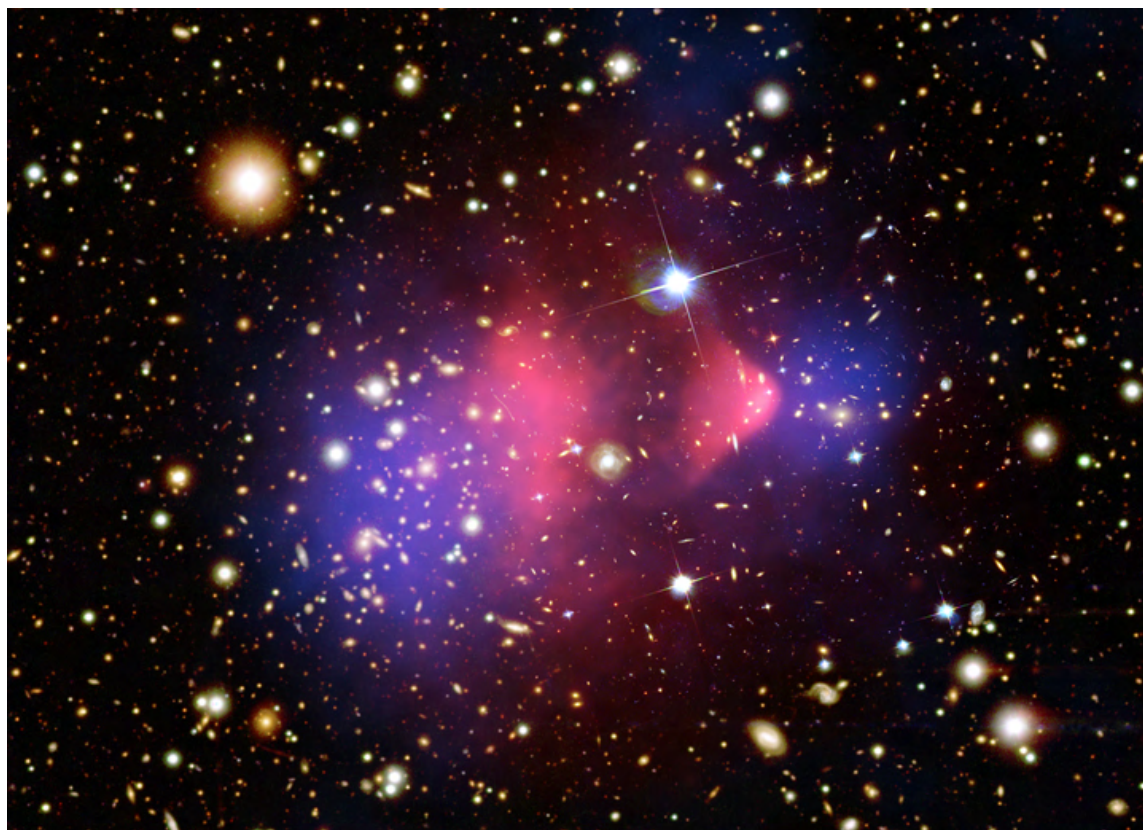
FIGURE 1.3: An artistic rendition of the Bullet cluster. Optical image from the Hubble Space Telescope and Magellan telescopes. Pink colour regions representing the Chandra x-ray measurement of hot gasses and blue region represents the gravitational lensing map. Image credit: X-ray: NASA/CXC/CfA; Optical: NASA/STScI; Magellan/U.Arizona; Lensing Map: NASA/STScI; ESO WFI; Magellan/U.Arizona [11]

A specific example of how the lensing technique helped reveal more information about DM is from cluster 1E 0657-558, also known as the Bullet cluster. This cluster is a remnant of two sub-clusters that collided and merged with each other ~100 million years ago. When two sub-clusters collide, the galaxies are expected to pass by each other. However,

the hot gasses are expected to collide and remain at the centers of the two sub-clusters. The Bullet cluster has been observed and studied using x-ray telescopes by the Chandra observatory [11]. In Fig. 1.3, the pink region shows the hot gases from the two sub-clusters after collision. A comparison of the image of the Bullet cluster with a gravity map obtained via gravitational lensing is shown in blue in Fig. 1.3. It can be seen that the center of gravity of the two sub-clusters do not lie within the luminous region of the Bullet cluster. This not only implies the presence of DM, but also an additional property that DM is almost collisionless.

1.1.3   Large scale structure formation

The large scale structure (LSS) formation refers to the evolution of the Universe after the Big Bang into its current state consisting of stars, galaxies, and clusters. The LSS is a result of the same density perturbations that gave rise to the anisotropies in the CMBR. The particles that make up visible matter are affected by radiation. The early Universe was radiation dominant. If the Universe only comprised of visible matter, then given the age of the Universe, there would not be sufficient time for the density perturbations to evolve into the galaxies and clusters as we see today. However, if one considers the presence of DM, which is unaffected by radiation then the time scale of the evolution of the Universe can be accelerated. The gravitational fields of DM act as an attractive potential for the visible matter, and thus collapsing them into galaxies and clusters, and accelerating the process of structure formation. Simulations of the LSS formation of the Universe assuming the ΛCDM model resulted in an almost identical state of the Universe as we see today [12, 13]. The comparison between simulations and galaxy surveys can be seen in Fig. 1.4.
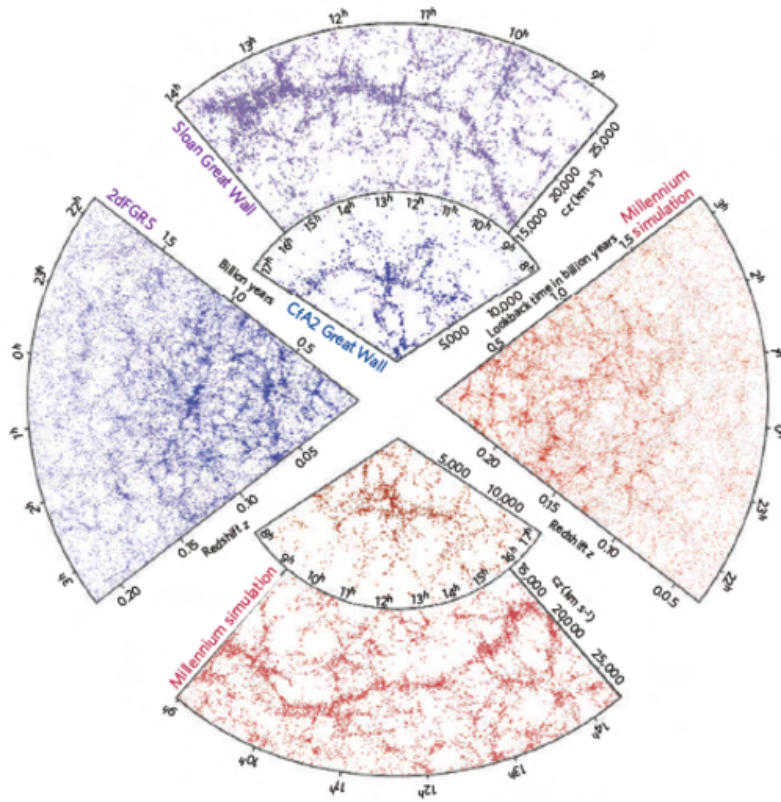
FIGURE 1.4: Simulation of the LSS, shown in red are compared to survey of the galaxy, which is shown in blue. The left slice, which is from the galactic map is similar to the right slice that is from simulations. Likewise the top slice which is from the galactic survey is similar to that obtained from simulation in the bottom slice. The filamentary structures in the figure represent galaxies, clusters and gasses clumping together. Figure taken from Ref. [12].

1.2 Identifying dark matter

From the observational evidences discussed in Sec. 1.1, it is possible to deduce the properties of DM, which will be the topic of discussion in Sec. 1.2.1. Based on the properties a set of most likely DM candidates is discussed in Sec 1.2.2. An overview of the DM detection techniques is given in Sec. 1.2.3.

1.2.1   Properties of dark matter

No electromagnetic interaction

The most apparent property of DM is that it has no electromagnetic interaction. This property can be deduced from all the evidences hinting towards the existence of DM like gravitational rotation curves, gravitational lensing, CMBR and LSS. DM is not observable via any of the telescopes used in standard astronomy. DM does however interact gravitationally as it is mapped by their gravitational lensing effect.

Almost collisionless

Observation of the Bullet cluster indicate that compared to visible matter, DM is almost collisionless. This can be deduced by the gravity map showing the centers of the two colliding sub-clusters having gone further past each other than the hot gasses.

Cold and stable

Observations of the current state of the galaxies and clusters in the Universe, as well as simulations of LSS reveal that DM must be cold, i.e. non-relativistic. On cosmological time scale, DM must also be stable as cold dark matter is assumed to have existed since the early Universe.

Relic density

From the latest CMBR measurements [2], the relative density of DM to total energy density of the Universe is ~27%. Any suitable DM solution must account for this constraint to the mass-energy budget of the Universe. The solution must also not affect the predicted abundances of currently known particles by Big bang nucleosynthesis that are validated by CMBR measurements [14].

1.2.2 Dark matter candidates

The properties discussed in Sec. 1.2.1 are not simultaneously satisfied by any particle from the standard model. However, several DM candidates have been proposed from beyond the standard model [14]. Figure 1.5 gives a summary of the several approaches to solving the DM problem and the resulting pool of DM candidates from each solution. We discuss the three most popular DM candidates in this subsection.

FIGURE 1.5: A visualization of the probable solutions to the DM problem, and the candidates that arrive from them. Here the abbreviations MOG stands for Modified Gravity model, TeVeS for tensor-vector-scalar theory, MOND for Modified Newtonian Dynamics, MaCHOs for Massive Compact Halo Objects. Details of the various DM candidates and their supporting theories are available in Ref. [14–16]. Figure taken from Ref. [15]

Weakly interacting massive particles

The most favoured candidate for DM belong to a classification called weakly interacting massive particles (WIMPs). These WIMPs arise from a hypothetical extension of the

standard model called supersymmetry (SUSY) that was proposed in 1984 [17]. SUSY introduces the idea that every standard model particle has a heavier partner i.e. a supersymmetric partner with its spin quantum number differing by half a unit. Particle physicists favour SUSY as an explanation to the 'fine tuning problem' with the mass of the Higgs boson [14]. WIMPs are SUSY particles that can have a mass ranging between 1 and 1000 GeV. They are expected to interact weakly with standard model particles making them discoverable. The total mass density of these hypothetical WIMP particles, if they exist, matches with the density of DM in the Universe measured by Cosmologists, a coincidence that is termed as the WIMP miracle [14]. Thus, they serve as an ideal candidate to bridge the gap between cosmic scale physics and particle physics with regard to the DM problem.

Axion

Axions were introduced to resolve a problem in understanding the behavior of particles interacting via the strong force in the standard model. In quantum chromodynamics (QCD), all particles are expected to have a charge-parity symmetry. However, particles that interact via the strong force violate this symmetry. A hypothetical light boson called axion was introduced to solve this strong CP violation [18, 19]. Axions are expected to have a mass in the range of μeV to meV. The mass of an axion particle is not as massive as the WIMPs, however it is expected to have a much higher number density in the universe to make up the DM relic density.

Sterile Neutrino

The standard model has three flavours of neutrinos, electron, muon, and tau. However, how neutrino gets its mass is an open problem in physics. One possible solution is the existence of a fourth flavour of neutrino called sterile neutrinos [14, 15]. Sterile neutrinos

would have right-handed chirality, and obtain their masses by the same mechanism as those for quarks and charged leptons. Sterile neutrinos are expected to have a mass in the eV scale. Like the neutrinos in the standard model, multiple kinds of sterile neutrinos with different masses are also hypothesized. Discovering a sterile neutrino can lead to a world of new physics beyond the standard model, termed as the dark sector [15]. The dark sector is postulated to be full of new particles like dark photons, dark gluons, and dark quarks that invisibly interact with each other. These new particles could then be used to explain the DM problem.

1.2.3 Types of detection techniques
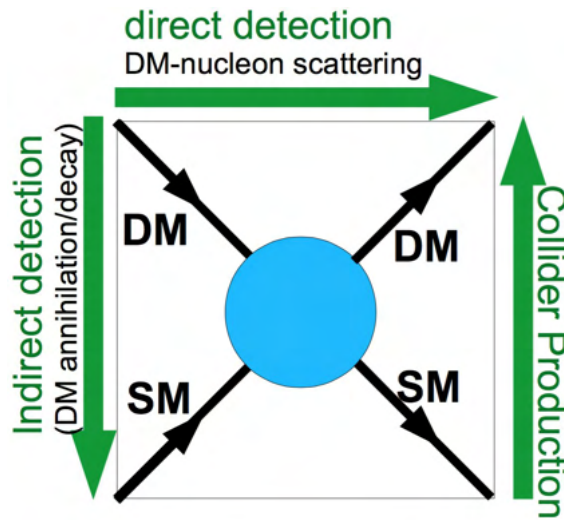
FIGURE 1.6: A schematic diagram to symbolize the three types of DM search mechanisms. The green arrows indicate the direction from participants to products in an interaction. The blue region symbolizes a mediator for the process. Here DM stands for dark matter particle and SM stands for standard model particle [20].

There are three approaches that can be taken to search for the various DM candidates. They are (i) by production at particle colliders, (ii) indirect detection, and (iii) direct detection. The basic ideology of each of these approaches are shown in the form of a

schematic diagram in Fig. 1.6. There are several experiments underway in each of these approaches. A brief description of each of these methods are given below.

Particle collider

In particle colliders, standard model particles like protons are collided with one another at energies high enough to reveal their constituent elementary particle. The high energy collisions between particles will briefly recreate an early universe environment where DM could be created from the decay of certain strongly-produced particles. The energy and momentum of all the particles produced in the collision are reconstructed. If the total energy before and after a collision is not conserved, then it can be due to the DM particle that went undetected through all the detectors. The ATLAS and CMS at CERN are some examples of collider experiments searching for DM [21].

Indirect method

If two DM particles, that can be their own antiparticles, interact and annihilate, they result in the production of standard model particles. These standard model products, could be neutrinos, gammas, or charged particles. Particle detectors on satellites above the Earth's atmosphere survey the Universe in all directions for these signatures of DM annihilation. Experiments like MAGIC, VERITAS, HESS, HAWC, and LHAASO are some of the experiments currently searching for DM annihilation signals [22].

Direct method

In a direct DM search method, a DM particle scatters off a standard model particle. The response of the standard model particle is directly observed through its recoil kinematics. The mass of the scattering DM particle for a given interaction cross section can be inferred

through such a process. The recoiling SM particle can give a signal in the form of phonons (heat), scintillation (light), charges (ionization), or a combination of these depending on the type of detector used in the experiment. SuperCDMS, PICO, CRESST, LZ are examples of direct DM search experiments [23]. In Sec. 1.3, the direct detection method is discussed in more detail.

1.3 Direct Detection method

Most direct DM search experiments are built around the framework conceptualized by Drukier and Stodolsky [24] for detecting neutrinos, which was expanded upon by Goodman and Witten [25] for direct DM searches. The mathematical formalism related to the dynamics of this method has been worked out in detail by Lewin and Smith [26]. In this section, a summary of the direct detection method is provided.

1.3.1 Mathematical framework

Consider the following assumptions for direct DM searches. Every galaxy is within a halo of DM. The density of DM particles (ρ_{DM}) in the halo have a central value of 0.4 GeV/cm^3 [26, 27]. The DM particles follow Maxwellian velocity distribution with a velocity parameter v_0 of 230 km/s [26]. The velocity of Earth (v_E) relative to the center of the galaxy is taken the same as v_0 [26]. If M_{DM} is the mass of a DM particle, and M_T is the mass of the nucleus of the detector material, then the observed event rate (R) by an experiment of a DM particle elastically scattering of the nucleus of the detector material is given by [26],

$$R(E_1, E_2) = \frac{c_1}{c_2} R_0 \left[e^{-c_2 E_1/E_0 r} - e^{-c_2 E_2/E_0 r} \right], \tag{1.2}$$

where E_1 and E_2 is the energy interval in which the event rate is measured by the experiment i.e. the lower and upper analysis threshold in an experiment. The unitless terms c_1, c_2 arise due to the motion of the Earth around the Sun which affect the event rate. The value of c_1/c_2 vary depending upon the time of the year, an effect also known as annual modulation [26]. R_0 is the total event rate expected by the experiment assuming $v_E = 0$ km/s. The units of R_0 is $\text{kg}^{-1}\text{d}^{-1}$, also called as integrated rate units (iru). The term r is a kinematic factor given by $4M_{DM}M_T/(M_{DM} + M_T)^2$, and E_0 is the most probable kinetic energy of the DM particle given by $\frac{1}{2}M_{DM}v_0^2$. The total event rate R_0 can be written as [26],

$$R_0 = \frac{503}{M_{DM}M_T}\left(\frac{\sigma_0}{1\,\text{pb}}\right)\left(\frac{\rho_{DM}}{0.4\,\text{GeV/cm}^3}\right)\left(\frac{v_0}{230\,\text{km/s}}\right), \qquad (1.3)$$

where σ_0 is the zero momentum transfer cross section between then DM particle and the nucleus of the detector material. The DM-nucleus cross section can be converted to DM-nucleon cross section (σ) using the relation below [28],

$$\sigma = \sigma_0 \frac{\mu_n^2}{\mu_T^2}\frac{C_n}{C_T}, \qquad (1.4)$$

where μ_n and μ_T are the reduced masses of the DM-nucleon and DM-detector nucleus system. If the mass number of the detector material is A, then $C_n/C_T = A^2$ [28]. The relationship in Eq. 1.4 is useful when trying to compare results from experiments using different detector material (and hence different M_T) as the interaction cross section is now normalized to a nucleon.

Direct DM search experiments measure the event rate R, i.e. the LHS of Eq. 1.2. For a given DM mass M_{DM}, experiments apply an upper limit on the R, which allows for a corresponding limit on the term R_0 on the RHS of Eq. 1.2. Using the relationships shown

in Eq. 1.3 and Eq. 1.4, the limit on R_0 can be converted as a limit on the DM-nucleon cross section σ. The results of all direct DM search experiments are shown in the DM-nucleon vs DM mass parameter space. A flowchart summarizing this process has been shown in Fig. 1.7

FIGURE 1.7: A simplified flowchart to summarize the process by which direct DM search experiments show their results. The terms R, R_0, σ_0, and σ carry the same meaning as defined Sec. 1.3.1. The process is repeated for different DM masses to generate a DM limit or exclusion curve.

1.3.2 Current status of dark matter searches

Figure 1.8 shows a summary of the results from different competing direct dark matter search experiments. Experiments like SuperCDMS/CDMSlite, DAMIC and EDELWEISS use semiconductor detectors like silicon and germanium. Experiments like DarkSide and DEAP use liquid argon while Xenon, LUX and PandaX use xenon as their detector material. News-G uses a spherical proportional counter filled with light gasses like hydrogen, helium and neon. As seen by the DM-nucleon cross section values in Fig. 1.8, detecting a DM particle is a rare event. Hence experiments must take sufficient precautions to shield against all possible backgrounds. All the direct DM search experiments are situated in deep underground laboratories to shield from cosmic rays. As the direct DM search experiments get more sensitive in terms of DM-nucleon cross sections, they will reach a point when neutrinos will scatter of the detector nucleus. This phenomena is termed as coherent elastic neutrino nucleus scattering (CEνNS). This will pose as a potential problem for these experiments as neutrinos cannot be shielded and would create an irreducible background
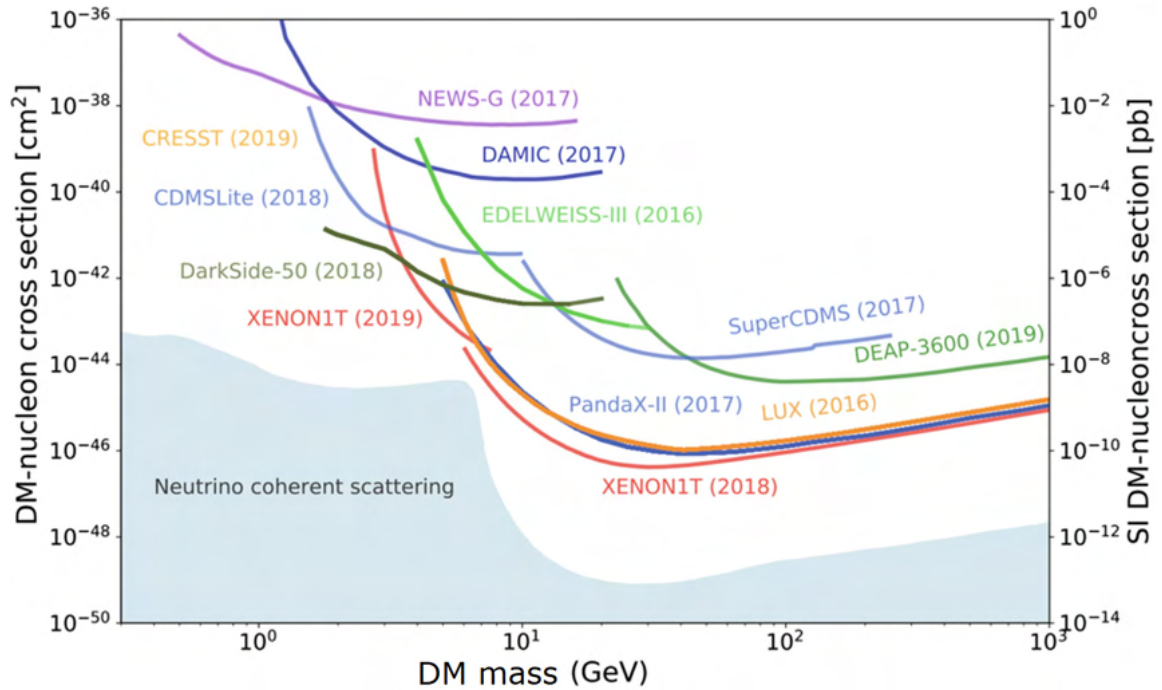
FIGURE 1.8: The results of several dark matter search experiments shown in the DM-nucleon vs DM mass parameter space. The region above a solid curve corressponding to an experiment has been excluded by it. The region below the solid curves is yet to be explored. The shaded region at the bottom of the figure corresponds to a phenomena called as coherent elastic neutrino nucleus scattering [29]. Figure taken from PDG 2020 [30].

for the experiment.

Figure 1.9 and Fig. 1.10 show a comparison of the recent results by collider experiments like CMS and ATLAS at CERN with some of the leading direct dark matter search results. The results are from the 13 TeV center-of-mass beam energy. With further upgrades and higher center-of-mass energies, they are likely to become competitive with the direct dark matter search experiments in terms of sensitivity to DM-nucleon cross section with an added advantage of not being concerned with CEνNS.
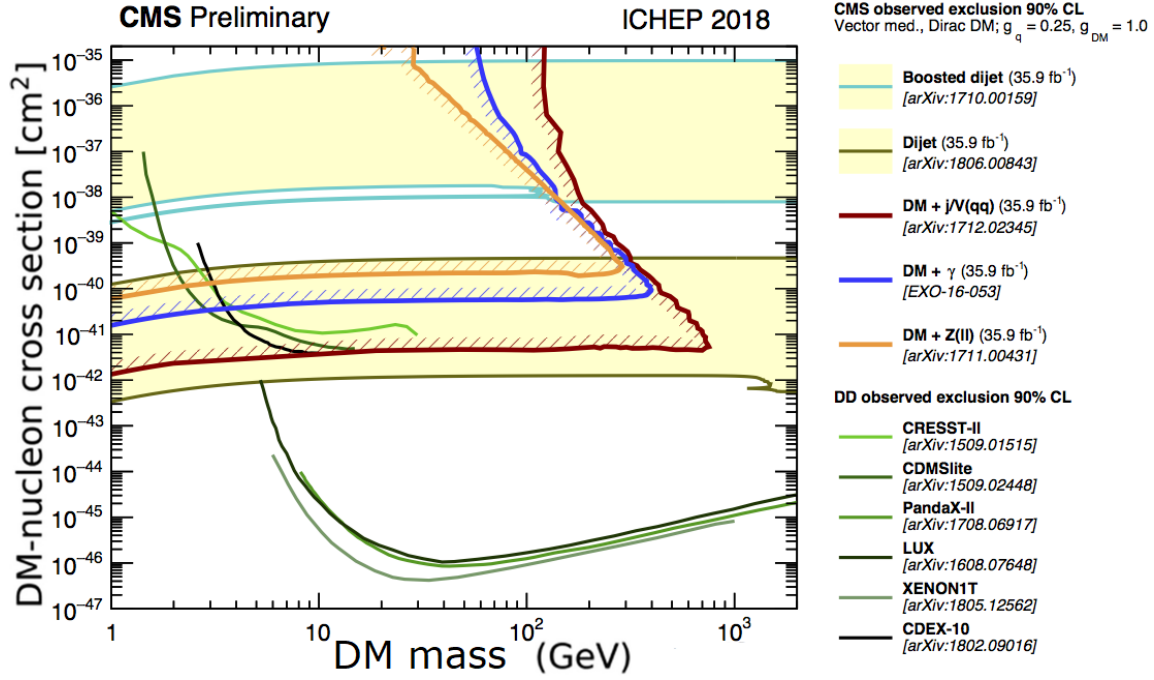
FIGURE 1.9: The search results from direct DM search experiments are compared with results by the CMS experiment at CERN in the DM nucleon vs DM mass parameter space [31]

1.3.3 Motivation for low mass dark matter searches

It can be seen in Fig. 1.8 that there are several experiments probing for DM in the mass range of 10–1000 GeV. Some of the most sensitive direct DM experiments in terms of DM-nucleon cross section have been designed for this mass range as WIMPs are considered as the most favourable DM candidate. However the increasing number of null results in this mass range, coupled with null results returned by collider experiments for SUSY have shifted the interest of physicists towards low mass dark matter (LMDM) particles in the sub-GeV range [33]. Several theories in support of LMDM such as asymmetric DM [34], or DM-Standard Model (SM) coupling through dark photons [35], are also shifting the focus of experimentalists towards LMDM searches. With constant advancements being made in detector technology, experiments are now beginning to explore the DM mass region below
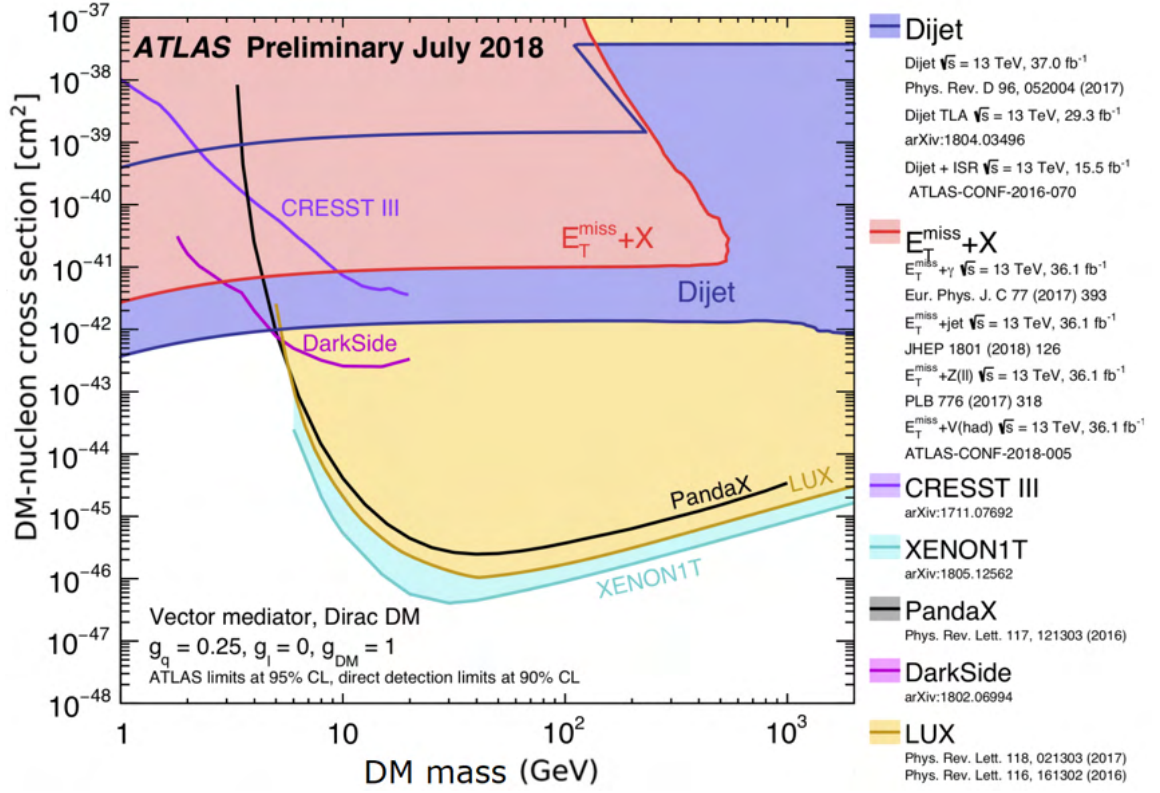
FIGURE 1.10: The search results from direct DM search experiments are compared with results by the ATLAS experiment at CERN in the DM nucleon vs DM mass parameter space [32].

1 GeV for new physics.

1.4 Prelude to work in this thesis

The key aspects for LMDM searches can be divided into three broad categories (i) development of detectors, (ii) low recoil energy calibration and measurement, and (iii) understanding of backgrounds in the experiment. A brief introduction of these three aspects and how they relate to the work presented in this thesis is done in this section.
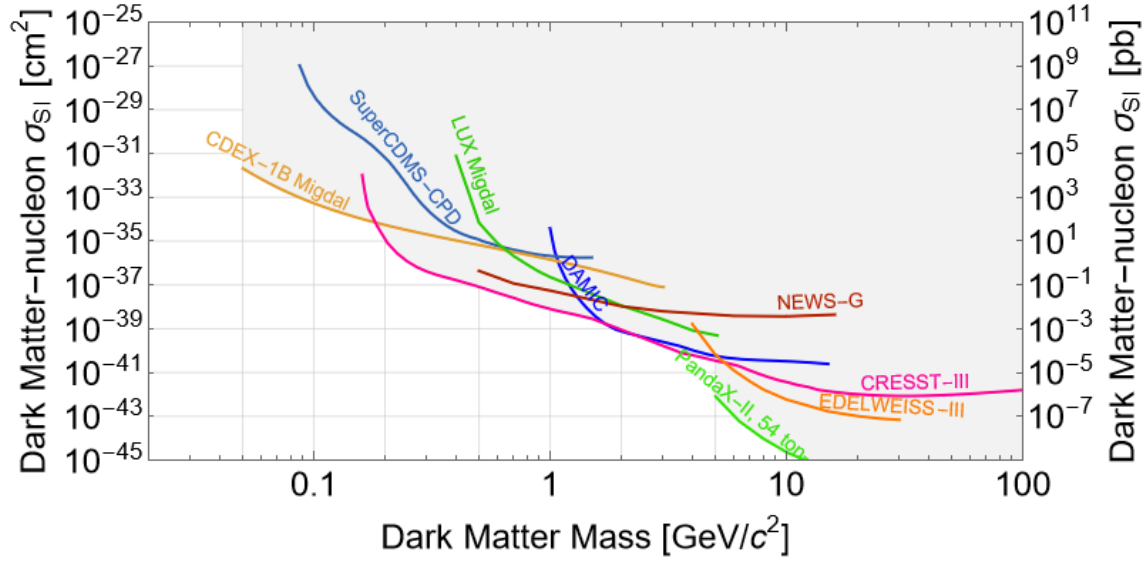
FIGURE 1.11: Results by experiments searching for low mass dark matters [36–43]. Figure made using the dark matter limit plotter by SuperCDMS [44]

1.4.1 Detectors for low mass dark matter search

Figure 1.11 focuses on the results published by experiments dedicated to LMDM searches in the DM-nucleon vs DM mass parameter space. The choice of material used as a detector plays a crucial role in LMDM searches. Semiconductors are a popular choice of material to be used as detectors for low mass dark matter searches [36–39]. There are also some experiments that are working on novel ideas like using gas detectors filled with a mixture of neon and CH_4, or using diamond as the detector medium [40, 45]. This is because materials with a lower atomic mass number will have a higher nuclear recoil from a scattering LMDM particle. Silicon detectors are preferred by several experiments as they have a low atomic mass number, offer better energy resolution than gas detectors, easier to produce, and have been well understood over time [46]. The silicon detectors currently in use by experiments like SuperCDMS and DAMIC have a mass of less than 10 g per detector module. To become more sensitive to the DM-nucleon cross section, these modules must have a larger

mass. But large mass detectors have historically been limited by leakage charges, thus affecting their signal to noise performance [47]. Chapter 2 of this thesis will be focused on the development of a large mass silicon detector for LMDM search. The detector will use a contact free electrode to counter the problem arising from the leakage charges, and thereby improving its signal to noise performance, to achieve a single electron baseline energy resolution.

1.4.2 Low recoil energy calibration and measurement
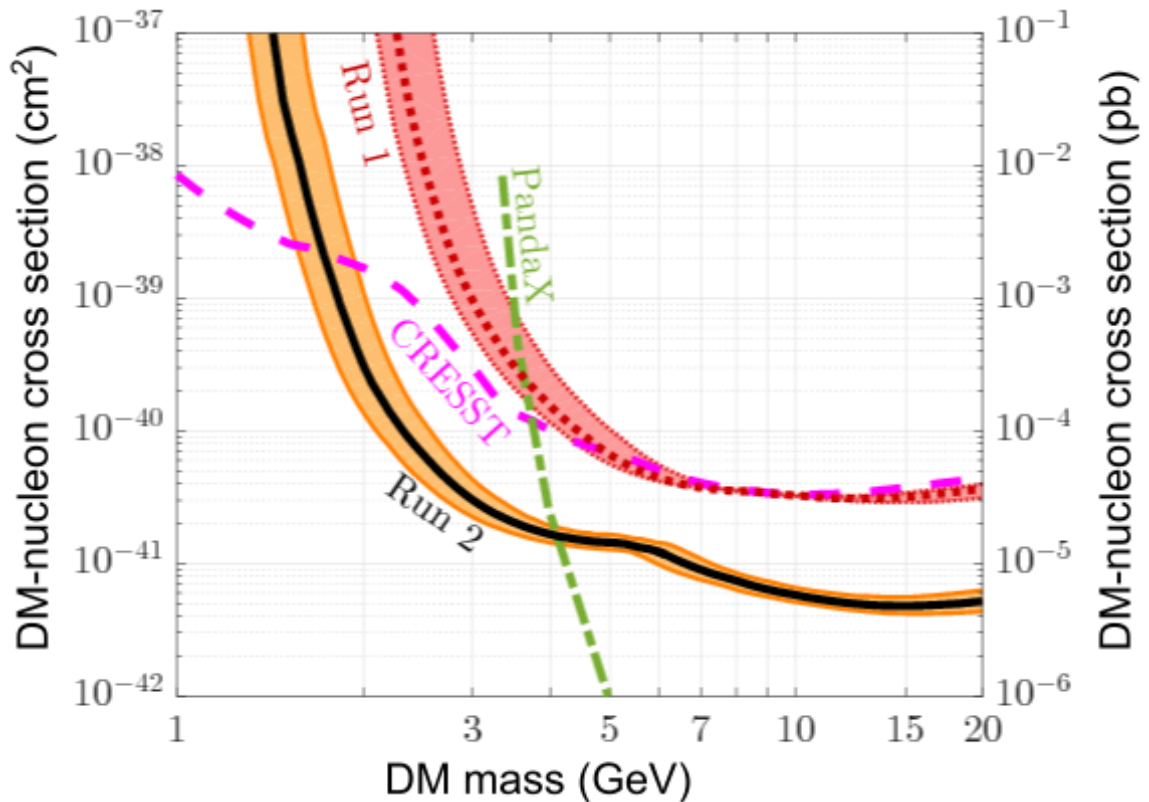
FIGURE 1.12: The results from the first and second runs by the SuperCDMS Soudan low ionization threshold experiment (CDMSlite) [48]. The results have a large uncertainty band owing to an uncertainty in the measured recoil energy in the detector.

Once a detector material is chosen, the next key aspect for LMDM search is precision

measurement of the recoil energy of the nucleus. Even for a lighter medium, a sub-GeV dark matter particle will produce a nuclear recoil energy less than 1 keV [49]. This is below the energy threshold of any semiconductor detector, thus establishing a need for amplifying the initial recoil signal in the detector. Phonon-mediated detectors like those used by SuperCDMS and EDELWEISS, do this by an indirect measurement of e^-/h^+ pairs in the detector through the phonons produced by them when accelerated within the detector at high voltages. These additional phonons act as the amplifying factor to the phonons from the nuclear recoil, thus allowing for the detection of a LMDM particle. Any uncertainty in the understanding of the electrons or holes drifted within the detector leads to an uncertainty in the recoil energy measured by the detector. Figure 1.12 shows the results of the SuperCDMS Soudan low ionization threshold experiment (CDMSlite) from their first and second run [48]. Since these detectors cannot directly measure the number of e^-/h^+ pairs produced in the detector, they utilize models to get this value in their detectors. Chapter 3 of this thesis is dedicated to an experiment performed with the germanium SuperCDMS Soudan detectors, to improve the precision of their recoil energy measurement. The experiment involves using monoenergetic neutrons of known energy to create nuclear recoils and deducing the ionization yield from it. The improved understanding of the ionization yield in the SuperCDMS detectors will improve the precision of the recoil energy measurements in its future runs.

1.4.3 Understanding backgrounds for dark matter searches

Backgrounds in an experiment play a major role in the ability to detect a rare and weak nuclear recoil signals from a LMDM. All direct dark matter search experiments are located in underground laboratories like Soudan Underground Lab (SUL), Sudbury Neutrino Observatory (SNO) lab, or the Gran Sasso National Laboratory (LNGS) to shield from
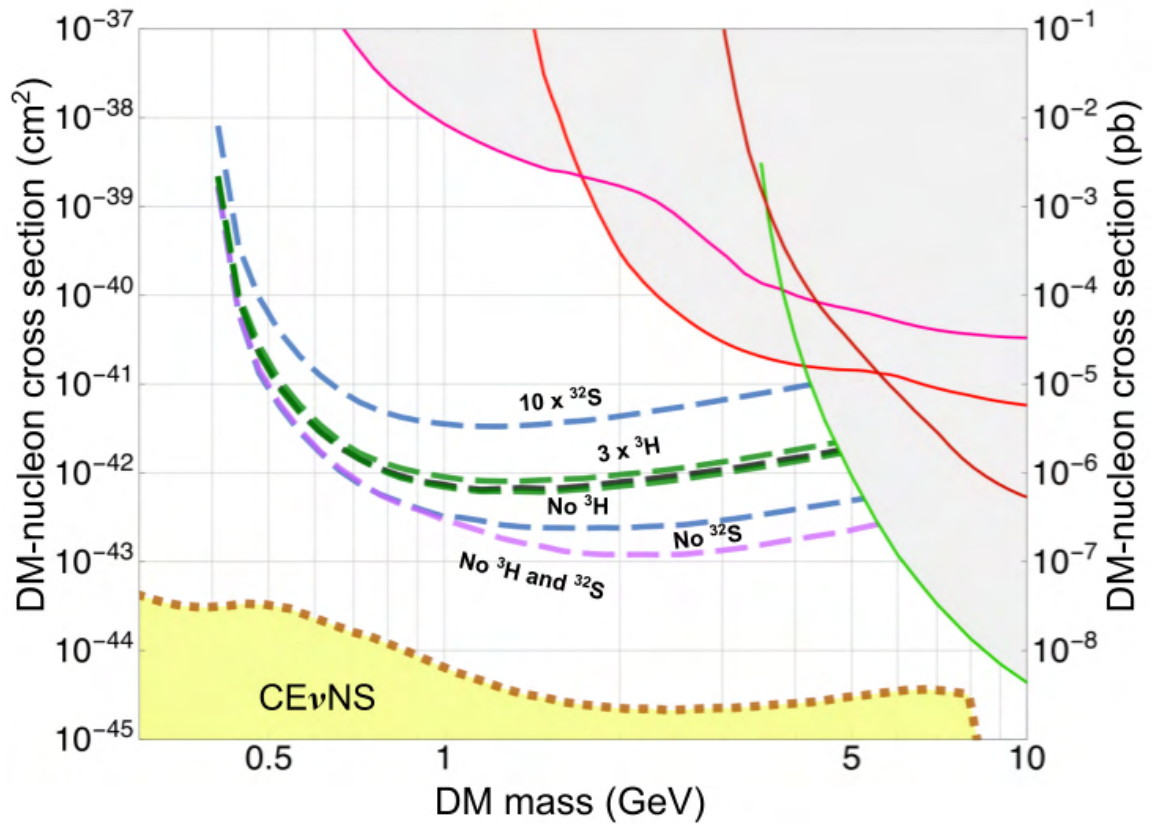
FIGURE 1.13: The effect of varying backgrounds on the sensitivity projected by SuperCDMS at SNOLAB [50]. The black dashed line is for nominal amount of ^{32}Si and ^{3}H background from literature. The green dashed line represent the effect of varying ^{3}H background. The lower green dashed line represents no ^{3}H, while the upper green dashed like represents ^{3}H three times above the nominal value. Likewise the lower blue dashed line represents no ^{32}Si contamination in the SuperCDMS Si detectors, while the upper blue dashed line is for 10 times the nominal value of ^{32}Si in the detector. The purple dashed line represents no ^{32}Si or ^{3}H background in the experiment.

high energy cosmic rays and other environmental radiations on the surface that would bury any DM signals in their detectors. Even underground, adequate understanding is needed to reduce or reject muons and neutrons from cosmic rays, and also from radiation within the underground cavern environment. The LMDM detectors are so sensitive that even radiation from cosmogencially activated isotopes of elements which make it through the

detector fabrication process, even after stringent measures, act as a background affecting the detector's sensitivity to a potential LMDM scattering event. In Fig. 1.13, the effect of varying two such cosmogenically activated radioactive isotopes, ^{32}Si and ^{3}H, are shown on the sensitivity projections using a silicon high voltage detector at SNOLAB [50]. It can be seen in this figure, that lower the background, better the sensitivity curve. Chapter 4 of this thesis will review the backgrounds from isotopes like ^{3}H, ^{55}Fe, ^{65}Zn and ^{68}Ge measured in SuperCDMS germanium detectors. The chapter will also contain a discussion on the ongoing estimation of the ^{32}Si background in the silicon detectors used by SuperCDMS.

The thesis thus aims to cover all major aspects needed to set-up a direct LMDM search experiment. The last chapter in this thesis will summarize the main conclusions from each chapter and provide an outlook towards the next steps that can be taken based on the work done in this thesis.

Bibliography

[1]   E. Komatsu et al. "Seven-Year Wilkinson Microwave Anisotropy Probe (WMAP) Observations: Cosmological Interpretation". *Astrophys. J. Suppl.* 192 (2011), p. 18. arXiv: 1001.4538 [astro-ph.CO].

[2]   P. A. R. Ade et al. "Planck 2015 results. XIII. Cosmological parameters". *Astron. Astrophys.* 594 (2016), A13. arXiv: 1502.01589 [astro-ph.CO].

[3]   Andrew Liddle. *An introduction to modern cosmology; 2nd ed.* Chichester: Wiley, 2003.

[4]   F. Zwicky. "Die Rotverschiebung von extragalaktischen Nebeln". *Helv. Phys. Acta* 6 (1933), pp. 110–127.

[5]   Yoshiaki Sofue and Vera Rubin. "Rotation Curves of Spiral Galaxies". *Annual Review of Astronomy and Astrophysics* 39.1 (2001), pp. 137–174. eprint: https://doi.org/10.1146/annurev.astro.39.1.137.

[6]   Chandra X ray Observatory. *Gravitational lensing*. https://chandra.harvard.
      edu/resources/illustrations/gravitational.html.

[7]   Albert Einstein. "Lens-Like Action of a Star by the Deviation of Light in the Gravi-
      tational Field". *Science* 84 (1936), pp. 506–507.

[8]   F. Zwicky. "Nebulae as Gravitational Lenses". *Phys. Rev.* 51 (4 Feb. 1937), pp. 290–
      290.

[9]   Richard Massey, Thomas Kitching, and Johan Richard. "The dark matter of grav-
      itational lensing". *Rept. Prog. Phys.* 73 (2010), p. 086901. arXiv: 1001.1739
      [astro-ph.CO].

[10] M. Gatti et al. "Dark Energy Survey Year 3 Results: Weak Lensing Shape Catalogue"
      (Nov. 2020). arXiv: 2011.03408 [astro-ph.CO].

[11] Chandra X ray Observatory. *NASA Finds Direct Proof of Dark Matter*. https:
      //chandra.harvard.edu/photo/2006/1e0657/.

[12] Volker Springel and others. "The large-scale structure of the Universe". *Nature* 440
      (2006), p. 1137. arXiv: astro-ph/0604561.

[13] Volker Springel et al. "Simulating the joint evolution of quasars, galaxies and
      their large-scale distribution". *Nature* 435 (2005), pp. 629–636. arXiv: astro-
      ph/0504097.

[14] Jonathan L. Feng. "Dark Matter Candidates from Particle Physics and Methods of
      Detection". *Ann. Rev. Astron. Astrophys.* 48 (2010), pp. 495–545. arXiv: 1003.0904
      [astro-ph.CO].

[15] Gianfranco Bertone and Tim M. P. Tait. "A new era in the search for dark matter".
      Nature 562.7725 (Oct. 2018), pp. 51–56. ISSN: 1476-4687.

[16] Gianfranco Bertone and Dan Hooper. "History of dark matter". *Rev. Mod. Phys.* 90
      (4 Oct. 2018), p. 045002.

[17] Howard E. Haber and Gordon L. Kane. "The Search for Supersymmetry: Probing
      Physics Beyond the Standard Model". *Phys. Rept.* 117 (1985), pp. 75–263.

[18] Frank Wilczek. "Problem of Strong *P* and *T* Invariance in the Presence of Instantons".
      Phys. Rev. Lett. 40 (1978), pp. 279–282.

[19] Steven Weinberg. "A New Light Boson?" *Phys. Rev. Lett.* 40 (1978), pp. 223–226.

[20] Andreas Korn. *DM: Latest results in the mono-jet and di-jet channels*. `https://indico.cern.ch/event/342623/contributions/807352/attachments/1250088/1842740/DMLHC_2016_Kornv2.pdf`.

[21] Antonio Boveia and Caterina Doglioni. "Dark Matter Searches at Colliders". *Ann. Rev. Nucl. Part. Sci.* 68 (2018), pp. 429–459. arXiv: `1810.12238 [hep-ex]`.

[22] Rebecca K. Leane. *Indirect Detection of Dark Matter in the Galaxy*. 2020. arXiv: `2006.00513 [hep-ph]`.

[23] Marc Schumann. "Direct Detection of WIMP Dark Matter: Concepts and Status". *J. Phys. G* 46.10 (2019), p. 103003. arXiv: `1903.03026 [astro-ph.CO]`.

[24] A. Drukier and Leo Stodolsky. "Principles and Applications of a Neutral Current Detector for Neutrino Physics and Astronomy". *Phys. Rev. D* 30 (1984). Ed. by J. Tran Thanh Van, p. 2295.

[25] Mark W. Goodman and Edward Witten. "Detectability of Certain Dark Matter Candidates". *Phys. Rev. D* 31 (1985). Ed. by M. A. Srednicki, p. 3059.

[26] J.D. Lewin and P.F. Smith. "Review of mathematics, numerical factors, and corrections for dark matter experiments based on elastic nuclear recoil". *Astroparticle Physics* 6.1 (1996), pp. 87–112. ISSN: 0927-6505.

[27] Evalyn I. Gates, Geza Gyuk, and Michael S. Turner. "The Local halo density". *Astrophys. J. Lett.* 449 (1995), pp. L123–L126. arXiv: `astro-ph/9505039`.

[28] Hyun Su Lee et al. "First limit on wimp cross section with low background csi(tl) crystal detector". *Phys. Lett. B* 633 (2006), pp. 201–208. arXiv: `astro-ph/0509080`.

[29] Daniel Z. Freedman. "Coherent Effects of a Weak Neutral Current". *Phys. Rev. D* 9 (1974), pp. 1389–1392.

[30] P. A. Zyla et al. "Review of Particle Physics". *PTEP* 2020.8 (2020), p. 083C01.

[31] CMS Collaboration. *CMS Exotica Summary plots for ICHEP 2018*. `https://twiki.cern.ch/twiki/bin/view/CMSPublic/SummaryPlotsEXO13TeV`.

[32] ATLAS Collaboration. "ATLAS Feature: Dark Matter". General Photo. Mar. 2019.

[33] Norman A. Graf et al., eds. *Proceedings, 2013 Community Summer Study on the Future of U.S. Particle Physics: Snowmass on the Mississippi (CSS2013): Minneapolis, MN, USA, July 29-August 6, 2013*. 2013.

[34] David E. Kaplan et al. "Asymmetric Dark Matter". *Phys. Rev. D* 79 (2009), p. 115016. arXiv: 0901.4117 [hep-ph].

[35] Itay M. Bloch et al. "Searching for dark absorption with direct detection experiments". *Journal of High Energy Physics* 06.6 (June 2017), p. 87. ISSN: 1029-8479.

[36] I. Alkhatib et al. "Light Dark Matter Search with a High-Resolution Athermal Phonon Detector Operated Above Ground" (July 2020). arXiv: 2007.14289 [hep-ex].

[37] A. Aguilar-Arevalo et al. "Results on Low-Mass Weakly Interacting Massive Particles from an 11 kg d Target Exposure of DAMIC at SNOLAB". *Phys. Rev. Lett.* 125 (24 Dec. 2020), p. 241803.

[38] Z. Z. Liu et al. "Constraints on Spin-Independent Nucleus Scattering with sub-GeV Weakly Interacting Massive Particle Dark Matter from the CDEX-1B Experiment at the China Jinping Underground Laboratory". *Phys. Rev. Lett.* 123 (16 Oct. 2019), p. 161301.

[39] L. Hehn et al. "Improved EDELWEISS-III sensitivity for low-mass WIMPs using a profile likelihood approach". *Eur. Phys. J. C* 76.10 (2016), p. 548. arXiv: 1607.03367 [astro-ph.CO].

[40] Q. Arnaud et al. "First results from the NEWS-G direct dark matter search experiment at the LSM". *Astropart. Phys.* 97 (2018), pp. 54–62. arXiv: 1706.04934 [astro-ph.IM].

[41] Xiangyi Cui et al. "Dark Matter Results from 54-Ton-Day Exposure of PandaX-II Experiment". *Phys. Rev. Lett.* 119 (18 Oct. 2017), p. 181302.

[42] D. S. Akerib et al. "Results of a Search for Sub-GeV Dark Matter Using 2013 LUX Data". *Phys. Rev. Lett.* 122.13 (2019), p. 131301. arXiv: 1811.11241 [astro-ph.CO].

[43] A. H. Abdelhameed et al. "First results from the CRESST-III low-mass dark matter program". *Phys. Rev. D* 100 (10 Nov. 2019), p. 102002.

[44] SuperCDMS Collaboration. *Dark matter limit plotter*. https://supercdms.slac.stanford.edu/dark-matter-limit-plotter.

[45] Noah Kurinsky et al. "Diamond detectors for direct detection of sub-GeV dark matter". *Phys. Rev. D* 99 (12 June 2019), p. 123005.

[46]   Helmuth Spieler. *Semiconductor Detector Systems*. Vol. v.12. Semiconductor Science and Technology. Oxford: Oxford University Press, 2005. ISBN: 978-0-19-852784-8.

[47]   Ritoban Basu Thakur. "The Cryogenic Dark Matter Search low ionization-threshold experiment". PhD thesis. Illinois U., Chicago, 2014.

[48]   R. Agnese et al. "Low-mass dark matter search with CDMSlite". *Phys. Rev. D* 97.2 (2018), p. 022002. arXiv: 1707.01632 [astro-ph.CO].

[49]   Rouven Essig et al. "Direct detection of sub-GeV dark matter". *Phys. Rev. D* 85 (7 Apr. 2012), p. 076007.

[50]   R. Agnese et al. "Projected sensitivity of the SuperCDMS SNOLAB experiment". *Phys. Rev. D* 95 (8 Apr. 2017), p. 082002.

Chapter 2

Silicon HV detector

From chapter 1, we understood that there is a strong motivation to search for low mass dark matter (LMDM) in the sub-GeV mass range. In direct detection method, LMDM search should have large mass detectors with low energy thresholds [1]. Simultaneously achieving both these requirements is a challenge when building a LMDM detector. In this chapter the requirements for building a detector for LMDM search will be examined in Sec. 2.1. The operation of a phonon-mediated 100 g Silicon (Si) detector with a contact free (CF) electrode built to meet these requirements are discussed in Sec. 2.2. The analysis of the detector's performance in terms of its phonon noise performance, signal gain and the signal-to-noise ratio (S/N) is discussed in Sec. 2.3. As we will see later in this chapter, the performance of this detector is optimal at high bias voltages (HV) between 150-250 V, hence in shorthand the detector is called as Si HV detector. The chapter ends with a summary and outlook in Sec. 2.4.

2.1   Requirements for building a detector for low mass dark matter search

From the perspective of building an ideal direct detection LMDM search detector, there are three main requirements: (i) Choose an appropriate detector material to maximize nuclear recoil energy produced during an elastic scattering of a dark matter (DM) particle with the detector nucleus, (ii) Lower the electronic noise in the detector to minimize the energy threshold as well as improve the energy resolution, and (iii) Increase the payload of the experiment i.e. the total mass of the detector to enhance the DM-nucleon cross-section. We discuss each of these requirements in more detail from Sec. 2.1.1 to Sec. 2.1.3.

2.1.1   Maximize nuclear recoil

The first requirement is to maximize the nuclear recoil produced in the detector during an elastic scattering process by a DM particle. The nuclear recoil within the detector produces signals, in the form of heat, light, charges or a combination of these, which become the measured quantity in the experiment. More the nucleus recoils, better is the signal. If we consider M_{DM} to be the mass of a DM particle, and M_T to be the mass of the element that makes up the detector, then from the conservation of energy and momentum the maximum energy transfer between the two bodies, and hence the maximum nuclear recoil, in an elastic collision is when $M_{DM} = M_T$. In the case of LMDM, we assume $M_{DM} << M_T$. If E_r is the nuclear recoil energy, then from Appendix A we see that under this assumption, the energy transfer equation gives the relation $E_r \propto M_{DM}^2$, and $E_r \propto 1/M_T$. So lighter the mass of the target nucleus more the recoil energy produced in a LMDM interaction. Using the formalism derived by Lewin and Smith in their paper [1], we show in Fig. 2.1 how choosing different detector materials based on their atomic mass number affects the DM sensitivity
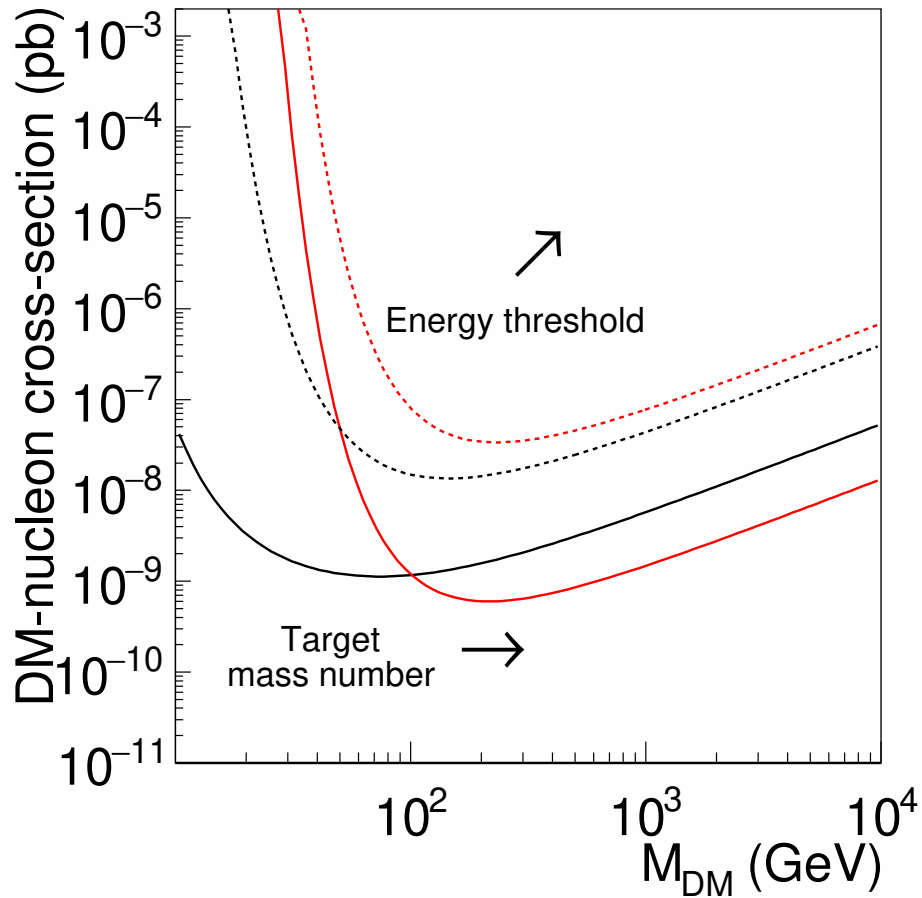
FIGURE 2.1: Limit curves in the DM-nucleon cross-section vs the DM mass parameter space is shown. The effect of changing the atomic mass number of the target i.e. detector material on the limit curves can be seen by following the solid lines. The solid red line has a high mass number than the solid black line. The effect of the energy threshold on the limit curves can be seen by following the solid and dashed lines of the same colour. The dashed line has a higher energy threshold than the solid line.

curve in the DM-nucleon cross-section vs DM mass parameter space. We see that the solid curves shift towards the left as the mass number of the target material is lowered implying detectors with lower atomic mass number are better suited for LMDM searches. Among semiconductors, this makes Si the best candidate with an atomic mass number of ~ 28 atomic mass units (amu). Hence to satisfy the requirement of maximizing recoil energy produced by a LMDM elastically scattered by the nucleus, the preferred choice of detector

material would be Silicon.

2.1.2   Minimize energy threshold

The second requirement is to have a low energy threshold for recoil energy measurement in the detector. The energy threshold is the value below which extracting any information about the signal is unfeasible due to high noise levels or poor detector energy resolution or a combination of both. Consider the widely adopted formula for the differential DM scattering rate given by Lewin and Smith [1] for direct detection methods of DM, in Eq. 2.1 below.

$$\frac{dR}{dE_r} = \frac{R_0}{E_0 r} e^{-E_r/E_0 r}, \tag{2.1}$$

where, R is the event rate per unit mass, R_0 is the total event rate, E_0 is the most probable incident kinetic energy of a DM particle of mass M_{DM}, and r is a kinematic factor given by $4M_{DM}M_T/(M_{DM} + M_T)^2$. The terms E_r, M_{DM}, and M_T retain their definitions from earlier in this chapter.

Figure 2.2 shows the DM scattering rate calculated using Eq. 2.1 as a function of recoil energy. From Fig 2.2 (a) we can make the following observations on the scattering rate distribution for a fixed Si target, (i) lower the energy threshold, higher the scattering rate, (ii) lower the dark matter mass, lower the end point of the recoil energy distribution. From this it can be inferred that the energy threshold of the detector must be sufficiently lower than the end point of the maximum recoil energy expected for the intended DM mass while also having a high enough scattering rate to increase the chances of detecting a LMDM. This is illustrated by the vertical brown line in Fig 2.2 (a). From Fig 2.2 (b), we see that for a given mass of DM, the end point of the recoil energy distribution is maximum for the lightest element. Fig 2.2 (b) reaffirms the conclusion made from Sec. 2.1.1 of Si being the
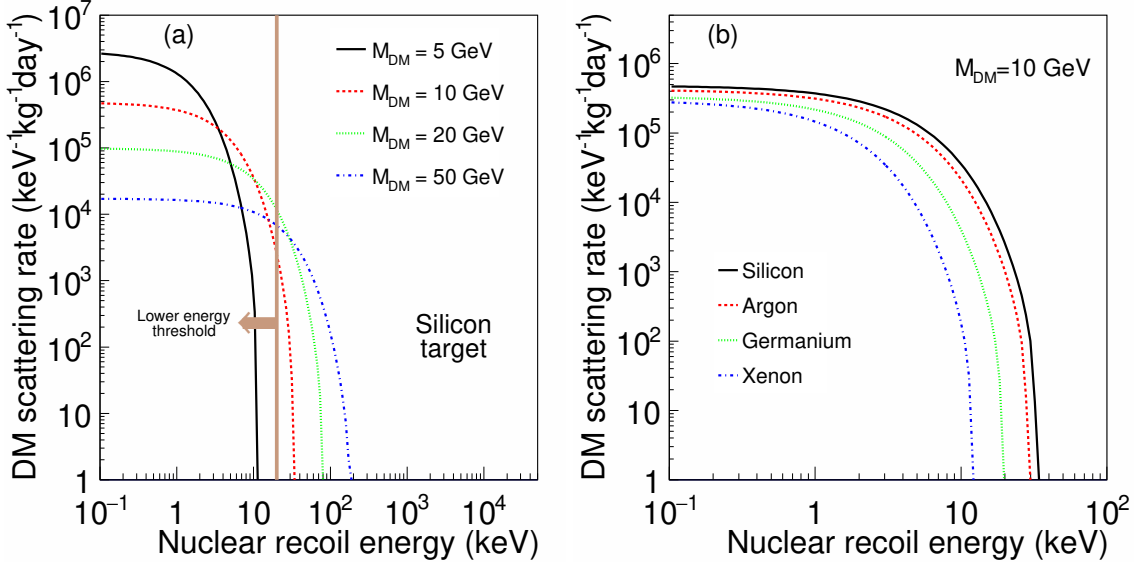
FIGURE 2.2: The DM scattering rate which is the L.H.S. in Eq. 2.1 is shown as a function of nuclear recoil energy. (a) The DM scattering rate for different masses of DM in a fixed Silicon detector is shown. The brown vertical line indicates the increasing possibility to detect a DM particle if the recoil energy threshold of the detector is lowered. (b) For a given DM mass, the recoil energy distribution in different target materials is shown.

best candidate to use as a detector for LMDM searches. The effect of varying the energy thresholds is also shown in Fig. 2.1 by comparing the dashed lines with the solid lines of the same colour. Lines of the same colour correspond to the same target material. The dashed lines have a higher energy threshold than the solid lines. We see that the solid lines cover more parameter space in the low mass region than the dashed lines. Thus we establish that the sensitivity to detect LMDM is better for detectors with lower energy thresholds.

The limiting factor in attaining lower energy thresholds in semiconductor devices is the inherent noise in the detector [2]. The noise could arise from different sources like imperfect electronics or external interference, but the primary source is usually the electronic noise. The electronic noise can be divided into 3 groups, (i) thermal (or Jhonson) noise, (ii) shot noise (or leakage), and (iii) low frequency (or $1/f$) noise (LFN). To understand the electronic noise better, consider the current passing through a material placed between two

electrodes separated by a distance *s*. The current is made up of *n* electrons moving with velocity *v*. From the Shockley-Ramo theorem [3, 4], the induced current *i* depends on *s*. In other words,

$$i = \frac{nev}{s} \tag{2.2}$$

Any fluctuation in the induced current i is given by,

$$\langle di \rangle^2 = \left(\frac{ne}{s} \langle dv \rangle \right)^2 + \left(\frac{ev}{s} \langle dn \rangle \right)^2 \tag{2.3}$$

From Eq. 2.3 we see that the contribution to electronic noise i.e. induced current in the circuit can be either due to a fluctuation in velocity, which is the first term in Eq. 2.3, or a fluctuation in the number of electrons which is the second term in Eq. 2.3. Thermal noise arises due to velocity fluctuations and can be written as $i_n^2 = 4kT/R$, where i_n^2 is the spectral noise current density, k is the Boltzmann constant, T is the absolute temperature, and R is the resistance in the circuit [2]. Thermal noise can be reduced by lowering the temperature of the detector. The shot noise and LFN arise due to fluctuation in the number of charges in the induced current. Shot noise occurs when charge carriers are injected into the detector independently of one another [2, 5]. It can be reduced by insulating the detector material from other materials like the electrodes [5]. LFN arises when charges are trapped due to imperfections in the detector material and later gets released with a time constant τ [2]. This fluctuation in the number of charges is thus a function of the their time constants. Since their power spectral density (PSD) assumes a $1/f$ distribution, LFN is also called as $1/f$ noise. LFN can be reduced by using pure materials with minimal defects and periodic flashing of the detector material with infra-red or ultra-violet light, depending on the band gap of the material, to remove any trapped charges before an experimental run. The amplitude distribution of noise is generally Gaussian in nature. The width of the

Gaussian is a measure of the RMS noise in the detector. Reducing the electronic noise will also simultaneously improve the energy resolution of the detector since the width of the noise Gaussian will reduce [2].

2.1.3 Maximize payload of the experiment

The payload is the total mass of all the detector modules used in the experiment. To improve the sensitivity of an LMDM search experiment to DM particle with low cross sections of interaction with the detector, one or both of the following two conditions must be satisfied: (i) the experiment takes data continuously for a very long period of time i.e. large run times, and (ii) the payload of the experiment is large. The product of the run time of an experiment to its detector payload is called as exposure. Running an experiment for a very long period of time presents practical difficulties in terms of maintaining the necessary operating conditions for the detector, for example, maintaining the temperature of the detectors, and prevent charge trapping. Hence satisfying the second condition i.e. increasing the payload is often preferred by experiments. The only caveat being increased cost of setting up the experiment. Building a single large mass detector of a material that matches the desired payload of the experiment can provide fabrication, transport and more importantly difficulties with detector performance in terms of signal to noise and energy resolution when compared to smaller modules of detectors of the same material. A lightweight detector of the same material will demonstrate significantly better performance. However assembling a large number of lightweight detector modules would again create difficulties in the form of wiring, more readout modules and associated noise. Hence finding the right balance between the mass of each detector module and detector performance is crucial. Direct detection experiments like CDMS-II [6], or future experiments like SuperCDMS SNOLAB [7] utilize Si detectors for LMDM searches of

mass in the range ~ 100 g to 300 g. This has become the benchmark for the mass of a detector module used in an experiment.

2.1.4   Section summary

Once we have a detector that satisfies all the above requirements discussed from Sec. 2.1.1 to 2.1.3, it has to be placed in a low background (ideally zero background) environment. A review on the effects of different backgrounds on the sensitivity of an experiment to LMDM will be explained in chapter 4. The summary of this section is that to effectively search for LMDM, the detector should satisfy the following properties, (i) made of a material with low atomic mass number, which, among semiconductors is Si , (ii) have low electronic noise to reduce energy threshold and improve energy resolution, (iii) each detector module should have a mass of ~ 100 g to 300 g, (iv) placed in a low background environment. In the next section we will examine the development of a 100 g Si detector which will have a contact free (CF) electrode to reduce the shot noise, and operated at cryogenic temperatures (mK scale). It will utilize a process called as Neganov-Trofimov-Luke (NTL) effect [8, 9] to improve the signal gain at higher bias voltages (HV). The combination of all these properties make the CF Si HV detector an ideal candidate as a LMDM detector.

2.2   Detector Technology

In this section we begin with the working principle of a Si semiconductor detector that measures phonon signals in direct detection dark matter search experiments. Then we discuss the NTL effect [8, 9] as a means to amplify the phonon signals in the detector. This will be followed by a discussion on the phonon sensors used in this detector. The section ends with a method to reduce the shot noise in the detector by using a contact free electrode

to bias the detector.

2.2.1 Working principle

There are two types of interactions possible in a silicon detector, (i) Electron recoil (ER), and (ii) Nuclear recoil (NR). When an electron or gamma interacts with the detector, they scatter off the atomic electrons creating an ER. When a neutron or DM interact with the detector, they scatter off the atomic nucleus creating a NR. In an ER, all the energy of the incident particle goes into creating e^-/h^+ pairs. In a NR only part of the energy of the incident particle goes into creating e^-/h^+ pairs and the rest goes in recoiling the nucleus. The ratio of the energy that goes into creating e^-/h^+ pair to the total recoil energy is called the ionization yield and is the topic of discussion for chapter 3. In either case, we have simultaneous production of e^-/h^+ pairs and phonons in the detector. When no bias voltage is applied, the e^-/h^+ pairs recombine shortly after they were created releasing additional phonons. Thus all the recoil energy is eventually recovered in the form of phonon energy. These "primary" phonons are absorbed by phonon sensors at the surface of the detector and in turn convert the phonon signal into an electronic signal proportional to the energy absorbed.

2.2.2 Signal gain

The recoil energies expected from LMDM are on the order of a few eV to a few 100s of eV (as shown in Fig. 2.2). This makes the recoil signal consistent with the noise in the detector. Hence some form of signal amplification is needed to improve the S/N of the detector. One way to amplify the signal in the detector is to make use of the Neganov-Trofimov-Luke (NTL) effect [8, 9]. The NTL effect can be understood as follows: When a bias voltage is applied to the detector, the electrons liberated from the initial scattering
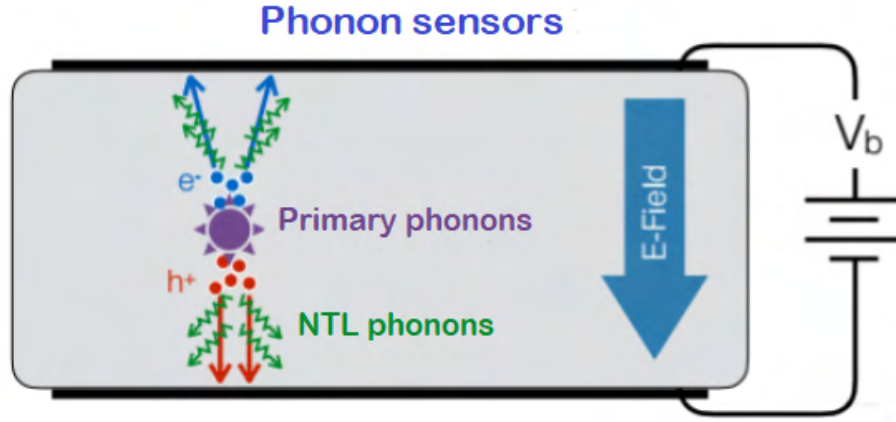
FIGURE 2.3: A schematic of the detector. The scattering process and associated primary phonons
are shown in violet. The electrons are shown in blue dots and holes in red dots. The
NTL phonons from the charge carriers as they drift along the electric field are shown
in green.

process start drifting along the lines of the electric field. The higher the bias voltage, the
faster the electrons accelerate through the crystal lattice until they reach a terminal velocity.
Any additional work from the electric field in moving the charges across the detector is
transferred to the lattice in the form of phonons which we shall henceforth call as NTL
phonons. Figure 2.3 is shown as a schematic to understand the phonon propagation and
collection in the detector. If E_r is the energy from primary recoil phonons, and E_{NTL} is
the energy from the NTL phonons, then the total phonon energy from a scattering process,
E_t is given as,

$$E_t = E_R + E_{NTL} \tag{2.4}$$

If we consider $N_{e/h}$ to be the total number of e^-/h^+ pairs drifting within the detector,
V_b to be the bias voltage, and e as the charge of an electron, then we can write the energy

from the NTL phonon as,

$$E_{NTL} = eV_b N_{e/h} \qquad (2.5)$$

Using Eq. 2.5 in Eq. 2.4, we get,

$$E_t = E_R + eV_b N_{e/h} \qquad (2.6)$$

From Eq. 2.6, we see that the amount of gain in the signal can be controlled by the bias voltage V_b. This signal gain helps improve S/N up to a certain bias voltage and thus lower the recoil energy threshold of the detector.

2.2.3 Phonon sensors and channel layout
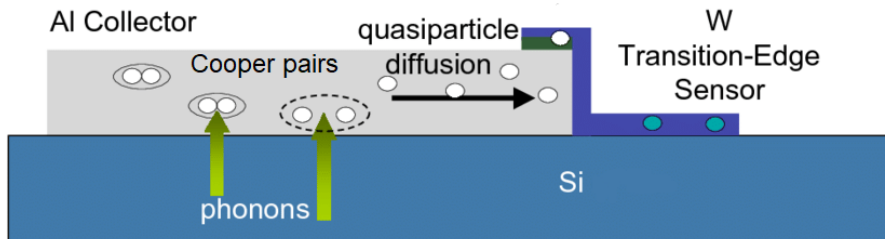
FIGURE 2.4: A schematic of the capture process of the phonons in the TES technology is shown. The while circles are the quasiparticles produced in Al and blue circles are quasiparticles produced in W [10].

The phonon sensors utilize the transition edge sensors (TES) [11] technology. They consist of two superconducting materials, Aluminium (Al) and Tungsten (W), etched photolithographically on the surface of the detector as shown in Fig. 2.4 [12]. The W layer is on top of the Al layer. The transition temperature (T_c) for Al is ∼ 1.2 K while that for W is ∼ 80 mK [13]. The detector is operated at a temperature cold enough for the Al

and W to be superconducting with the W being kept at the edge of its T_c. The Al layer
absorbs the phonons that reach the surface. If the energy of the phonons are more than the
superconducting band gap of Al i.e. $\sim$ 340 μeV, then the phonons will break the Cooper
pairs within the Al and create quasiparticles. If the energy of the phonons is less than $\sim$ 340
μeV, then it is lost and is attributed to the inefficiency in phonon detection by the sensor.
The quasiparticles then diffuse into the W layer which has a lower superconducting band
gap energy of $\sim$ 80 μeV compared to Al. They break up the Cooper pairs in W further
creating quasiparticles. The phonon energy is thus concentrated in the quasiparticles which
are trapped in the W layer. They heat up the W from a superconducting to normal state.
The sharp change in resistance, and hence current in the circuit is used as a measure to
convert the signal from the phonon energy to an electronic signal. The W is biased at 0 V
i.e. used as ground. The increase in temperature of W due to an phonon signal leads to a
decrease in Joule heating. This in turn causes the TES to cool back to its operating point.
This mechanism is known as electrothermal feedback loop.
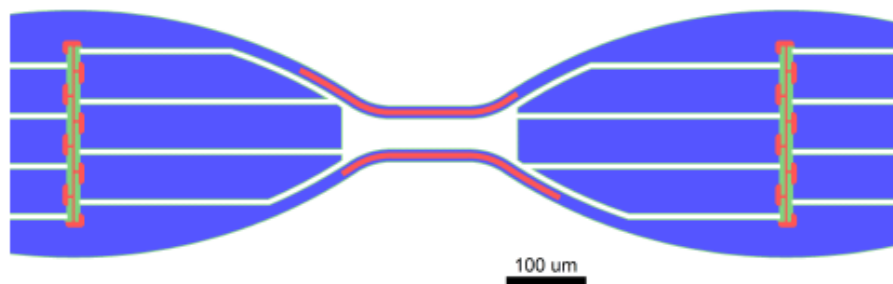
FIGURE 2.5: A schematic of the two TESs connected in a chain is shown. The blue region is Al.
            The red regions are W. The contact between the two Al fins of the TES on either side
            are shown in pink. Figure from Ref. [14]

In the Si HV detector that is used in this work, thousands of such TES sensors are etched
on one surface of the detector. For the purpose of determining the position of an interaction
within the detector, the sensors were divided into 4 channels as shown in Fig. 2.6. All

TESs within a channel are connected to one another as shown in Fig. 2.5. The channels are independently read out using superconducting quantum interference device (SQUID) based front-end amplifiers. This division of phonon sensors into four channels allow event localization in the detector. That is, we expect the pulse amplitude of the channel closest to the point of interaction in the detector to be the maximum.
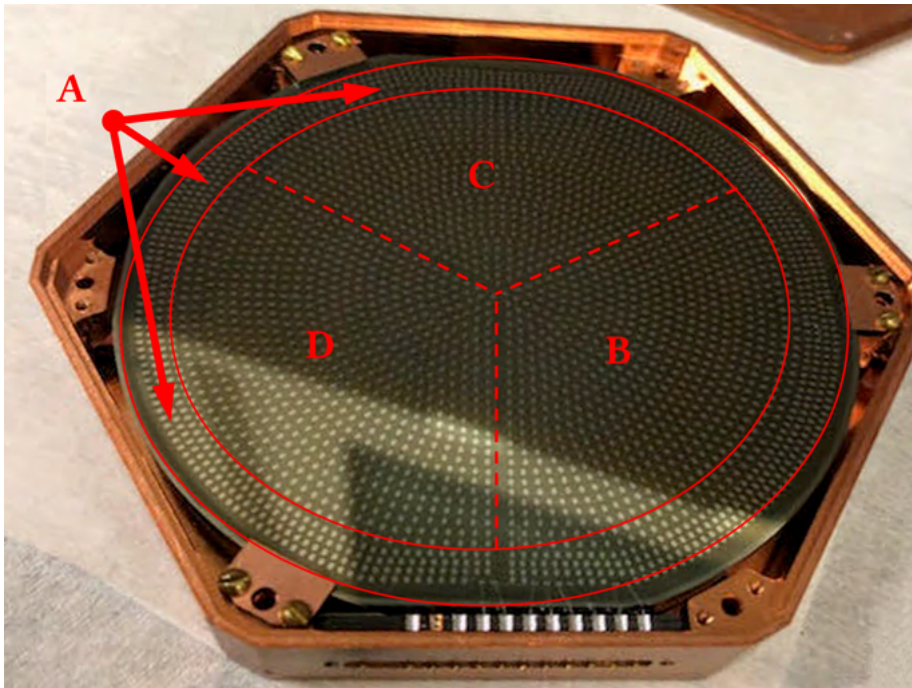
FIGURE 2.6: A picture of the 100 g silicon detector (diameter=7.5 cm and thickness=1 cm) used in this work kept inside a copper casing. The phonon sensors consist of ~1000 TES sensors. The TES sensors are divided into 4 groups of ~250 sensors and independently read out forming 4 channels (A, B, C, and D). This configuration allows reconstruction of interaction locations based on the relative amplitudes and time delays between independent channels.

2.2.4 Contact free electrode

As described in Sec 2.1.2, reducing the electronic noise will reduce the energy threshold and improve the energy resolution of the detector. The detector is being operated at
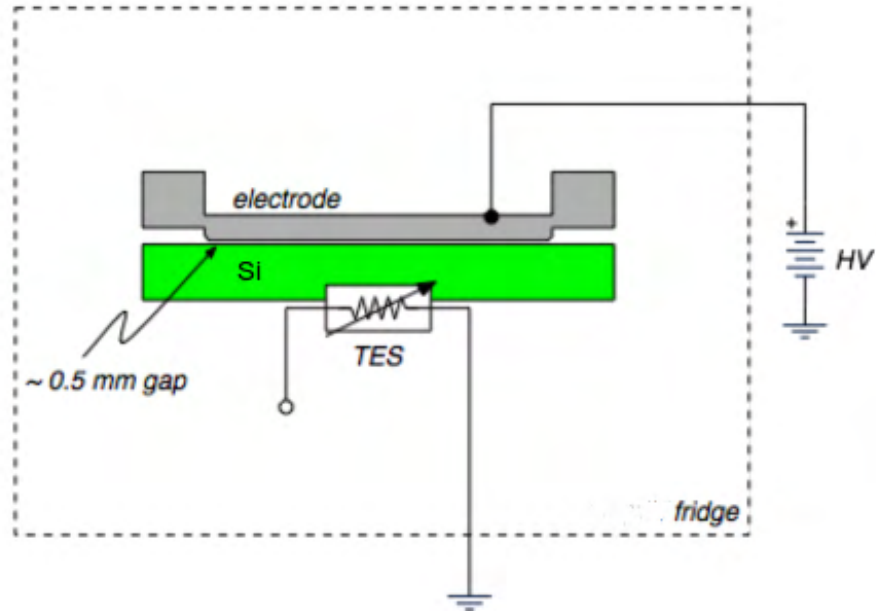
FIGURE 2.7:   A schematic of the detector showing one face covered with TES to measure phonons
produced in the crystal. The phonon sensors are held at the ground potential and the
crystal is biased through a vacuum gap using an aluminum electrode.

temperatures less than 50 mK for TES operation as described in Sec. 2.2.3. Previous

studies have indicated that the shot noise associated with the leakage charges are due to

the injection of electrons into the detector material from the metal electrodes [5]. The

electronic noise from the SQUID-based phonon readout is generally independent of the

voltage bias. Hence, following Eq. 2.6, we can expect a S/N that grows linearly with the

bias voltage. However, above a certain biasing threshold voltage, stochastic carrier leakage

into the detector, further amplified by the NTL process appears as irreducible noise. This

limits the ultimate sensitivity of NTL-phonon-assisted readout technology. The early onset

of this spurious leakage current has been the limiting factor for the sensitivity of such

detectors.

    In an attempt to reduce carrier leakage through the metal-semiconductor interface, a

method is developed whereby one side of the detector is biased through a gap of ~ 500 μm as shown in Fig. 2.7. The gap in introduced by placing a piece of cigarette paper of ~ 500 μm thickness between the bare surface of the detector and the Al electrode. This insulates the Si detector from the Al (metal) electrode. By removing the direct electrical contact between the Si detector and the Al electrode, a significant reduction of the leakage current of the detector and an improved energy resolution is expected. The other side of the detector has the TES sensors etched on them. On the TES side of the detector (that also provides the ground potential), the interface is improved by removing the amorphous-Si layer and establishing a direct Si/electrode Schottky contact. Amorphous-Si layers were historically introduced in the contact architecture to mitigate the problem of a dead-layer [6, 15]. Due to the large bias fields present for this NTL-phonon assisted detectors and the shallower dead-layer depths thereof, the advantage of those interface layers becomes almost obsolete. Eliminating the amorphous-Si will also improve the phonon absorption efficiency by the phonon sensors resulting in an enhanced S/N.

2.2.5 Summary of the detector technology

A silicon detector of mass 100 g as shown in Fig. 2.6 is fabricated. The detector had a diameter of 7.5 cm and thickness of 1 cm. The detector has thousands of phonon TES on one of its flat surfaces. The TES are etched photolithographically [12]. These phonon sensors are divided in to four channels A, B, C and D, each channel having roughly 250 sensors and covering similar surface area. The four channels are read out using SQUID based front end amplifiers. The position of interaction in the detector can be deduced from the relative amplitudes and time delays between the independent measurements made by these channels. The other flat side of the Si detector shown in Fig. 2.8 (a) is polished and left as is. An Al electrode is placed at a gap of ~ 500 μm from this surface. The voltage

bias is applied across the detector with the phonon sensors at ground potential.

2.3   Analysis of CF Si HV data

In this section we discuss the experiment setup to characterize the CF Si HV detector in terms of its phonon noise performance, signal gain, and baseline resolution. The response of the detector was measured over a range of high voltage (HV) biases to study the NTL gain in phonon signal and noise to assess the S/N in this new detector technology.

2.3.1   Experimental setup

The main components of the experiment are : (i) a Si HV detector, (ii) a laser source, (iii) an ^{55}Fe source, (iv) optical fibers, (v) a dilution refrigerator, and (vi) power supply, data acquisition (DAQ), and other readout electronics. The detector is kept inside a copper casing as seen in Fig. 2.6. This detector assembly is placed on a BlueFors LD400 pulse-tube based ^{3}He–^{4}He dilution refrigerator. A dilution refrigerator is a device that is used to cool the temperature of the detector down to a few mK. Photons of energy 1.9 eV (640 nm) are transported from a room temperature pulsed laser via a single mode optical fiber to the refrigerator where the detector is placed. The cold end of the fiber directly projects onto the polished bare surface of the detector via a gap of ∼ 1 mm under channel B of the detector. Some images of the experimental setup described above are shown below in Fig. 2.8.

To calibrate the energy scale, an ^{55}Fe source is placed under channel D, on the bare and polished surface of the detector. The detector is mounted with SQUID front-end amplifiers. The laser is pulsed synchronously with the DAQ setup to mitigate the influence of the high rates expected from the ambient radioactivity.
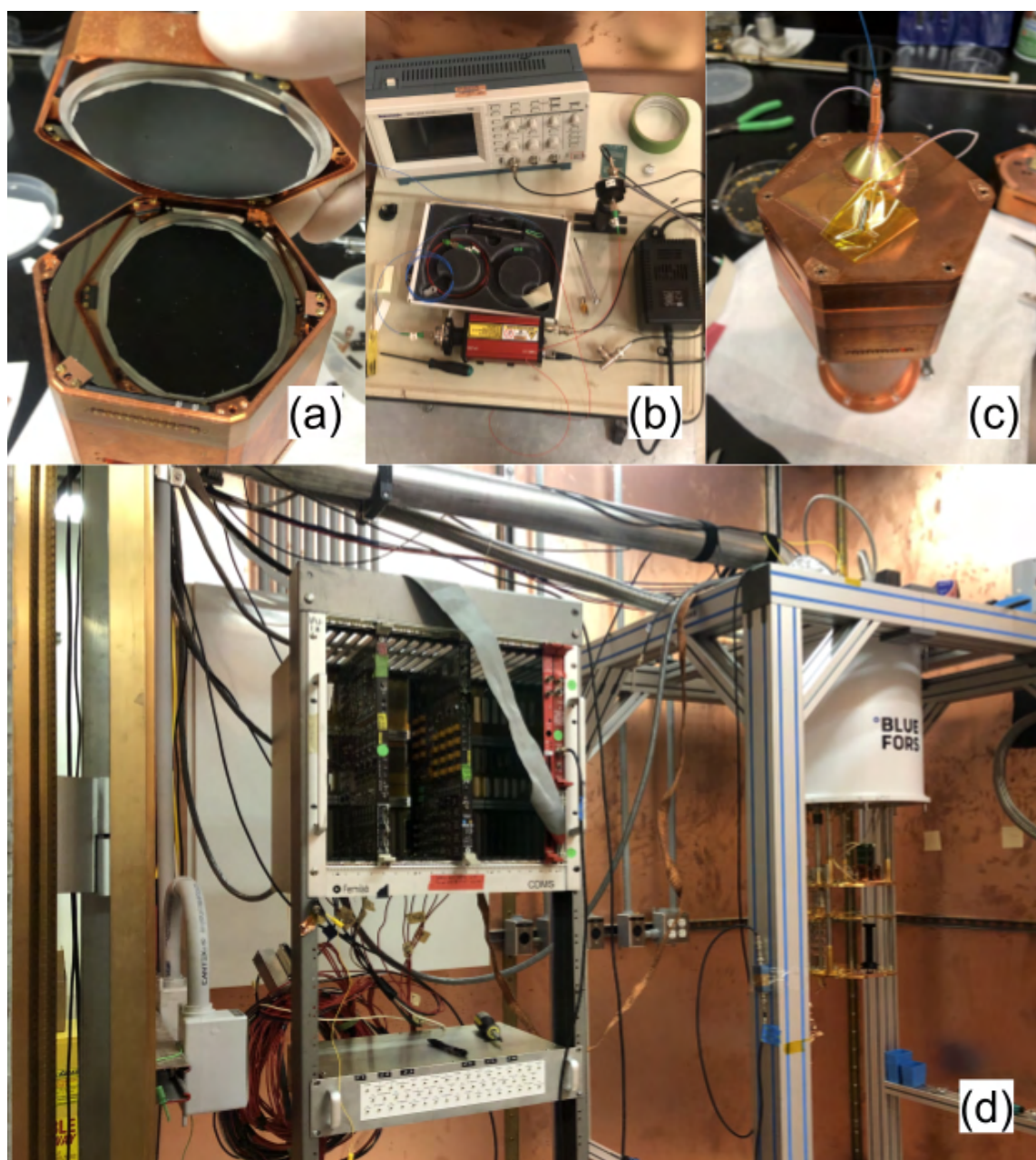
FIGURE 2.8: (a) Image of the bare polished surface of the Si detector. The Al electrode, coated in black to reduce reflection of photons, can also be seen being held above the detector. The detector is placed in its copper casing, (b) The laser setup is shown. The red box is the 640 nm laser which has two output, one is an optical fiber connection going to the detector and the other is connected to a CRO via a room temperature photodetector to look at the pulse width, (c) The laser photons passed through the optical fiber and collimated over channel B of the detector, (d) The dilution refrigerator with the detector assembly mounted on it can be seen in the far right. The associated power supply and DAQ related components are placed on the electronics rack.

2.3.2   Laser energy calibration

A single laser pulse can contain multiple photons. The energy of a laser pulse is calibrated with respect to the energy of the gammas emitted from a known source, which is the 5.89 keV gammas of an ^{55}Fe source. All four channels of the detector are read out at 0 V bias voltage. The signal gain due to the NTL effect is expected to be different for low energy laser photons to the relatively higher energy photons from the ^{55}Fe source. Hence the energy calibration is done at 0 V to avoid any systematic differences associated with this ionization quantum yield between the photons from the laser and ^{55}Fe sources. At 0 V, we expect the e^-/h^+ pairs produced by the recoils to recombine within the detector. Hence at 0 V the phonon signals are proportional to the recoil energy and independent of the ionization quantum yield. We expect two distinct peaks in the total phonon energy summed over all channels, one from the laser photons that is collimated under channel B and another from the ^{55}Fe 5.89 keV photons collimated under channel D. In Fig. 2.9 (b) we show the total phonon energy distribution summed in arbitrary units over all channels. As expected, we observe two peaks; one from the laser source and one from the ^{55}Fe source.

We take advantage of the phonon channel layout and construct two variables to estimate the location of the sources on the detector in a system similar to the X-Y Cartesian co-ordinates referred to as the X partition and Y partition. These variables are defined as:

$$\text{X partition} \quad = \quad \frac{\cos 30° \cdot pD + \cos 150° \cdot pB + \cos 270° \cdot pC}{pB + pC + pD}, \tag{2.7}$$

$$\text{Y partition} \quad = \quad \frac{\sin 30° \cdot pD + \sin 150° \cdot pB + \sin 270° \cdot pC}{pB + pC + pD}, \tag{2.8}$$

where, pB, pC and pD are the phonon amplitudes of the event in the channels B, C, and D respectively.
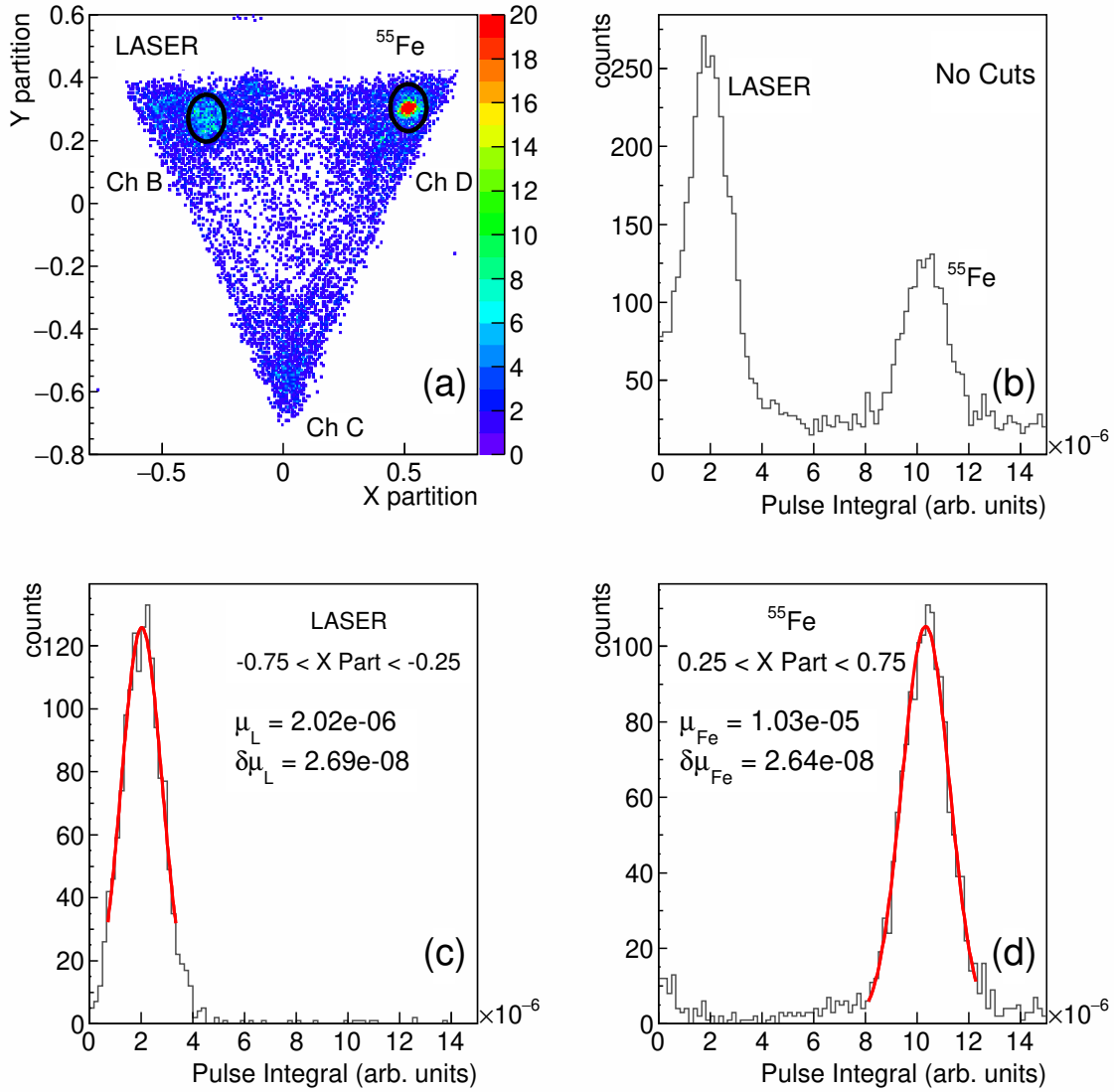
FIGURE 2.9: (a) A scatter plot of the Y partition variable against the X partition variable showing the location of laser events on channel B and ^{55}Fe events on channel D. Here the colour palettes represent the number of events in each bin. (b) the pulse integral distribution showing the laser and the ^{55}Fe peaks at 0 V. (c) The pulse integral distribution at 0 V after applying the selection cut on the partition variables to isolate the laser peak. (d) The pulse integral distribution at 0 V after applying the selection cut on the partition variables to isolate the ^{55}Fe peak. Panels (c) and (d) also show the Gaussian function fits to the peaks (red curves) along with the corresponding means (μ), the errors on the mean ($\delta\mu$) and the selection criteria used to isolate the peaks [16].

Figure 2.9 (a) shows the scatter plot of X and Y partition variables constructed based on Eq. 2.7 and Eq. 2.8. The laser and the ^{55}Fe source position can be seen as the high density blobs in Fig. 2.9 (a). To isolate the laser peak, a cut on the X partition variable defined as -0.75 < X partition < -0.25 is applied. Similarly, to isolate the ^{55}Fe peak, a cut defined as 0.25 < X partition < 0.75 is applied. A Gaussian function is fitted to the laser and ^{55}Fe peaks after applying the cuts as shown in Fig. 2.9 (c) and Fig. 2.9 (d). The average phonon energy of the laser at 0 V bias is calculated using the ratio of the laser peak to the ^{55}Fe peak and its value is found to be ∼ 1150±50 eV. The error on this value is obtained from the errors on the Gaussian fits to the two peaks.

2.3.3 Datasets

As the laser is collimated under channel B and the majority of the phonons are absorbed in this channel, henceforth we will discuss the results only from channel B. Laser data and randomly triggered noise data were taken from 0 V to 320 V at intervals of 20 V. However, we found later that the noise data at 140 V had been acquired during a high environmental noise period. Hence the data of this voltage is excluded from the analysis. The length of each waveform or trace is 2.56 ms and read out in units of current (A). Figure 2.10 shows some sample raw pulses of laser. We expect the signal to increase with voltage due to the NTL gain as seen with the pulse heights in Fig. 2.10. However, very large NTL gain at higher voltages may warm the TES from the transition region to the normal state, creating a nonlinear readout. To overcome this effect, the laser intensity beyond 100 V is reduced, with the help of the photodetector, by a factor of roughly three, from ∼ 1150 eV to ∼ 380 eV.

Two sets of data were taken at 100 V, one at each laser intensity. We see from Fig. 2.11 that the mean phonon energies in arb. units for the laser intensity at 1150 eV and 380 eV at
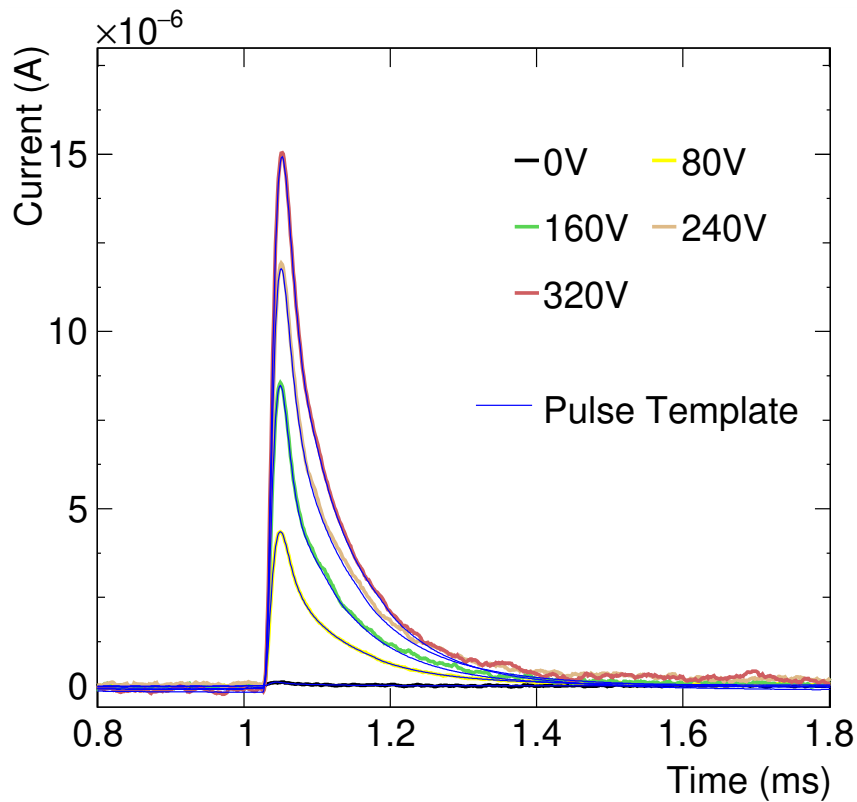
FIGURE 2.10: The phonon raw pulses as current signals in the TES as a function of bias voltages is shown. The pulses below 100 V were at a laser intensity of ∼ 1150 eV. The pulses above 100 V in the figure have been scaled to data below 100 V by a factor of 2.85. The pulse template fit to the pulses using the optimal filter (OF) method is also shown [16]

100 V are 5.15×10^{-6} and 1.81×10^{-6} respectively. The ratio of the mean phonon energies at 100 V for the two intensities i.e. 2.85, is used as a scaling factor for all data above 100 V taken with lower intensity laser.

2.3.4 Phonon noise performance

To understand the phonon noise performance of the detector, we first select 10% of the total noise events with the lowest standard deviation (STD) in their phonon baseline. This is done to remove pile-ups or pulses from the randomly triggered noise data set which may
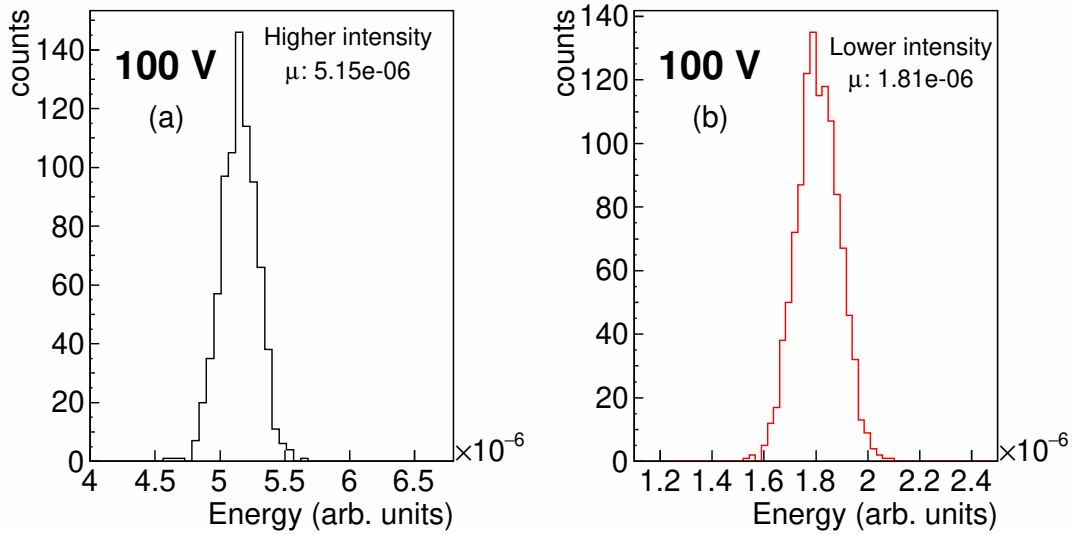
FIGURE 2.11:   The laser energy distribution and their means (μ) in arb. units is shown for the higher
intensity laser at 100 V bias in panel (a) and the lower intensity laser at 100 V bias in
panel (b).

have higher baseline STD. We assess the phonon noise performance on the basis of their

power spectral density (PSD). The power spectrum density is obtained by taking a Fourier

transform of each raw noise trace to convert it from a time domain to frequency domain.

The PSD describes the distribution of power in a signal (or noise) into components of

different frequencies. We obtain at the average PSD of the noise data at each voltage. The

noise PSD comparison across all voltages is shown in Fig. 2.12 (a). A ratio of the noise

PSDs to the noise PSD at 0 V are taken at three different frequencies, (i) low frequency

(10^3 Hz), (ii) intermediate frequency (10^4 Hz), and (iii) high frequency (10^5 Hz). We can

see in Fig. 2.12 (b) that the noise at low frequency ($\sim 10^3$ Hz) starts to increase at high

voltages indicating a gradual rise in leakage current in the detector.
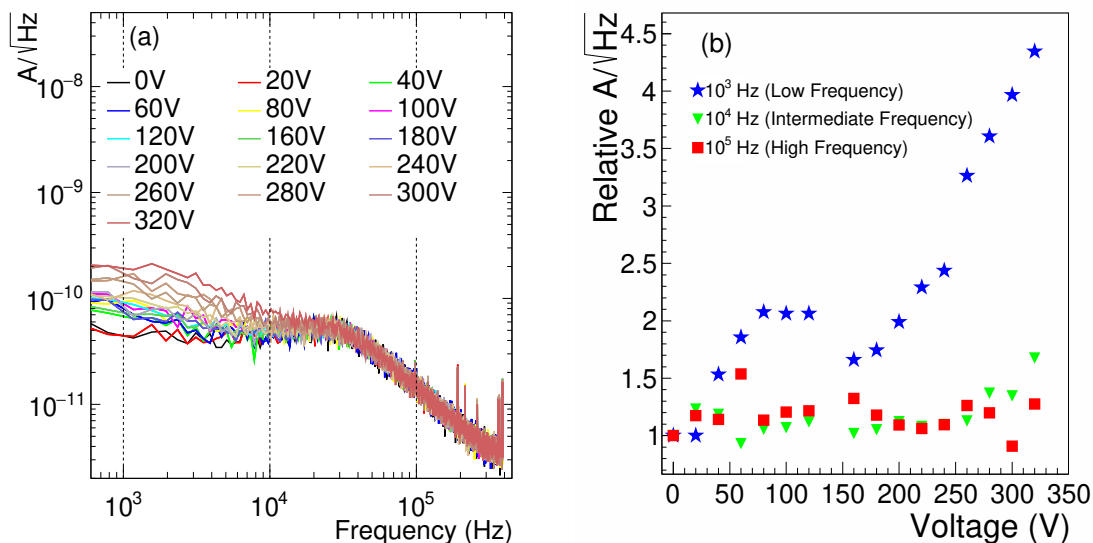
FIGURE 2.12: (a) The (TES current amplitude)/$\sqrt{\text{Hz}}$ plotted as a function of frequency for different voltages from 0 V to 320 V. These distributions are the phonon noise PSDs. (b) The ratio of the noise PSD at 0 V to the noise PSDs at every other voltage is shown at three chosen frequencies; low, intermediate and high, to assess the phonon noise performance of the detector.

2.3.5 Signal gain with voltage

The amplitudes of the laser signals are obtained using the optimal filter (OF) method [17]. The OF method requires the raw pulses, a good pulse template and the noise PSD as an input. The OF method fits the pulse template to each of the raw laser traces over the frequency domain. It uses the noise PSD to determine similar noise-like components in the raw laser pulse over the frequency domain and block them out of the fitting range. The OF method then minimizes the χ^2 of the pulse template fit to the raw laser pulse to determine the laser pulse amplitude which we refer to as the OF amplitude. More information on the OF can be found in Appendix B. The pulse template is made by averaging over some good pulses. The good pulses are defined by putting restrictions, if required, on pulse characterizing variables such as rise time, fall time, full width half maximum, peak current
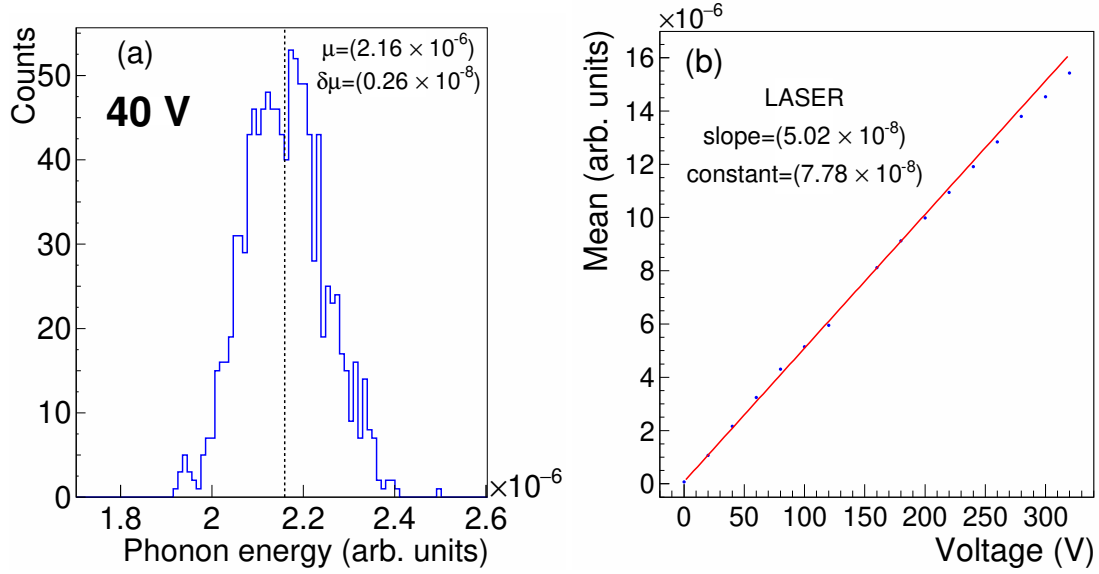
FIGURE 2.13: (a) The phonon energy distribution in arbitrary units at 40 V is shown along with its mean (μ) and error on mean ($\delta\mu$). Supplementary figures showing the phonon energy distribution at all remaining bias voltages can be found in Appendix C. (b) The mean of the laser energies in arbitrary units obtained at different voltages from 0 V to 320 V . The red line is a straight line fit to the data points. Fit parameters are also shown. Statistical errors are small and on the order of the marker size [16].

amplitude, baseline standard deviation and minimum current amplitude of the trace. Fig. 2.10 shows the pulse template fit over some laser pulses for different voltages. The OF amplitude is therefore a direct measure of the phonon energy in arbitrary energy units. We obtain the mean of the OF amplitude distribution for the laser data set at each voltage as shown in Fig. 2.13 (a). Since all the energy of the laser photons has gone into creating e^-/h^+ pairs, we can rewrite Eq. 2.6 as:

$$E_t = E_R + \frac{eE_R}{\epsilon}V_b \,, \tag{2.9}$$

where the L.H.S. is the measured total phonon energy, first term on the R.H.S. is the primary recoil phonon energy, and the second term on the R.H.S. is the signal gain from NTL effect. We can see from Eq. 2.9 that the phonon signal amplification is expected to

increase linearly with voltage due to the NTL effect [8, 9]. This linear gain in amplification is observed in Fig. 2.13 (b) up to 240 V. Above 240 V, despite the gain in phonon amplitude, the noise in the detector starts increasing more rapidly than the phonon signal thereby degrading the overall S/N.

2.3.6 Baseline resolution

The energy of the laser at 0 V was determined in Sec. 2.3.2 as 1150 ± 50 eV. If we consider the average energy to create an e^-/h^+ pair in Si with low energy photons to be equal to the band gap energy in Si (~ 1.12 eV), then a laser pulse creates ≈ 1030 e^-/h^+ pairs. However, given the energy of the laser photons (1.9 eV) is slightly below twice the Si gap and if we assume that only 1 e^-/h^+ is created per photon absorption, then the quantum yield at 0 V would turn out to be $1150/1.9 \approx 608$. Our estimate of detector resolution depends linearly on our assumption about the quantum yield for 1.9 eV laser photons. We add this as a systematic uncertainty in this work. The noise OF amplitude distribution can be converted to e^-/h^+ pair scale using the calibration factor $1150/(1.12 \cdot S_n)$ where S_n is the mean of the distribution of the OF amplitudes and n runs from 0 to 320 V in steps of 20 V as shown in Fig. 2.13 (b). The noise distributions in e^-/h^+ pair units for each voltage are fitted to Gaussians as shown in Fig. 2.14 (a). The sigma of each Gaussian is taken to be the baseline resolution of the detector at that voltage. Fig. 2.14 (b) shows the baseline resolution as a function of voltage.

To obtain the S/N ratio and relate the observed behaviour of the baseline resolutions as a function of the voltage, the functional forms for the noise (N) and signal (S) are taken to be
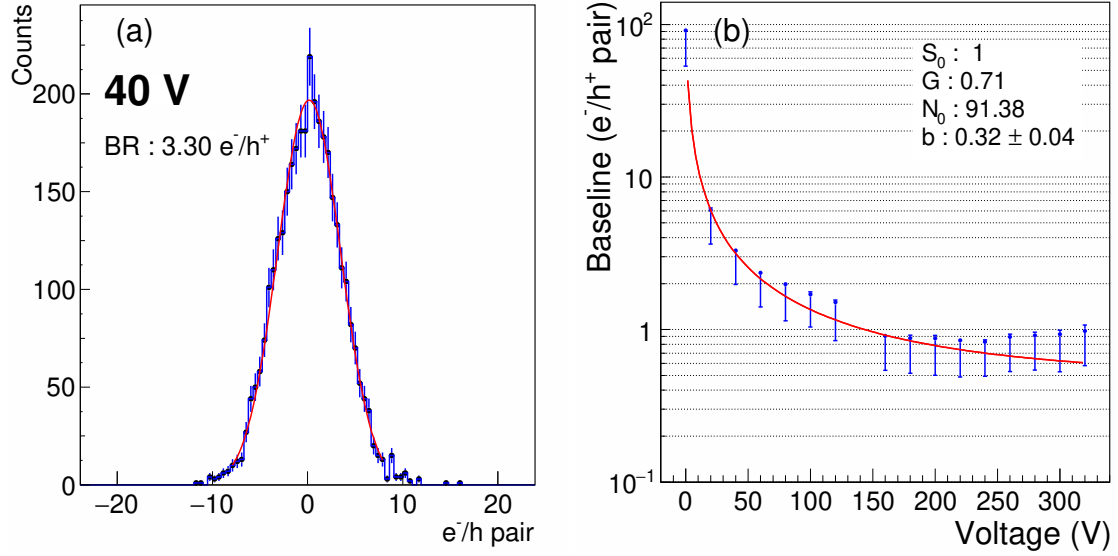
FIGURE 2.14: (a) The noise energy distribution in e^-/h^+ pair energy scale is shown. The sigma of the Gaussian fit is the baseline resolution of the detector. Supplementary figures showing the noise energy distribution at all remaining bias voltages can be found in Appendix C. (b) Baseline resolution in units of e^-/h^+ pair units as a function of voltage. The data points are fit to a functional form given by N/S where N and S are defined in Eq. 2.10 and Eq. 2.11 respectively [16].

$$N \quad = \quad \sqrt{N_0^2 + (V_b b)^2}, \tag{2.10}$$

$$S \quad = \quad S_0 + S_0 q V_b G / \epsilon, \tag{2.11}$$

where N_0 is the noise at 0 V, V_b is the applied bias voltage, b is the noise associated with the leakage current, S_0 is the normalised mean laser amplitude at 0 V, q is the charge of an electron, G is a dimensionless quantity to include the effect of the gap between the detector and the electrode (i.e. the effect of the voltage drop in series with the detector), and ϵ is the average energy required to create an e^-/h^+ pair in Si. Eq. 2.10 is modelled such that the effect of the voltage and shot noise is included in the overall noise N. Eq. 2.11 is modelled along the lines of Eq. 2.9 with the additional term G to include effect of the gap between the electrode and detector. The baseline resolution is the inverse of the S/N of the detector

at a given voltage.

We expect the S/N vs HV to be divided into 3 regions: (i) In the first region the dominant noise components are from thermal noise associated with the sensors, bias circuit, SQUIDS and electronics which are independent of the bias voltage. We expect the S/N to improve linearly in this region, (ii) In the second region the noise associated with the stochastic leakage current dominates the N and thus both noise and the signal increase linearly with voltage so that the S/N becomes independent of the bias voltage, and (iii) In the third region, the leakage current increases with the bias voltage causing the S/N ratio to decrease with bias. We expect the baseline resolution to degrade with voltage in this region. In the Fig. 2.14 (b), we see that the resolution improves up to 120 V, then plateaus, and beyond 240 V the S/N shows signs of degradation. This behaviour is consistent with our expectations. Fig. 2.14 (b) shows the S/N fit using all the available baseline resolution data points even though the fit does not represent the third region. The shot noise is generally a function of bias voltage and its functional form in the third region is not well known. Hence the fit does not accurately represent the S/N behaviour in the third region. We obtain the lowest baseline resolution of $0.83^{+0.03}_{-0.34}$ e^-/h^+ pairs at 240 V bias.

There are two systematic uncertainties associated with this result. First, and the dominant one comes from the assumption about the quantum yield. The baseline resolution at each voltage is calculated once assuming a 1.12 eV photon quantum yield, and then assuming a 1.9 eV photon quantum yield. The difference between the two baseline resolutions is taken as a systematic uncertainty. Lower quantum yield will result in a better baseline resolution. The second systematic uncertainty on the baseline resolution comes from varying the acceptable baseline STD of the pulses from 1 σ to 10 σ of its mean value. The individual systematic uncertainties are added in quadrature to obtain the total systematic uncertainty. The statistical uncertainties on the baseline resolution comes from

the uncertainties on the Gaussian fits to the noise distributions like those shown in Fig. 2.14, the error on the mean values as shown in Fig. 2.13, and the error on the average energy of a laser pulse discussed in Sec. 2.3.2. The individual statistical uncertainties are added in quadrature to obtain the total statistical uncertainty. The total uncertainty on the baseline resolution is obtained by adding the total statistical and total systematic uncertainties.

The raw pulses in the data have a bandwidth of 3 KHz. From the newfound information of the baseline resolution of this detector, we can estimate the leakage current in the detector as follows,

$$I_{noise} = \sqrt{e I_{leakage} BW}, \tag{2.12}$$

$$Q_{noise} = I_{noise} t = I_{noise}/BW, \tag{2.13}$$

$$Q_{noise}^2 = \frac{e I_{leakage} BW}{BW^2}, \tag{2.14}$$

$$I_{leakage} = \frac{Q_{noise}^2 BW}{e}, \tag{2.15}$$

where I_{noise} is the total current due to electronic noise, e is charge of an electron (1.6×10^{-19} C), $I_{leakage}$ is the leakage current, BW is the bandwidth of a laser pulse, Q_{noise} is the induced charge, t is time. The bandwidth of the laser pulse in the data is ~ 3 KHz, and if we assume a baseline resolution of 1 e^-/h^+ pair as the induced charges in the leakage current i.e. $Q_{noise} = 10^{-19}$ C, then the leakage current comes out to be on the order of 10^{-16} A. This leakage current is almost an order of magnitude smaller than an earlier work using contact free geometry on a Ge detector with a similar volume, where the lowest baseline resolution achieved was ~ 7 eV ($\sim 2.4 e^-/h^+$ pair) [5].

2.3.7 Towards the observation of single electron peaks

A new set of laser and noise data is taken at 250 V with the laser intensity tuned to roughly 1 photon per pulse. The goal was to observe the Poisson distribution of individual e^-/h^+ peaks in the laser energy distribution. The phonon energy spectrum of the laser showed a Poisson-like distribution as seen in Fig. 2.15. The distribution shows an offset with respect to 0 that is likely due to the cross talk between the trigger circuit and the readout circuit but we will investigate this further in our future detector runs with different laser wavelengths.

Considering that the laser emits a few photons during each pulse and the detector has a finite energy resolution, the phonon energy of the laser distribution can be fit to a Poisson normalized multi-Gaussian function given by the form:

$$f(x) = \sum_{\mu_n}^{N} A_{\mu_n} \left[\frac{1}{\sigma\sqrt{2\pi}} e^{-\frac{1}{2}\left(\frac{x-\mu_n+s}{\sigma}\right)^2} \right], \tag{2.16}$$

$$A_{\mu_n} = \frac{\lambda^{\mu_n} e^{-\lambda}}{\mu_n!} \tag{2.17}$$

Here the expression in the parenthesis of Eq. 2.16 are standard Gaussian functions where σ is the width, μ_n is the mean of individual Gaussians representing the number of e^-/h^+ pairs created per pulse ($\mu_n = 0, 1, 2, \ldots N$), N is the maximum number of e^-/h^+ pairs created, s is the offset, and the normalization A_{μ_n} is the Poisson probability for μ_n number of e^-/h^+ pairs to be created from a laser source that creates λ e^-/h^+ pairs on average. The value of σ was fixed by the baseline resolution of the detector at 250 V and the maximum number of e^-/h^+ created (N) was restricted to 10. All other parameters were floated. The fit of the data to this model returned a λ of 0.99 ± 0.03. The error on λ is the error on the fit. The laser energy distribution did not show individual peaks from quantization indicating the presence of factors in addition to the baseline resolution affecting the overall detector energy resolution.
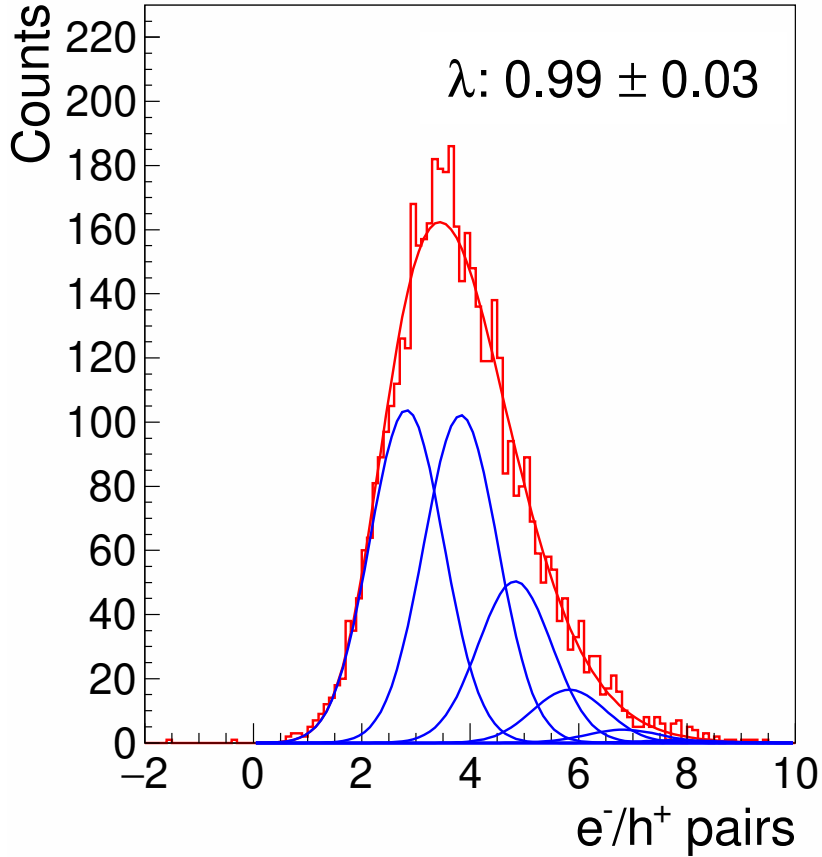
FIGURE 2.15: The red histogram is the distribution of the total phonon energy measured in the detector for the laser pulses incident on it. The red line is the Poisson-normalized multi Gaussian model fit to the distribution given by Eq. 2.16. The blue lines are the Gaussians for different number of e^-/h^+ pairs produced by the laser. The $\lambda = 0.99$ value represents the average number of e^-/h^+ pairs produced by the laser. The cross talk between the trigger circuit and the readout circuit is the likely cause for the offset observed with respect to 0.

2.4   Summary

A large mass ($\sim$ 100 g) Si phonon mediated semiconductor detector was developed and characterized. The detector achieved a baseline resolution of $\sim$ 1 e^-/h^+ pair assuming a quantum yield of $\approx$ 1030 e^-/h^+ pairs per laser pulse and a leakage current on the order of 10^{-16} A. This performance was achieved by implementing a contact free interface between

the Si detector and the Al electrode on one side. These features delayed the onset of the leakage current contribution to the noise with bias voltage while maintaining the linearity of the signal gain. The threshold voltage beyond which the linearity in signal is lost is $\sim$ 240 V, which is an improvement by a factor of 3 to previous semiconductor detectors of similar mass and dimensions [13]. The baseline resolution and leakage current in the detector is a significant improvement over earlier work with a Ge detector using contact free geometry, where the lowest baseline resolution achieved was $\sim$ 7 eV ($\sim$ $2.4e^-/h^+$ pair) [5] corresponding to a leakage current of 10^{-14} A. The cause of the offset in the energy distribution when the laser pulse energy was tuned to $\sim$ 1 photon per pulse is yet to be understood. More studies are being planned to investigate this and achieve the ultimate goal of being able to see peaks from quantization in the laser energy distribution for a large mass detector. The use of pulsed laser photons as the source also allowed for a better control over the energy to avoid TES readout non-linearity. The combination of large mass, low noise, single electron resolution detector makes the Si HV an ideal candidate for use in LMDM search and Coherent elastic neutrino nucleus scattering (CEνNS) [18] experiments. This detector is already in use at the Mitchell Institute Neutrino Experiment at Reactor (MINER) [19] to measure CEνNS. Sensitivity to single e^-/h^+ pair excitation offers unique opportunities for experiments seeking signal via nuclear recoil interactions including the possibility of background discrimination in directional direct DM searches [20].

Bibliography

[1] J.D. Lewin and P.F. Smith. "Review of mathematics, numerical factors, and corrections for dark matter experiments based on elastic nuclear recoil". *Astroparticle Physics* 6.1 (1996), pp. 87–112. ISSN: 0927-6505.

[2]   Helmuth Spieler. *Semiconductor Detector Systems*. Vol. v.12. Semiconductor Science and Technology. Oxford: Oxford University Press, 2005. ISBN: 978-0-19-852784-8.

[3]   W. Shockley. "Currents to conductors induced by a moving point charge". *J. Appl. Phys.* 9.10 (1938), pp. 635–636.

[4]   S. Ramo. "Currents Induced by Electron Motion". *Proceedings of the IRE* 27.9 (1939), pp. 584–585.

[5]   Nader Mirabolfathi et al. "Toward Single Electron Resolution Phonon Mediated Ionization Detectors". *Nucl. Instrum. Meth. A* 855 (2017), pp. 88–91.

[6]   R. Agnese et al. "Silicon Detector Dark Matter Results from the Final Exposure of CDMS II". *Phys. Rev. Lett.* 111 (25 Dec. 2013), p. 251301.

[7]   R. Agnese et al. "Projected sensitivity of the SuperCDMS SNOLAB experiment". *Phys. Rev. D* 95 (8 Apr. 2017), p. 082002.

[8]   B.S. Neganov et al. "Application of ionization to heat conversion to the light absorption spectra measurement in silicon at 1 K through adiabatic calorimetry". *J Low Temp Phys* 93 (1993), pp. 417–422.

[9]   P.N. Luke et al. "Calorimetric ionization detector". *Nucl. Instrum. Meth. A* 289 (1990), pp. 406–409.

[10] Richard Schnee. "Introduction to dark matter experiments" (Jan. 2011).

[11] K. D. Irwin et al. "A quasiparticle-trap-assisted transition-edge sensor for phonon-mediated particle detection". *Review of Scientific Instruments* 66.11 (1995), pp. 5322–5326. eprint: https://doi.org/10.1063/1.1146105.

[12] A. Jastram et al. "Cryogenic Dark Matter Search detector fabrication process and recent improvements". *Nuclear Instruments and Methods in Physics Research Section A: Accelerators, Spectrometers, Detectors and Associated Equipment* 772 (2015), pp. 14–25. ISSN: 0168-9002.

[13] Ritoban Basu Thakur. "The Cryogenic Dark Matter Search low ionization-threshold experiment". PhD thesis. Illinois U., Chicago, 2014.

[14] Mark David Pepin. "Low-Mass Dark Matter Search Results and Radiogenic Backgrounds for the Cryogenic Dark Matter Search". PhD thesis. Minnesota U., 2016.

[15] T Shutt et al. "Studies of the dead layer in BLIP dark matter detectors" (1997).

[16] V. Iyer et al. "Large mass single electron resolution detector for dark matter and neutrino elastic interaction searches". *Nuclear Instruments and Methods in Physics Research Section A: Accelerators, Spectrometers, Detectors and Associated Equipment* 1010 (2021), p. 165489. ISSN: 0168-9002.

[17] Sunil Ramanlal Golwala. "Exclusion limits on the WIMP nucleon elastic scattering cross-section from the Cryogenic Dark Matter Search". PhD thesis. Jan. 2000.

[18] Daniel Z. Freedman. "Coherent Effects of a Weak Neutral Current". *Phys. Rev. D* 9 (1974), pp. 1389–1392.

[19] G. Agnolet et al. "Background Studies for the MINER Coherent Neutrino Scattering Reactor Experiment". *Nucl. Instrum. Meth. A* 853 (2017), pp. 53–60. arXiv: 1609. 02066 [physics.ins-det].

[20] Fedja Kadribasic et al. "Directional Sensitivity In Light-Mass Dark Matter Searches With Single-Electron Resolution Ionization Detectors". *Phys. Rev. Lett.* 120.11 (2018), p. 111301. arXiv: 1703.05371 [physics.ins-det].

Chapter 3

Ionization yield measurement in Germanium

The accuracy in the results of direct dark matter search experiments rely on the precision with which the detectors can measure the recoil energy of the nucleus, after a dark matter (DM) elastically scatters off it. In detectors that produce e^-/h^+ pairs, i.e. ionization signals at the time of the scattering process, a precise understanding of the ionization yield (further elaborated in Sec. 3.1) is crucial as any uncertainty in the ionization yield translates to an uncertainty in the recoil energy measured. The nuclear recoil produced from low mass dark matter (LMDM) searches have low recoil energies. At low recoil energies the level of uncertainty in its measurement will be a key factor in the interpretation of a weak recoil signal from noise. The Super Cryogenic Dark Matter Search (SuperCDMS) is an experiment that makes use of Germanium (Ge) detectors to measure recoil energy using ionization and phonon signals [1]. The next run of SuperCDMS will be at SNOLAB,

Canada, where they will look for LMDM [2]. Thus motivating a thorough study of the inonization yield of their Ge detectors. In this chapter, we review the ionization yield in Ge in Sec. 3.1, followed by a discussion on a dedicated ionization yield measurement in Ge done by the SuperCDMS experiment from Sec. 3.2 to Sec. 3.5. The chapter concludes with the results and summary in Section 3.6.

3.1   Ionization yield in Germanium

3.1.1   Introduction to ionization yield

As described in Sec. 2.2.1, in semiconductor detectors like Ge or Si, the recoiling nucleus from the elastic scattering of a DM particle simultaneously produces e^-/h^+ pairs (ionization) and phonons. The ratio of the ionization energy to the total recoil energy from each interaction is the ionization yield of the detector. Recall Eq. 2.4,

$$E_t = E_R + E_{NTL}, \tag{3.1}$$

where, E_t is the total phonon energy measured by the detector, E_R is the recoil energy of the nucleus, and E_{NTL} is the energy of the NTL phonons. If we consider E_Q to be the energy used to create e^-/h^+ pairs i.e. the ionization energy, then we can define the ionization yield Y as,

$$Y = \frac{E_Q}{E_R} \tag{3.2}$$

Now, if the number of charges produced in the initial scatter is $N_{e/h}$, and ϵ is the average energy to create an e^-/h^+ pair in Ge, then,

$$N_{e/h} = \frac{E_Q}{\epsilon} = \frac{YE_R}{\epsilon} \tag{3.3}$$

If e is the charge of an electron, and V_b is the applied bias voltage across the detector, then recalling Eq. 2.5, the energy from the NTL phonons is given by,

$$E_{NTL} = eV_b N_{e/h} = \frac{eV_b Y E_R}{\epsilon} \tag{3.4}$$

Thus, Eq. 3.1 can be rewritten as,

$$E_t = E_R + \frac{eV_b Y E_R}{\epsilon} = E_R \left(1 + \frac{eV_b Y}{\epsilon} \right) \tag{3.5}$$

Or, we can rewrite Eq. 3.5 as,

$$E_R = \frac{E_t}{(1 + eV_b Y / \epsilon)} \tag{3.6}$$

Among all the terms in Eq. 3.6, E_t and Y are the main contributors to the uncertainty in E_R. The uncertainty in E_t is the detector resolution, which is a small factor ($\sim 0.2\%$) in semiconductor detectors [21]. The term that dominates the uncertainty in E_R is Y. This motivates the need to have a precise understanding of the ionization yield in rare event searches for accurate recoil energy measurements. In the 1960s, Lindhard et al., theoretically derived the ionization yield in a material [16–19] as part of a comprehensive study on the collisions of ions with atoms. The ionization yield has been shown to depend on the mass number of the target material, type of interacting particle, and possibly the temperature of the target material [20, 22]. Figure 3.1 shows the results of several experiments that have measured the ionization yield in Ge, as a function of the nuclear recoil energy [3–15, 23]. We see that the ionization yield increases with recoil energy.

3.1.2 Need for a dedicated ionization yield measurement

Experiments often compare their ionization yield measurements to the predictions by Lindhard et al. [16–19] shown as the solid blue line in Fig. 3.1. This is because the
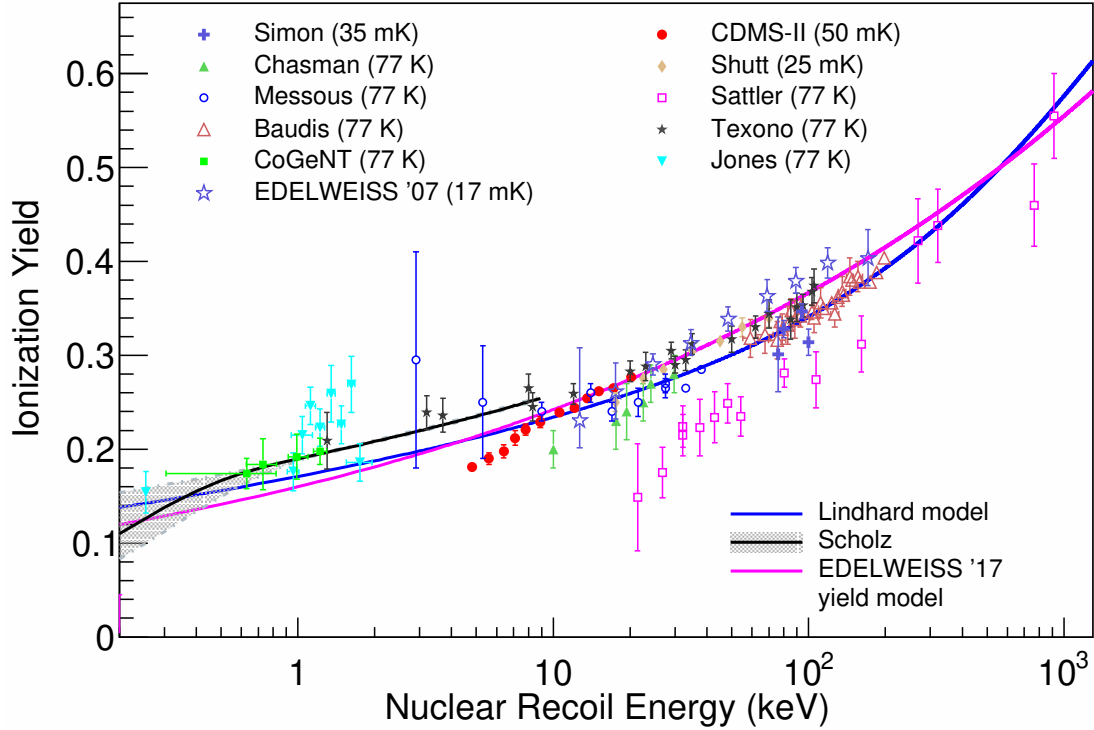
FIGURE 3.1: World data on ionization yield measurements as a function of recoil energies in Ge [3–15]. Measurements by Schutt, Simon, EDELWEISS, CDMS-II and Scholz are in the mK scale temperature, while all others are at 77 K. The prediction by Lindhard et. al. [16–20] has also been shown for comparison.

Lindhard 'model' has been in good agreement with several measurements in describing the behaviour of the ionization yield as a function of recoil energy, and provided a means to directly compare experimental results with theory. However, for LMDM, the expected nuclear recoil energies are low (< 10 keV). As pointed out by Lindhard et al. in Ref. [17], effects of the atomic binding energy on the ionization yield, which is neglected by the authors in their derivations, become more prominent for low energy nuclear recoils. In Fig. 3.1, we observe that the measurements at low nuclear recoil energies deviate more from the Lindhard model than at higher energies. Additionally, the Lindhard model does not consider any temperature dependence, which in theory should affect the band gap

of the material, and hence the ionization yield [22]. The SuperCDMS is a direct dark matter search experiment that will look for LMDM at SNOLAB using Ge high voltage (HV) detectors [24]. The HV detectors are operated at < 50 mK temperature. The HV detectors cannot directly measure the ionization yield on an event-by-event basis. As seen in Fig. 3.1, very little experimental data exists of ionization yield measurements at the mK scale temperatures for recoil energies less than 10 keV. This coupled with the limited accuracy of the Lindhard model at low energy nuclear recoils, makes it necessary to have a dedicated study of the ionization yield in Ge for SuperCDMS. The precision in the understanding of the ionization yield in SuperCDMS detectors will help reduce the uncertainty in their results for dark matter searches at SNOLAB.

3.2 Experimental Setup and datasets

3.2.1 Photo-neutron calibration concept
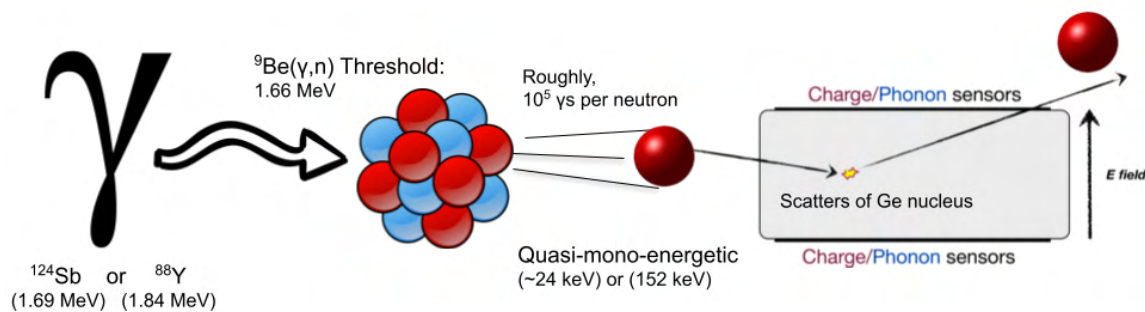
FIGURE 3.2: A schematic representation of the method used to obtain the ionization yield in Ge by the SuperCDMS experiment.

A common method of measuring the ionization yield is to make use of monoenergetic neutron sources [5, 13–15]. One of the ways to produce mono-energetic neutrons is by using a gamma-source along with ^{9}Be. The energies of the prominent gamma lines from

these sources should be above the threshold energy of 1.66 MeV to initiate a Be(gamma,n) reaction to produce the monoenergetic neutrons [25]. We call the neutrons thus produced as photo-neutrons. The energy of the photo-neutrons emitted can be calculated theoretically as [26],

$$E_n = \frac{A}{A-1}\left[E_\gamma - E_{th} - \frac{E_\gamma^2}{(1862MeV)(A-1)}\right] + \delta(\theta), \tag{3.7}$$

where, E_n is the energy of the emitted photoneutron in MeV, A is the mass number of the target material, E_γ is the energy of the incoming gamma in MeV, E_{th} is the threshold energy in MeV for a (gamma, n) reaction in the target material, and $\delta(\theta)$ is a small spread in the energy of the emitted neutron which is a function of the angle θ between the direction of the incoming gamma and the emitted neutron. This angular spread can be defined as [26],

$$\delta(\theta) = E_\gamma \cos\theta \left(\frac{2(A-1)(E_\gamma - E_{th})}{931A^3}\right)^{1/2} \tag{3.8}$$

The method used by SuperCDMS involves measuring nuclear recoil energy in Ge detectors from monoenergetic photo-neutrons of known energy. Two gamma sources [88]Y, and [124]Sb were used separately, both with an activity of 1 mCi as on 1 April, 2015. The [88]Y emits 1.84 MeV gammas which when incident upon [9]Be produce neutrons in the range of 151-159 keV depending upon the neutron production angle. Likewise [124]Sb emits 1.69 MeV gammas producing neutrons in the range of 22.8-24.1 keV. During the discussion of the experimental setup in Fig 3.3, we will see that only neutrons in the forward direction reach the detectors, and the solid angle subtended by the detectors is very small. The neutrons reaching the detector from the [124]Sb[9]Be and [88]Y[9]Be sources are considered quasi-monoenergetic sources for the analysis in this experiment. These quasi-

monoenergetic neutrons elastically scatter off a Ge nucleus within the detector causing it to recoil. Neutrons from the ^{124}Sb^{9}Be source produces a maximum recoil energy of 1.3 keV and the ^{88}Y^{9}Be source produces a maximum recoil energy of 8.5 keV from a single scatter neutron. By studying the recoils of Ge nuclei from these quasi-monoenergetic neutrons (single and multiple scatter), the measured total phonon energy E_t of our detectors can be calibrated to the recoil energy E_R. This can be achieved by simulating the expected E_R distribution in the detector, then folding it with a yield function $Y(E_R)$ to obtain the simulated E_t distribution, and by fitting this simulated E_t distribution to the measured E_t distribution using a likelihood method. The yield function that will be used in this study is a modified Lindhard model which will be explained in more detail in Sec. 3.5. This model will have a few parameters whose best fit values will be determined by the fit from the simulated E_t to the measured E_t. Using the best fit values of the parameters, we can obtain the ionization yield of the SuperCDMS Ge detector as a function of recoil energy.

3.2.2 Experimental Setup

Figure 3.3 (a) shows the schematic of the experimental setup. There were 15 Ge detectors, each with 3 inch diameter, 1 inch thickness, and with a mass of $\sim$ 600 gms. Figure 3.4 (a) is an image of the detector. The detector has four phonon channels as shown by the schematic in Fig. 3.4 (b) labelled as A, B, C, and D. The detectors can be operated in two modes, (i) iZIP [30], and (ii) CDMSlite (or HV) [31]. In the iZIP mode the bias voltage is at 4 V . iZIPs allow direct measurement of the ionization yield of the detector as it measures ionization and phonon signals separately. In the CDMS low ionization threshold experiment or CDMSlite mode the detectors are biased at voltages much higher than those for the iZIPs and only the phonon signals are measured. Ionization is measured indirectly through the NTL phonons. This significantly lowers the recoil energy threshold of the
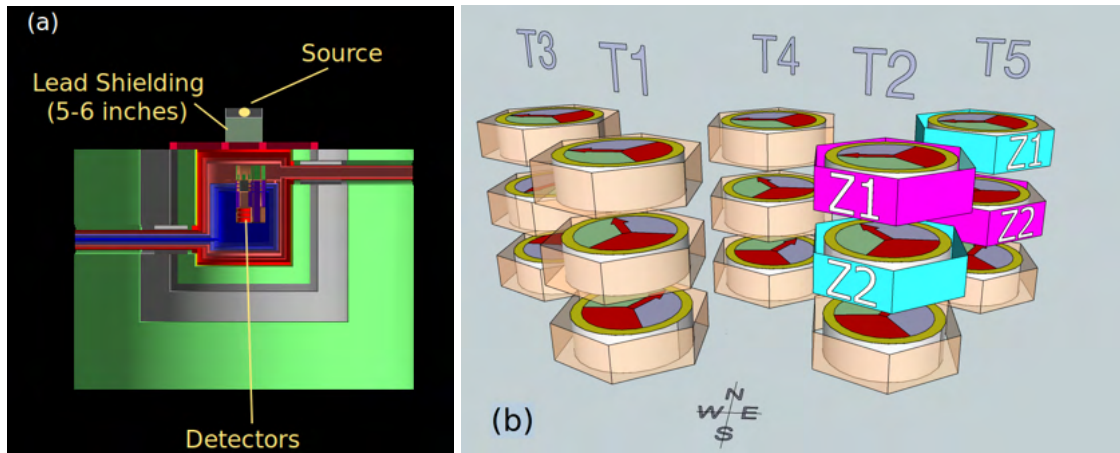
FIGURE 3.3: (a) A GEANT4 schematic of the experimental setup with the shielding configuration. Poly-ethylene (shown in green) is used to shield against neutrons, and lead (shown in gray) against gammas. (b) The 5 tower setup with 3 detectors in each tower. The photo-neutron source (gamma+^{9}Be) is placed above towers 2 and 5. The T2Z1 and T5Z2 detectors used in this analysis have been highlighted in pink [27].

detector, but at the cost of directly measuring the ionization yield. The detectors were arranged in 5 towers with 3 detectors in each tower as shown in Fig. 3.3 (b). All detectors except two, labelled as T5Z2 (second detector in tower 5) and T2Z1 (first detector in tower
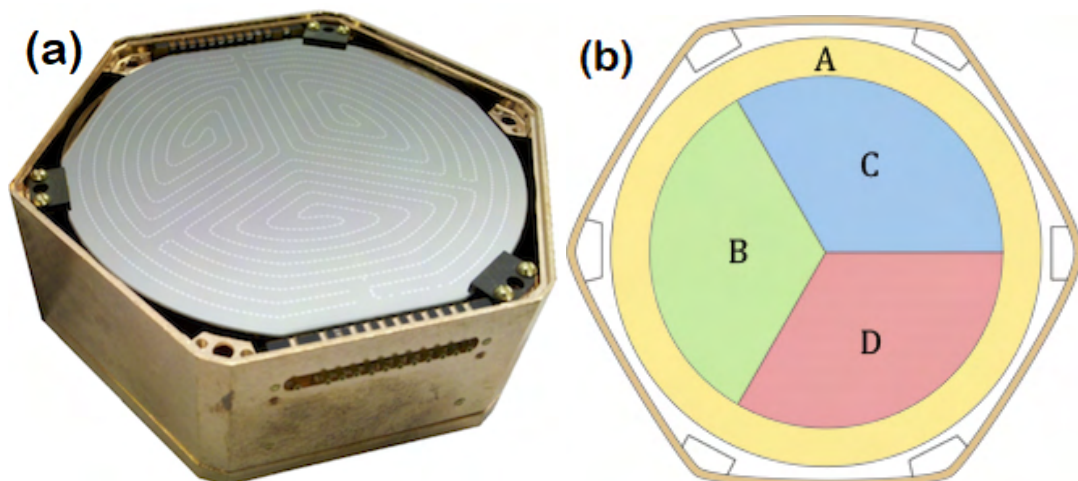
FIGURE 3.4: (a) A Germanium SuperCDMS detector in its Copper housing [28], (b) A schematic of the detector with the phonon channel layout [29].

2) in Fig. 3.3 (b) were operated in iZIP mode. In this study, the T5Z2 and T2Z1 were used. They were operated at 70 V and 25 V, respectively in CDMSlite mode. These two detectors were chosen as they showed the best signal to noise performance when biased at higher voltages. Simulations of the neutron spectrum from the two detectors were done to determine the best position of the source. The photo-neutron source was placed above and between the towers 2 and 5 which contain the T2Z1 and T5Z2 detectors. Given the activity of the gamma sources, we expect $\sim 10^5$ γs for each neutron from the photo-neutron source. To counter the high rate of these γs from the source 5 to 6 inches of lead shielding was placed between the photo-neutron source and the detectors at different stages of the data taking run. The thickness of the lead shielding between the source and the detectors were optimised from simulations such that there is no degradation of the neutron energy as they reach the detectors. Also the energies of any additional gammas and electrons created in the lead due to the photo-neutron sources were found to be well below the energy threshold attainable by the Ge detectors.

Figure 3.5 (a) shows the top view of the SuperCDMS Soudan experimental setup [1]. The ice box (i.e. the unit in which all the towers are placed and connected to the cryogenic cooling system) is shown with a schematic of the tower configuration overlayed. Towers 2 and 5, which is used in this study, have been highlighted. Figure 3.5 (b) shows the ^{9}Be disk placed underneath the gamma-source rod. Figure 3.5 (c) shows the source box setup. The source rod can be unscrewed to remove and swap the gamma sources. A side view of the source box with the lead shielding placed between the source and the top of the ice box is seen in Fig. 3.5 (d). The source box is kept on a bridge. Figure 3.5 (e) is a top view of the source box resting on the bridge. The position of the source box is such that it is above towers 2 and 5.

FIGURE 3.5: (a) Top view of the SuperCDMS Soudan ice box, (b) top view of the gamma source rod with the ^{9}Be wafer underneath. The gamma source is placed within the source rod, (c) the source box with the detachable source rod, (d) side view of the source box with the lead shielding to counter the high gamma rate from the source, and (e) top view of the source box placed on a bridge above detector towers 2 and 5.

3.2.3 Datasets
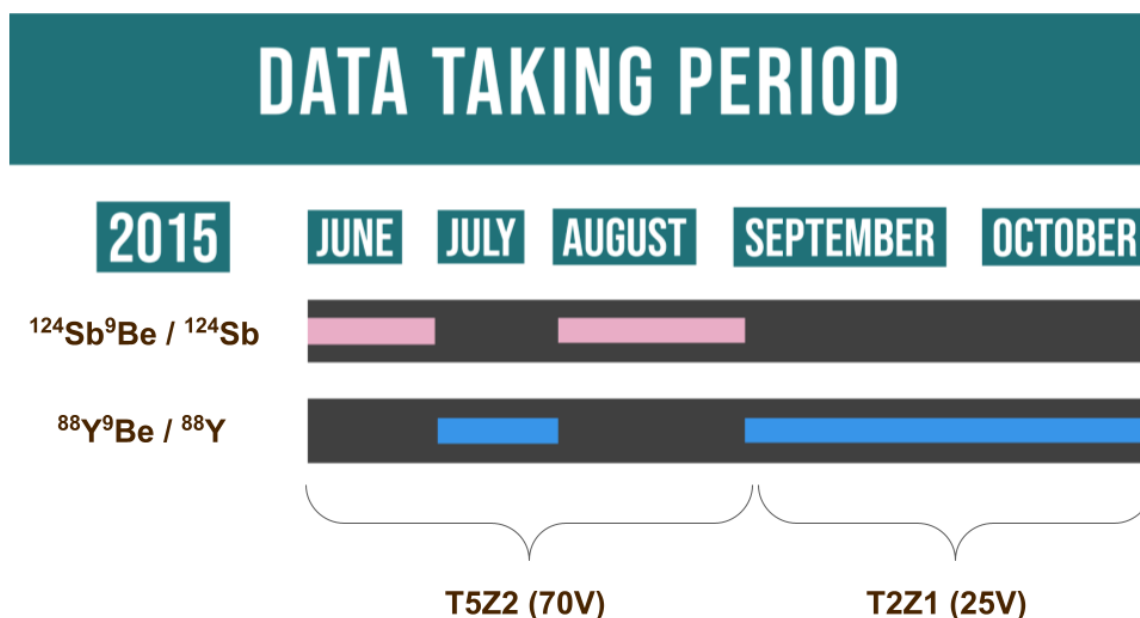
FIGURE 3.6: A timeline of the photo-neutron data taking run showing the different datasets used in this study.

The photo-neutron run was taken for 144 day between 5 June, 2015 and 26 October, 2015. Figure 3.6 gives the photo-neutron data taking timeline. There were two modes of data taking, (i) neutron-ON, and (ii) neutron-OFF. Data taken with the ^{9}Be wafer is called neutron-ON, and without the ^{9}Be wafer is called neutron-OFF. In the neutron-ON dataset, photo-neutrons are produced as described in Sec 3.2.1, while the neutron-OFF dataset is useful in understanding the gamma background. Both neutron-ON and neutron-OFF datasets were taken for each of the gamma sources i.e. ^{124}Sb and ^{88}Y. There are datasets with three different source configurations, (i) A total of 64 days of data with the ^{124}Sb neutron-ON and OFF mode combined using the T5Z2 detector biased at 70 V, (ii) A total of 42 days of data with the ^{88}Y neutron-ON and OFF mode using the T5Z2 detector biased at 70 V, and (iii) A total of 38 days of data with the ^{88}Y neutron-ON and OFF mode using

the T2Z1 detector biased at 25 V. There were some intermittent calibration runs for the iZIPs with the ^{252}Cf neutron source at which point the T5Z2 and T2Z1 detectors were also exposed to it. There were also some runs taken with no source to study the background rate of the environment. Noise data was taken by randomly triggering on events before, after and in-between the photo-neutron runs. The neutron-ON datasets were used to obtain the measured total phonon energy E_t. The neutron-OFF datasets, the ^{252}Cf datasets, and the no source datasets were used to model the background distribution in the likelihood method.

3.3   Data selection criteria

The raw data comprises of several traces recorded by the data acquisition system (DAQ). Each trace corresponds to an event read out by a phonon channel which is 6 ms long and the pulse amplitude recorded in units of current. The data was processed using the optimal filter (OF) method [32, 33]. The energy scale was calibrated to keV using the K and L shell electron capture lines in ^{71}Ge at 10.1 keV and 1.3 keV respectively [33–35]. The data was then subjected to several event selection criteria to filter good events. The selection criteria (or cuts) can be broadly divided into 2 groups, (i) basic cuts, and (ii) quality cuts. Cuts that largely deal with ensuring the consistency of the run conditions (hardware and DAQ) are called basic cuts. They are applied directly on the value of a related variable obtained after the data is processed. These cuts are summarized in Sec. 3.3.1. Quality cuts are those which filter events mostly on the basis of the goodness of their pulse shapes when compared to relevant pulse shape templates. They require certain analysis and are explained in Sec. 3.3.2.

3.3.1   Basic Cuts

Bias flashtime

Long and continuous periods of data-taking can lead to charges getting trapped within the detector possibly due to crystal defects. This affects the effective electric field within the crystal. Therefore the detectors were periodically flashed with infrared light (energy ~ band gap energy of Ge = 3 eV) to remove charges trapped within the Ge crystal. The T5Z2 detector was flashed every 3300 secs while the T2Z1 detector was flashed every 10800 secs. The interval between flashes is decided based on the activity of the source, and the applied bias voltage. As the data with T2Z1 was taken roughly 3 months after starting the photo-neutron run, and also at a reduced bias voltage, the flashing interval was increased. Events recorded in periods of data taken above the specified flashing interval for each of the detectors were discarded.

Base temperature

The detectors are operated between 35 to 55 mK with the help of a dilution refrigerator. The base temperature of the detector is recorded for each event. There are instances when the base temperature is not read out properly by the DAQ and is recorded by a value < 0 K. All events with improper read out of the base temperature, and fluctuation beyond the acceptable operating temperature range were removed.

Bias voltage

The Ge HV detector utilizes the NTL effect which is driven by the applied bias voltage. Fluctuations in bias voltage will affect the energy scale (i.e. E_t) as shown in Eq. 3.5. Any events recorded when the T5Z2 detector was not at biased at 70 V, or the T2Z1 detector was not biased at 25 V were removed from the analysis.

Zero current and leakage current

The Ge HV detectors have a leakage current on the order of a few nA. This leakage current can get excessive if the data is taken too soon after the previous flashing of the detector with infrared light. A cut was applied, similar to the CDMSlite WIMP search analysis, to ensure all recorded events have a leakage current below 3 nA [1]. In case of improper read out, the leakage current is recorded by a value of 0 A. All events with zero leakage current values are also discarded.

Bad series

The DAQ would bunch the raw data in regular time intervals, and each of these bunch is called a data series. There were a few series of data which exhibited unusual behavior when compared to the rest of run. The abnormalities were in the form of sudden change in the phonon noise, or a burst in the trigger rate of events for a very short period at the time of swapping or removing the photo-neutron sources. All such data series were removed.

Phonon delay window

There can be a delay between the start of a pulse and the start of the trigger window. Ideally these two starting points should coincide if a good pulse is to trigger the event. The OF method tries to find the peak of a phonon signal to fit the pulse template over the entire length of the trace. For this analysis, the time window for the OF method to search for the peak is centered at the starting point of the trigger, and the allowed window was taken to be between -195 μs and 35 μs. The values of the upper and lower bounds of the delay time window were adopted from a previous CDMSlite analysis [33]. The cut is applied to removed pile ups or poorly reconstructed energies from phonon signals outside the delay window.

Pre-pulse baseline standard deviation

The pre-pulse region is the part of the pulse before the start of the trigger window. The baseline of the pre-pulse region is an indicator of the noise level in the detector. A cut is applied to remove events which show beyond 4σ standard deviation of the baseline during a run. This cut was set separately on the baselines of each phonon channel.

Analysis threshold

The analysis threshold in this study was taken as the energy at which the trigger efficiency was 100%. As only one detector at a time was used in the photo-neutron measurements, the trigger efficiency was obtained by a method previously used by the CDMSlite [33] analysis. The general idea is to make use of ^{252}Cf source with a full tower readout, and matching trigger settings to those used in the photo-neutron runs. The full tower has 3 detectors. The ^{252}Cf source was used as it has a continuous neutron energy distribution up to a few MeV and could trigger multiple events in the full tower read out. Consider tower 2, with T2Z1 being the detector that was used in the photo-neutron run. The method for calculating the trigger efficiency is as follows:

$$\text{Efficiency} = \frac{\text{(Trigger in T2Z1 AND T2Z2) OR (Trigger in T2Z1 AND T2Z3)}}{\text{Trigger in T2Z2 OR T2Z3}}$$

Here, there numerator is the number of triggers issued simultaneously by at least two detectors from the tower, one of which must be T2Z1. The denominator is the number of triggers issued by any detector except T2Z1. This fraction is the trigger efficiency of T2Z1. The analysis threshold for the data taken with the T5Z2 detector is 1.8 keV, and the T2Z1 detector is 2.2 keV.

3.3.2   Quality Cuts
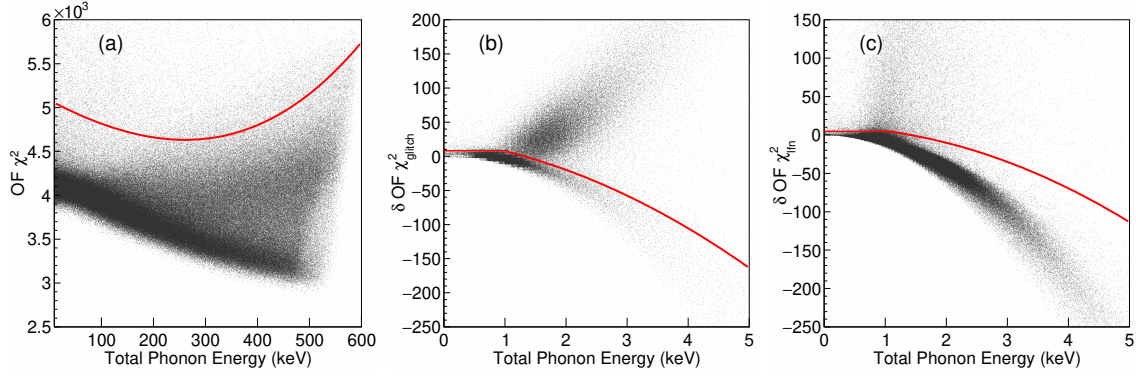
FIGURE 3.7: (a) Events in the phonon OF χ^2 parameter space, (b) Events in the phonon OF $\delta\chi^2$ LFN parameter space, and (c) Events in the phonon OF $\delta\chi^2$ glitch parameter space. The solid red line in each of the panels shows the criteria for event selection in the respective parameter spaces.

Phonon OF χ^2

For the OF method, a phonon pulse template is made from the phonon signals. The phonon pulse quality is determined by the goodness of fit (χ^2) of the template to each individual phonon pulse in the dataset. This is called as the Phonon OF χ^2 and its value for each event is stored as variable in the processed data. The cut on the phonon pulse shape is set in the phonon OF χ^2 vs phonon energy parameter space for each dataset. As shown in Fig. 3.7 (a) there is a band of events around OF χ^2 values of 4000. The X axis is divided into several windows of energy with equal interval. The cumulative distribution function (CDF) of the phonon OF χ^2 is computed within each of the energy windows. A third order polynomial is fit through the 97% CDF limit in each of the energy window. The red solid line in Fig. 3.7 (a) shows this polynomial for the ^{88}Y^{9}Be data taken with T2Z1 at 25 V bias voltage. All events with an OF χ^2 value above the polynomial curve are rejected from the analysis.

Charge χ^2

The Ge HV detector has both phonon and charge channel read out. The charge energy information is not used directly in this analysis. However as a sanity check a cut is applied on the OF χ^2 of the charge template fit to the charge signals. This is done to avoid any unknown co-relation between bad charge signals and the phonon read outs. The flat cut of charge OF $\chi^2 < 6250$ was set. This value was chosen as charge pulses above this χ^2 value were dominated by electronic glitches.

Glitch cut

Glitches can be defined as signals with nonphysical origins. They have a different shape than that of phonon pulses from an electron recoil or a nuclear recoil. Glitches in the data were removed in two ways, (i) by restraining the difference in the number of triggers issued by the phonon and charge channel readouts, and (ii) applying a condition on the pulse shape. When an event is triggered, the DAQ records which detectors triggered in both the charge and phonon channels within 1 msec of the trigger time. This information is stored in variables called as 'ntrigp' and 'ntrigq'. These quantities are defined as the total number of phonon (ntrigp) or charge (ntrigq) trigger produced from all the sides of the detectors that were read out during the run. In the photo-neutron run, the maximum number of triggers that can be issued are 12 (i.e. 2 sides of each detector read out from towers 2 and 5). The quantity Δntrig is then defined as follows:

$$\Delta\text{ntrig} = \text{ntrigp-ntrigq}$$

Since a true recoil event should ideally produce triggers in both the charge and phonon channels, the idea of the cut is to remove events for which too many detectors produced a

phonon trigger without an accompanying charge trigger. The cut was set to remove events
which had Δntrig< 4. This value was adopted from a previous CDMSlite WIMP search
analysis [33]. An examination of the raw phonon traces for events with Δntrig≥ 4 showed
several of them to have features identified as instrumental artifacts.

In addition to the cut on the number of triggers, glitches were also removed based on
the goodness of the pulse shape. Similar to the phonon pulse template, a glitch template
was also made by sampling glitch events in the datasets. The glitch template was then
passed onto the OF method in place of the pulse template and the goodness of fit of each
event, given by the OF method i.e. OF χ^2_{glitch} was stored in a variable. The difference in
the OF χ^2 (i.e. the OF $\delta\chi^2_{glitch} = \text{OF}\chi^2_{glitch} - \text{OF}\chi^2_{pulse}$) between the pulse template fit
and the glitch template fit to the raw pulse was examined as a function of phonon energy
as shown in Fig. 3.7 (b). The more positive the $\delta\chi^2_{glitch}$ the more glitch like the event,
while a more negative $\delta\chi^2_{glitch}$ would indicate higher possibility of a good phonon pulse.
A cut was made in the $\delta\chi^2_{glitch}$ vs phonon energy parameter space as shown in Fig. 3.7
(b) which is a combination of a straight line ($y_1 = c_1$) and a second order polynomial
($y_2 = a_2x^2 + b_2x + c_2$). For the straight line cut, the 3σ of the noise distribution in the
$\delta\chi^2_{glitch}$ plane was used to set the value of c_1. the polynomial cut was set by dividing the X
axis in Fig. 3.7 (b) into several energy windows of equal interval. The $\delta\chi^2_{glitch}$ distribution
in each energy window was fit with a Gaussian. A second order polynomial was fit to
the 3σ values in each energy window. The events in the analysis must satisfy the Δntrig
condition, the straight line and the second order polynomial cuts. All events below the
solid red line in Fig. 3.7 (b) are accepted in this analysis.

$\delta\chi^2$ LFN (low frequency noise)

Similar to the $\delta\chi^2_{glitch}$ cut for the glitches, an OF $\delta\chi^2_{LFN}$ cut was also set for removing LFN events. The goodness of fit by the OF method between the pulse template and an LFN template were stored in variables, and their $\delta\chi^2_{LFN}$ values were constructed. A straight line and a second order polynomial cut was set following an identical procedure as described for the $\delta\chi^2_{glitch}$ cut for glitches. Only this time the cut was set in the OF $\delta\chi^2_{LFN}$ for LFN vs phonon energy parameter space as seen in Fig. 3.7 (c). All events above the solid red line in Fig. 3.7 (c) were removed as they are indicative of LFN-like behaviour.

3.3.3 Cut efficiency
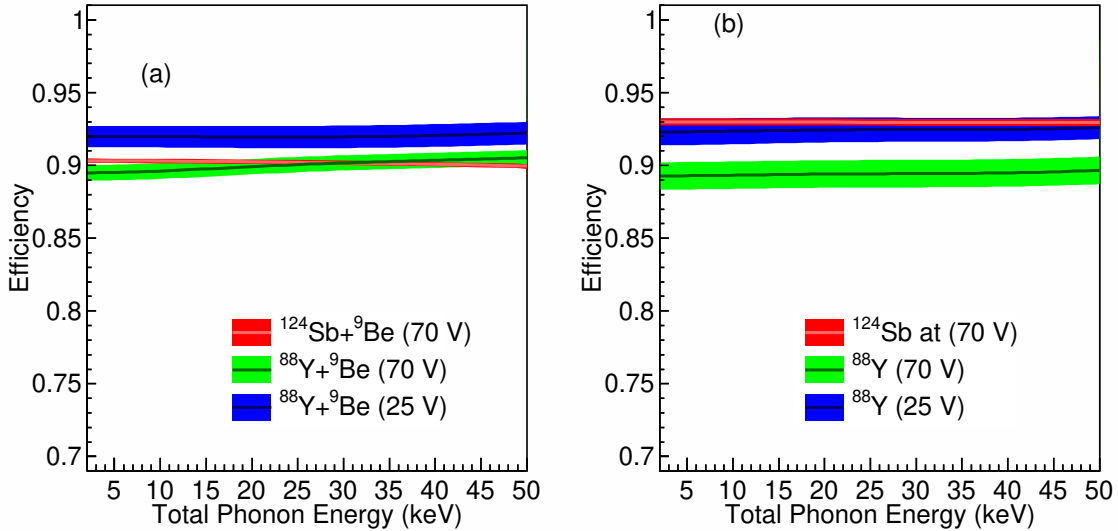
FIGURE 3.8: Cut efficiency as a function of energy for each data set. (a) With the Be wafer on, and (b) without the Be wafer [27].

The cut efficiencies were calculated on the signal events using a method developed for blinding data in the CDMSlite WIMP search analysis [33]. A package developed by SuperCDMS called the BatFaker is used to generate fake datasets. The fake data is

generated by adding randomly triggered noise events with phonon pulse templates. The BatFaker scales the amplitudes of the pulse templates such that the fake dataset becomes a good representative of the real photo-neutron data. The fake dataset can now be considered as a dataset with all good events. The cut efficiency is the ratio of the events passing all the selection cuts to the total number of events in the fake data sets. Figure 3.8 shows the cut efficiencies for the different data sets and source configurations. As seen in Fig. 3.8, the cut efficiency have an almost flat response to energy for all source configurations.

3.4 **Simulated neutron spectrum**
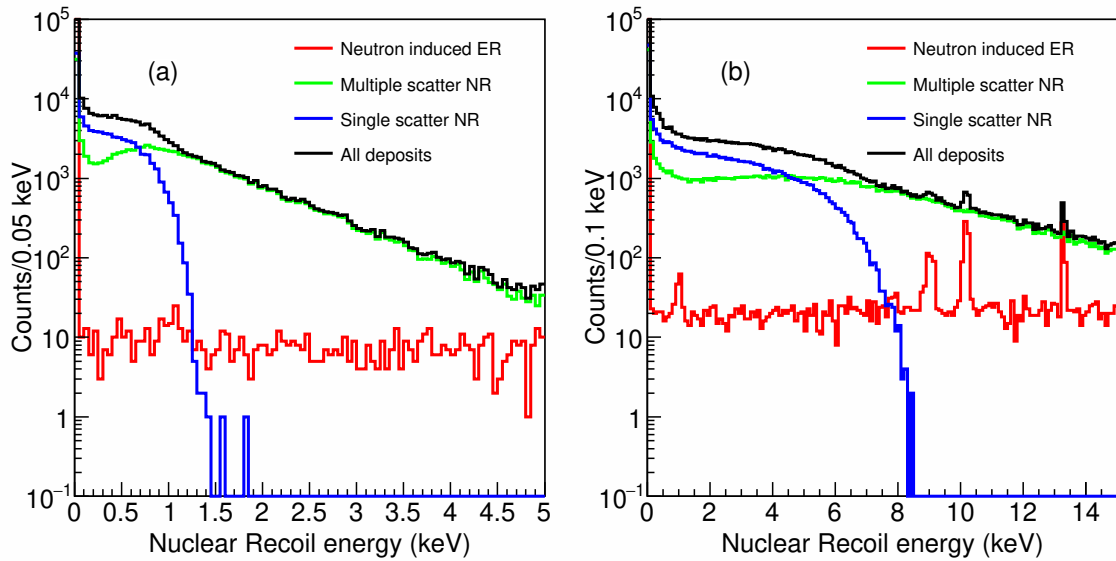
FIGURE 3.9: The simulated recoil energy distributions in (a) ^{124}Sb+^{9}Be, and (b) ^{88}Y+^{9}Be in the detector T5Z2. The energy depositions from electron recoils (ER) that come from gammas is shown in red, the energy depositions from multiple scattered neutrons in the detector is shown in green. The energy distribution of single scatter neutrons is shown in blue [27].

The ionization yield is extracted using a likelihood analysis. One of the inputs to the likelihood analysis is a neutron energy probability distribution function (PDF). SuperCDMS

has a GEANT4 10.6-based [36] package called Supersim which has detailed geometry of the experimental setup. Supersim was used to simulate the recoil energy distribution of neutrons for the different photo-neutron source configurations. The GEANT4 NeutronHP physics model [37] along with G4NDL4.6 cross-section package was used to produce the data for 1.2 billion photo-neutrons incident on the detectors. The high rate of the gamma sources made it difficult to generate the energy distribution of the gammas as they required substantial computational power and time. Therefore, only the energy depositions from the neutrons, and any secondary products like gammas due to the exposure of the materials in the experimental setup to these neutrons were simulated. The neutron-OFF data is used to model the gamma backgrounds. Figure 3.9 (a) shows the recoil energy deposition from the ^{124}Sb^{9}Be neutrons in the T5Z2 detector biased at 0 V while Fig. 3.9 (b) shows this information from the ^{88}Y^{9}Be neutron source. In Fig. 3.9 we see that the total energy deposition has two main components, (i) neutron energy deposition from nuclear recoils (NR) in Ge, and (ii) gamma energy deposition in the form of electron recoils (ER) in Ge. The NR component in the energy deposition can be further divided into single and multiple neutron scatter. The single scatter edge which corresponds to the maximum recoil energy from a single scatter neutron falls sharply at ∼ 1.3 keV for the 24 keV neutrons from ^{124}Sb^{9}Be as seen by the blue line in Fig. 3.9 (a). Similarly, the blue line in Fig. 3.9 (b) shows the single scatter edge in the neutron distribution at ∼ 8.2 keV for the 152 keV neutrons from ^{88}Y^{9}Be source. There are a large number of multiple scatters by neutrons in the detector, shown as the green line in Fig. 3.9 which bury the energy distribution from single scatter neutrons. This makes it difficult to find any feature corresponding to the single scatter edge and thereby directly determine the ionization yield from it in our data. There is an ER background which arise from the gammas that are produced as a result of the neutrons passing through the layers of lead, polyethylene, and finally reaching the Ge

detectors in their copper housing. The rate of this ER background is very low compared to the neutron scatters and is almost flat over the entire energy range as shown by the red line in Fig. 3.9. The peaks at ∼ 1 keV and ∼ 10 keV in Fig. 3.9 (b) come from the L and K shell electron capture in Ge. In Sec. 3.5.1, the NTL effect due to the bias voltage is applied to the simulated recoil energy distribution from the photo-neutrons that has been discussed here.

3.5 Yield extraction using likelihood method

The analysis makes use of the log likelihood method to extract the ionization yield in the Ge CDMSlite detectors. In this method, first a PDF describing the data is generated by combining a signal model from simulation of the neutron-ON distribution with a background model describing the electron recoil distribution of the gammas. The PDF is fit to the neutron-ON data and the best fit results are obtained when the likelihood function is minimized. The method of modeling the signal is described in Sec. 3.5.1 and the background model in 3.5.2. Section. 3.5.3 will discuss the likelihood fits that help us extract the ionization yield of the detectors. Discussions on the various uncertainties on the yield will also be done in Sec. 3.5.3.

3.5.1 Signal modeling

Section 3.4 described the procedure to simulate the recoil energy distribution (E_R) from the two photo-neutron sources when the detectors are at 0 V. When a bias voltage is applied to the detectors, the phonon energy generated through the NTL effect [38, 39] must also be taken into account. The signal is modelled for the three source configurations, (i) ^{124}Sb^{9}Be with the detector biased at 70 V, (ii) ^{88}Y^{9}Be with the detector biased at 70 V, and

(iii) ^{88}Y^{9}Be with the detector biased at 25 V. Recalling Eq 3.5 that gives the relationship between the total phonon energy measured (E_t) by the detector, the recoil energy (E_R), and energy from NTL phonons (E_{NTL}).

$$E_t = E_R \left(1 + \frac{eV_bY}{\epsilon} \right), \tag{3.9}$$

where Y is the ionization yield which is a function of recoil energy E_R, and $\epsilon = 3$ eV [40–42] is the average energy required to generate a single e^-/h^+ pair in Ge, V_b is the bias voltage, and e is unit electronic charge. The dependence of E_t on our parameter of interest Y can be seen in Eq. 3.9.

Barker and Mei [20] provide a simplified form of the Lindhard model [17] that gives the ionization yield (Y) for a material of atomic number Z. The Lindhard model can be written as,

$$Y = k\frac{g(\varepsilon)}{1 + kg(\varepsilon)}, \tag{3.10}$$

where:

$$g(\varepsilon) = 2\varepsilon^{0.15} + 0.7\varepsilon^{0.6} + \varepsilon; \quad \varepsilon = 11.5\, E_r\, Z^{-7/3}. \tag{3.11}$$

where, $g(\varepsilon)$ is a reduced energy term that arose while including the effects of the nuclear stopping power in Y. The theoretical value of k by Lindhard, which is a term related to the electronic stopping power in the material, is a constant given by $k = 0.133Z^{2/3}A^{-1/2}$ [17, 20]. For Ge this comes out to be ~ 0.157. Many experiments often adopt a value of k in the range of 0.1 and 0.2 that best describes the ionization yield as a function of recoil energy in their detectors. For example, Ref [9, 10, 13] use k=0.15, Ref [7, 8] use k=0.157, Ref [12] use k=0.159, and Ref [3, 5] use k=0.2. In the likelihood fit done in this work, k is a free parameter. A generalization of the Lindhard model given by Eq. 3.10 is considered

where the k parameter is modified as shown in Eq. 3.12, such that it varies linearly with the recoil energy.

$$k(E_r) = k_{low} + \frac{k_{\text{high}} - k_{\text{low}}}{E_{\text{high}} - E_{\text{low}}}(E_r - E_{\text{low}}), \tag{3.12}$$

where E_{low} is defined as the minimum value of the analysis threshold converted to nuclear recoil energy over all three data sets contributing to the fit. E_{high} is the maximum recoil energy of the simulated neutrons. The decision to use the 2-parameter form of k over the energy independent 1-parameter comes from a likelihood ratio test performed to determine which formalism describes the neutron-ON data better. Three thousand toy datasets for each of the three source configurations are generated sampling from the background model (described in Sec. 3.5.2) plus the neutron-ON distribution. The toy datasets are fitted twice, once using the conventional recoil energy independent single k parameter model, and once using the recoil energy dependent 2-parameter form of k (as shown in Eq. 3.12). The likelihoods obtained in the two fits were used to construct the likelihood ratio, which was used as test statistic to determine which is the best model. The likelihood ratio consists of the difference between the two log likelihood values (Δ log likelihood). The result of this study is shown in Fig. 3.10. The positive tail of the Δ log likelihood is indicative of the 2-parameter form of k always outperforms the single-parameter k model fit. The negative Δ log likelihood values are due to some of the likelihood fits not converging.

Energy resolution of the detector

The next step in modeling the signal PDF is to introduce the effects of detector resolution in the simulated neutron recoil energy distribution. The total detector resolution (σ_T) is defined as:

$$\sigma_T^2(E) = \sigma_B^2 + \sigma_F^2(E) + \sigma_D^2(E), \tag{3.13}$$
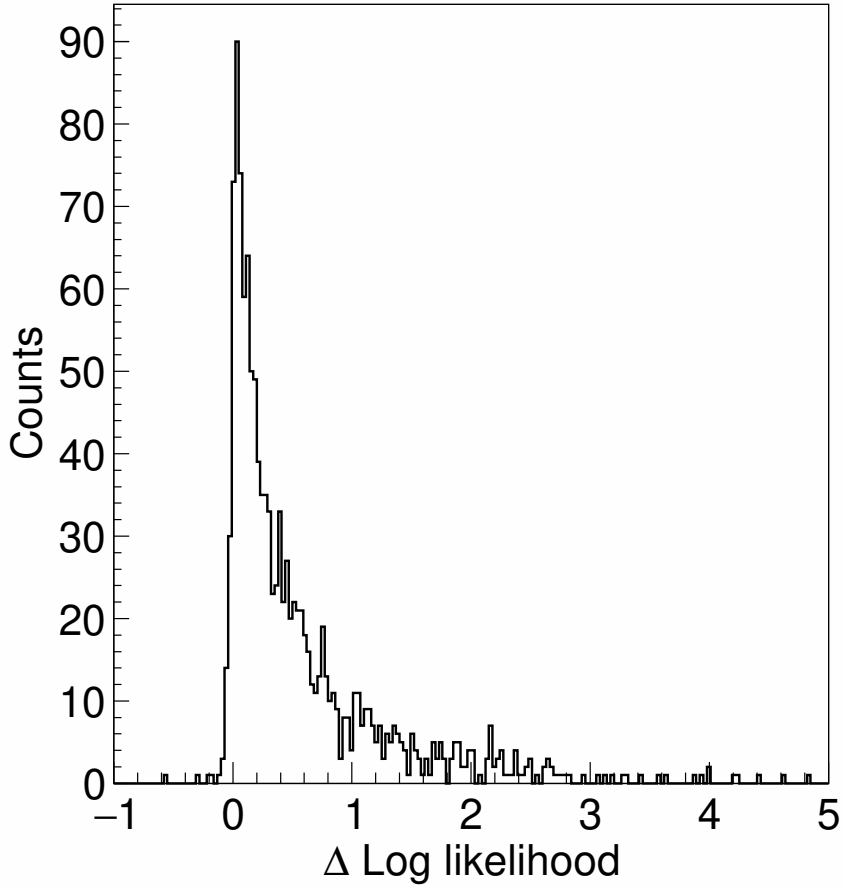
FIGURE 3.10: The Δ log likelihood distribution obtained from the 2-parameter form of k and single parameter form of k [27].

where the σ_B is the baseline noise due to the electronics. The value of σ_B is obtained by fitting a Gaussian and taking the 1σ value of the fit to the energy distribution of events randomly triggered by noise in the detector. For the 70 V datasets with T5Z2 detector, σ_B=8.31±0.08 eV and for the 25 V dataset with the T2Z1 detector σ_B=18.71±0.16 eV. The second term is the variance in the number of e^-/h^+ pairs produced in a recoil event and can be written as σ_F^2 =F$N_{e/h}\epsilon^2$=FϵE where F is the Fano factor, $N_{e/h}$ is the number of e^-/h^+ pairs produced and ϵ is the average energy to create e^-/h^+ pairs in Ge. The third term σ_D is an empirical term that has been included to model any other detector effects given by

TABLE 3.1: Values of the parameters used in the energy resolution model

Bias voltage	σ_B (eV)	F	A
70 V	8.31±0.08	0.19±0.07	0.0095±0.0015
25 V	18.71±0.16	0.27±0.02	0.0107±0.0005

AE^2. The resolution model can thus be rewritten as:

$$\sigma_T(E) = \sqrt{\sigma_B^2 + F\epsilon_\gamma E + AE^2}, \tag{3.14}$$

To determine the values of F and A in Eq. 3.14, first the resolutions of each of the K-shell, L-shell and M-shell peaks from electron-captures (EC) decays of the ^{71}Ge are determined by fitting them with a Gaussian and obtaining their 1σ values. Next the resolutions of these EC peaks are plotted as a function of energy and the resolution model described in Eq. 3.14 is fit to the data points. Figure 3.11 shows the resolution model fit to the data points obtained from K, L and M shell peaks for both the detectors. The values of F and A are determined from this fit. Table 3.1 shows the values of the different parameters used in the resolution model for the two operating voltages. Finally, to mitigate the effects due to statistical fluctuations, we smoothen the energy distributions using a Savitzky-Golay filter [43] before fitting.

3.5.2 Background modeling

There are two sources of backgrounds in the datasets. The first are γs from K, L and M shell electron captures (EC) in Ge. The ^{70}Ge in the detector are activated due to exposure to neutrons from a ^{252}Cf source that was swapped intermittently with the photo-neutron sources during the data taking period. The second source of background are from the Compton interaction of the photons coming from the photo-neutron source with the electrons of germanium. We model these backgrounds as follows:
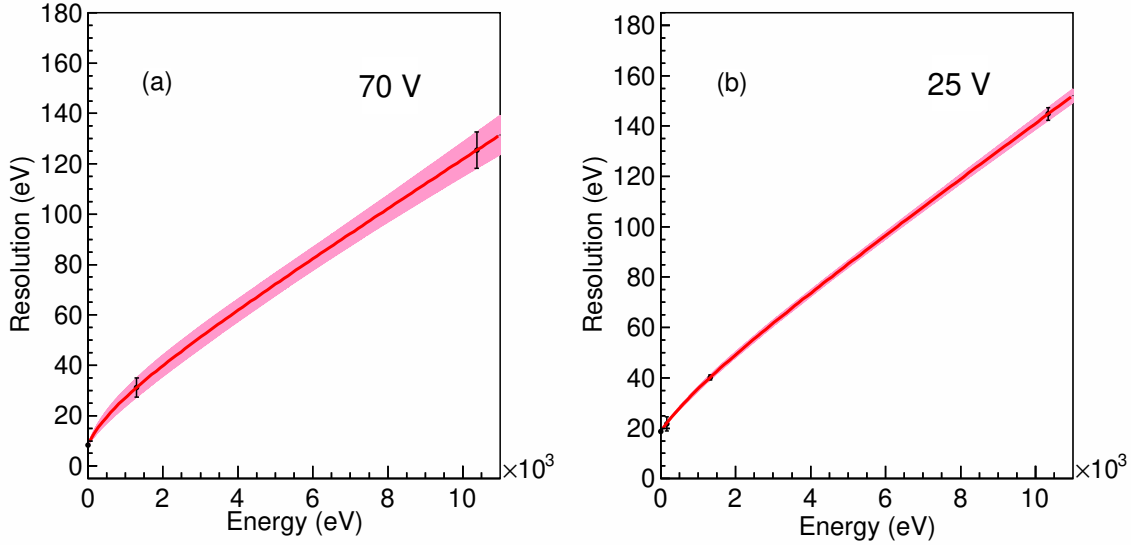
FIGURE 3.11: (a) The resolution of the T5Z2 detector operated at 70 V as a function of energy. The resolutions of the K, and L shell gammas were used as the data points for fitting of the resolution model. The M shell peak was not visible in the 70 V datasets, (b) The resolution of the T2Z1 detector operated at 25 V as a function of energy. The K, L and M shell resolutions were taken as the data points for fitting of the resolution model [27].

- The K, L and M shell EC peaks in ^{71}Ge post exposure to the ^{252}Cf source are modeled using Gaussian functions. The fractional EC probabilities (f) for each shell was determined following Ref. [44], For the K, L, and M shells, these are $f_K = 87.6\%$, $f_L = 10.5\%$, and $f_M = 1.8\%$ respectively. The only parameter determined with a fit to the neutron-off data for this background is the amplitude of the K shell peak (A_K), we then constrained the other amplitude using the fractional ratio and model the EC peak as,

$$f_{EC}(E_R) = A_K \{ \text{Gauss}(E_R, E_K, \sigma(E_K)) + \frac{f_L}{f_K} \text{Gauss}(E_R, E_L, \sigma(E_L))$$
$$+ \frac{f_M}{f_K} \text{Gauss}(E_R, E_M, \sigma(E_M)) \}, \tag{3.15}$$

where,

$$\text{Gauss}(E_R, E_{peak}, \sigma(E_{peak})) = e^{-(E_R - E_{peak})^2/(2\sigma(E_{peak})^2)}, \qquad (3.16)$$

where E_K, E_L, and E_M are the energies of each of the EC peaks with the values of 10.37 keV, 1.3 keV, and 0.16 keV respectively. The $\sigma(E_{peak})$ values are taken from the Gaussian fits made while obtaining the resolution model.

- The Compton continuum is characterized by steps corresponding to each of the Ge electron shells which arise due to the minimum energy required to free electrons from each shell. The steps are modeled by error functions, one at each step, on top of a flat background. The Compton step model is given as:

$$f_C(E) = a_0[1 + S_M \Theta(E, \mu_M)] + S_L a_0[1 + S_M \Theta(E, \mu_M)]\Theta(E, \mu_L)$$
$$+ S_K a_0\{[1 + S_M \Theta(E, \mu_M)]\Theta(E, \mu_L)\}\Theta(E, \mu_K), \qquad (3.17)$$

where S is the fractional step amplitude, and a_0 is the flat background level. The step sizes and background level are free parameters that we determined by fitting the neutron OFF data. μ is the central energy of the step, which we determined via a GEANT4 simulation. Θ is the error function:

$$\Theta(E, \mu) = \frac{1}{2}\left[1 + \text{erf}\left(\frac{E - \mu}{\sqrt{2}\sigma_T(\mu)}\right)\right], \qquad (3.18)$$

with $\sigma_T(\mu)$ as the detector resolution.

The K, L and M shell EC peaks can be observed in the data collected with the detector biased at 70 V and no external sources like the photo-neutron sources or ^{252}Cf were used. For the 25 V data the M shell step occurs below the analysis threshold, and so is excluded from the model of the two backgrounds.

The combined background model from the EC peaks and Compton steps were fit to the neutron-OFF energy distribution. The p-values of these fits were 0.001 and 0.03 for the ^{124}Sb and ^{88}Y data taken at 70 V bias, and 0.07 for the ^{88}Y data at 25 V bias. The p-values indicate a possible energy dependence in the instrumental backgrounds which cannot be analytically modeled. To include this effect we add the fit residual to the model and statistical fluctuations were smoothed by applying a Gaussian filter.

As a final step, to mimic the experimental data with more accuracy, the cut efficiencies described in Sec. 3.3 are applied to the signal PDF and the background PDF. The background model is shown in Fig. 3.12.
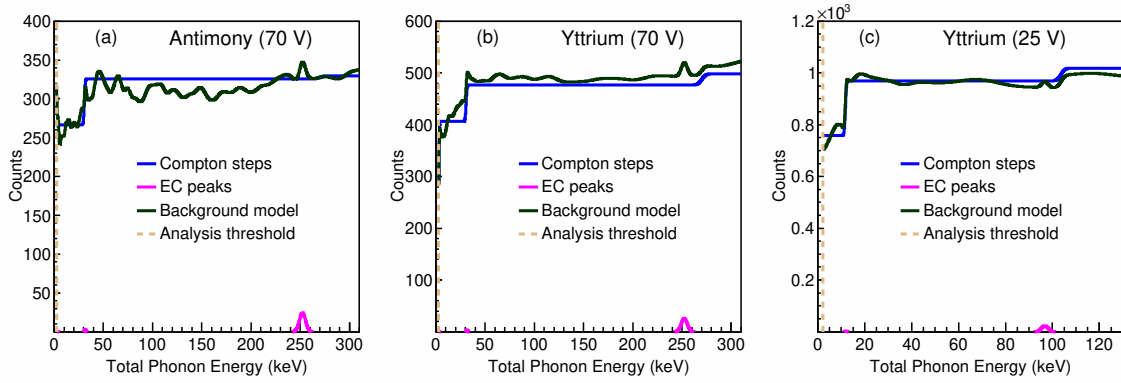
FIGURE 3.12: The different components of the background model are shown. Panel (a) is for the ^{124}Sb data at 70 V, panel (b) is for ^{88}Y data at 70 V, and panel (c) is for ^{88}Y data at 25 V. The final background model after incorporating the residuals in the fit from the Comptons and EC peaks to neutron-OFF data is shown in dark green [27].

3.5.3 Likelihood analysis

The summed negative log likelihood function $-\ln \mathcal{L}$ is defined in Eq. 3.19.

$$-\ln \mathcal{L} = -\sum_{D=1}^{3} \sum_{i=1}^{N_D} \ln(f_D \nu_D(E_i, k) + (1 - f_D) b_D(E_i)), \qquad (3.19)$$

where N_D is the number of events in a data set D. There are three neutron-ON datasets in this analysis, i.e. (i) ^{124}Sb^{9}Be data with the detector biased at 70 V, (ii) ^{88}Y^{9}Be data with

the detector biased at 70 V, and (iii) ^{88}Y^{9}Be data with the detector biased at 25 V. f_D is the fractional contribution of the neutron PDF $\nu_D(E)$ to the total energy spectrum of the data set. The method of obtaining $\nu_D(E)$ was discussed in Sec. 3.5.1. $b_D(E)$ is the background PDF as described in Sec. 3.5.2. The negative log likelihood function is minimized using the MINUIT [45] minimization package. The free parameters of this function are the three neutron contribution fractions f_D for each of the neutron-ON data set, and the Lindhard parameters k$_{low}$ and k$_{high}$. Figure 3.13 shows the total phonon energy spectrum with the best fit result of the modified two k-parameter Lindhard model overlaid for the three data sets.
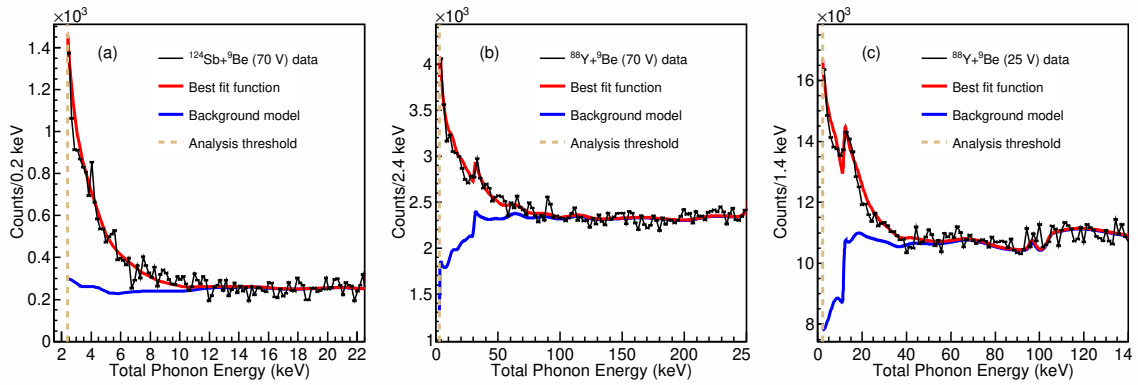
FIGURE 3.13: Energy spectrum for the three data sets, (a) ^{124}Sb+^{9}Be with T5Z2 biased at 70 V, (b) ^{88}Y+^{9}Be with T5Z2 biased 70 V and (c) ^{88}Y+^{9}Be with T2Z1 biased at 25 V, with best fit result overlaid, shaded area shows the fit uncertainty. Blue curve shows the fitted gamma background contribution [27].

Uncertainties calculation

The uncertainties can be divided into 2 categories, statistical and systematic. The following statistical uncertainties in the ionization yield are considered: (i) randomness associated with the application of the detector energy resolution model in the simulated neutron spectrum, (ii) uncertainties in the experimental neutron-ON distribution, and (iii) the cut

efficiency. The randomness associated with the application of the detector energy resolution model to the neutron PDF can affect the exact shape of the neutron PDF. The resulting statistical uncertainty in the ionization yield is estimated by performing the likelihood fit 184 times, each time with a different random seed associated with the application of energy resolution. The resulting distributions of k_{low} and k_{high} are fitted with a Gaussian and its one sigma deviation is taken as the uncertainty. To evaluate the statistical uncertainty arising from the experimental statistics in the neutron-ON spectrum, 230 data sets of mock Monte Carlo (MC) neutron-on data sets are produced. The total number of events is the same as that for the experimental data. The number of events selected from each data set D is equal to $f_D N_D$ while the background component is comprised of $(1\text{-}f_D)N_D$ events. The likelihood fits are repeated in each of the 230 data sets. The distributions of the fit results (k_{low} and k_{high}) are fitted with Gaussian distributions. We take the one standard deviation of the Gaussian as the uncertainty for each of the contributions. We propagated the uncertainty on the cut efficiency by repeating the analysis twice, using the efficiencies shifted by one standard deviation up and down with respect to their central values. We take the difference in the fit results as an estimate for the uncertainty in the yield.

We evaluated four sources of systematic uncertainties in the ionization yield: (i) The uncertainty in the neutron-nucleus cross section, (ii) the choice of physics model in GEANT4 simulations, (iii) the value of the Fano factor, and (iv) the shape of the background model. The GEANT4 neutron simulation as described in Sec. 3.4 was repeated with several different randomly chosen cross section files for each Ge isotope from the TENDL-2017 [46] library. The negative log likelihood fit was repeated for each of the simulations, and the standard deviation of the resulting distribution of fit results (k_{low} and k_{high}) is used to estimate the systematic uncertainty due to the elastic scattering cross section. In order to quantify the systematic uncertainty due to the choice of the physics model in this analysis

i.e. NeutronHP [37], another simulation was performed using the LEND physics model [47]. In the LEND models the cross sections are evaluated at a fixed temperature, rather than the on-demand temperature calculations of NeutronHP [36]. The difference between the k_{low} and k_{high} fit results obtained using these two models is used as a systematic source of uncertainty. There is also a study [48] that showed the Fano factor (F) for nuclear recoils could be significantly higher than that for electron recoils i.e. ~ 6.1. To account for these uncertainties in the ionization yield, the fit is repeated twice. The upper limit of the uncertainty comes from using (F-δF) as the value of the fano factor, where δF is the statistical uncertainty showin in Table 3.1. The lower limit of the uncertainty comes from using a value of ($10+\delta F$) to account for nuclear recoils. The value of 10 is chosen as conservatively to be above the value quoted in ref. [48]. The resulting difference in the fit results is taken to be the systematic uncertainty associated with the Fano factor. In order to evaluate the uncertainty on the shape of the background model described in Sec. 3.5.2, we recalculate the yield directly using the neutron-off data energy distributions as background model, first smoothed with a Gaussian filter to mitigate for the statistical fluctuations and then fitted with a cubic spline. The difference in the k_{low} and k_{high} result with respect to the results obtained using the standard background model described in Sec. 3.5.2 is used as an estimate for this systematic uncertainty. All the statistical uncertainties are added in quadrature to get the total statistical uncertainty. Likewise all the systematic uncertainties are added in quadrature to get the total systematic uncertainty. The overall uncertainty on the ionization yield is obtained by adding the total systematic and total statistical uncertainties.

TABLE 3.2: Summary of the uncertainties on the k parameters of the Lindhard model

	Best fit value	Stat. uncertainty	Sys. uncertainty
k_{low}	0.040	0.005	0.008
k_{high}	0.142	0.011	0.018

3.6 Results and summary

3.6.1 Results

Table 3.2 gives the best fit values of k_{low} and k_{high} along with the statistical and systematic uncertainties associated with them. These k parameters and their respective uncertainties are propagated to the ionization yield $Y(E_{r,nr})$ and plotted as a function of the nuclear recoil energy in Fig. 3.14. The resulting ionization yield in the Ge CDMSlite detector approaches the yield predicted by the Lindhard model with the standard $k = 0.157$ value at ~ 7 keV. The data indicates a lower ionization yield in the recoil energy range explored in this analysis compared to the yield from classic Lindhard model. As seen from Fig. 3.14, the dominant sources of uncertainty for this measurement are from the statistical uncertainty of the experimental data and the systematic uncertainty due to the neutron-nucleus elastic cross section in Ge.

3.6.2 Summary

A better understanding of the ionization yield will reduce the uncertainty in the measured nuclear recoil energy from a DM-nucleus scattering process. Measurements of ionization yields from low energy nuclear recoils is of importance to low mass direct dark matter search experiments as they establish a more accurate sensitivity of a DM detector. In this analysis, we report the measurement of nuclear recoil induced ionization yield in Ge
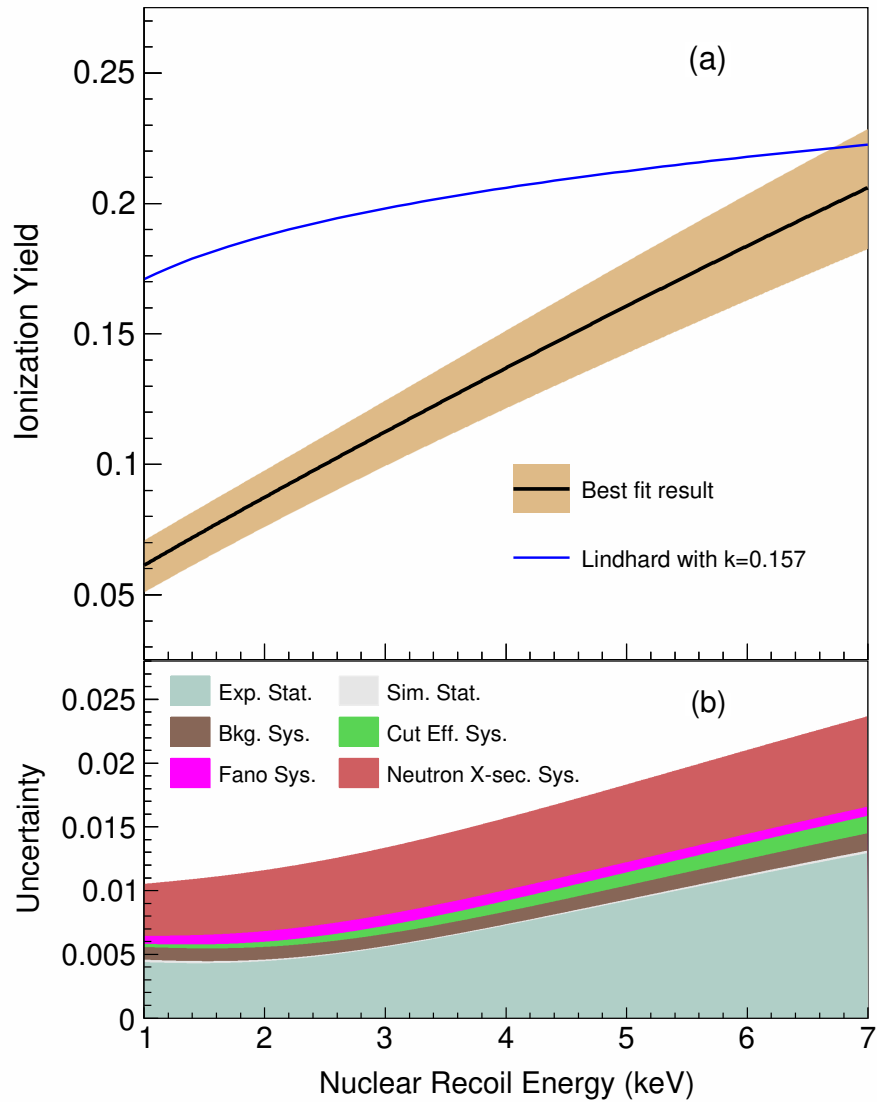
FIGURE 3.14: (a) The ionization yield from the best fit values of the 2 k-parameter Lindhard model
as a function of the nuclear recoil energy in germanium. Blue line shows the classic
Lindhard model with $k = 0.157$ (b) The contribution of various sources of statistical
and systematic uncertainties to the ionizzation yield in germanium [27].

between 1 keV and 7 keV recoil energy operated at $\sim$ 50 mK. The ionization yield is
extracted using a likelihood analysis that makes use of GEANT4 based simulations to
generate a neutron PDF and a data-driven approach to model the background PDF. The

yield model considered in this work is a modified Lindhard model with the *k* parameter considered as a linear combination of two components k_{low} and k_{high} with a dependence on recoil energy as given in Eq. 3.12. The likelihood ratio test described in Sec. 3.5.1 validates that the data prefers some energy-dependence in k and justifies the use the energy dependent two k-parameter formalism. The results from this study showed deviations from the ionization yield predicted by the classic Lindhard model with k=0.157. The likelihood analysis return a best fit values of $k_{low} = 0.040 \pm 0.013$ and $k_{high} = 0.142 \pm 0.029$. The measurement from this study is compatible with previous ionization yield measurements taken with CDMS-II Ge detectors [8].

Bibliography

[1] R. Agnese et al. "Search for Low-Mass Dark Matter with CDMSlite Using a Profile Likelihood Fit". *Phys. Rev.* D99.6 (2019), p. 062001. arXiv: `1808.09098 [astro-ph.CO]`.

[2] R. Agnese et al. "Projected sensitivity of the SuperCDMS SNOLAB experiment". *Phys. Rev. D* 95 (8 Apr. 2017), p. 082002.

[3] K. W. Jones and H. W. Kraner. "Stopping of 1- to 1.8-keV ^{73}Ge Atoms in Germanium". *Phys. Rev. C* 4 (1 July 1971), pp. 125–129.

[4] K. W. Jones and H. W. Kraner. "Energy lost to ionization by 254-eV ^{73}Ge atoms stopping in Ge". *Phys. Rev. A* 11 (4 Apr. 1975), pp. 1347–1353.

[5] C. E. Aalseth et al. "CoGeNT: A Search for Low-Mass Dark Matter using p-type Point Contact Germanium Detectors". *Phys. Rev.* D88 (2013), p. 012002. arXiv: `1208.5737 [astro-ph.CO]`.

[6] Ruan Xi-chao et al. "Nuclear recoil quenching factor, measurement for HPGe detector". *Nuclear recoil quenching factor measurement for HPGe detector, presented at Application of Germanium Detector in fundamental research, Tsinghua University* (Mar. 2011), 24–26.

[7]   Y. Messous et al. "Calibration of a Ge crystal with nuclear recoils for the development of a dark matter detector". *Astroparticle Physics* 3.4 (1995), pp. 361 –366. ISSN: 0927-6505.

[8]   Z. Ahmed et al. "Results from a Low-Energy Analysis of the CDMS II Germanium Data". *Phys. Rev. Lett.* 106 (13 Mar. 2011), p. 131302.

[9]   C. Chasman et al. "Band-Gap Effects in the Stopping of Ge^{72*} Atoms in Germanium". *Phys. Rev. Lett.* 21 (20 Nov. 1968), pp. 1430–1433.

[10]   T. Shutt et al. "Measurement of ionization and phonon production by nuclear recoils in a 60 g crystal of germanium at 25 mK". *Phys. Rev. Lett.* 69 (24 Dec. 1992), pp. 3425–3427.

[11]   E. Armengaud et al. "Performance of the EDELWEISS-III experiment for direct dark matter searches". *Journal of Instrumentation* 12.08 (Aug. 2017), P08010–P08010.

[12]   Sattler et al. "Ionization Produced by Energetic Germanium Atoms within a Germanium Lattice". *Phys. Rev.* 143 (2 Mar. 1966), pp. 588–594.

[13]   "High-purity germanium detector ionization pulse shapes of nuclear recoils, gamma-interactions and microphonism". *Nuclear Instruments and Methods in Physics Research Section A: Accelerators, Spectrometers, Detectors and Associated Equipment* 418.2 (1998), pp. 348 –354. ISSN: 0168-9002.

[14]   E. Simon et al. "SICANE: a detector array for the measurement of nuclear recoil quenching factors using a monoenergetic neutron beam". *Nuclear Instruments and Methods in Physics Research Section A: Accelerators, Spectrometers, Detectors and Associated Equipment* 507.3 (2003), pp. 643 –656. ISSN: 0168-9002.

[15]   B. J. Scholz et al. "Measurement of the low-energy quenching factor in germanium using an ^{88}Y/Be photoneutron source". *Phys. Rev.* D94.12 (2016), p. 122003. arXiv: 1608.03588 [physics.ins-det].

[16]   J. Lindhard and M. Scharff. "Energy Dissipation by Ions in the kev Region". *Phys. Rev.* 124 (1 Oct. 1961), pp. 128–130.

[17]   J. Lindhard et al. "RANGE CONCEPTS AND HEAVY ION RANGES (NOTES ON ATOMIC COLLISIONS, II)". *Kgl. Danske Videnskab. Selskab. Mat. Fys. Medd.* 33.14 (Jan. 1963).

[18] Lindhard et al. "INTEGRAL EQUATIONS GOVERNING RADIATION EFFECTS. (NOTES ON ATOMIC COLLISIONS, III)". *Kgl. Danske Videnskab., Selskab. Mat. Fys. Medd.* 33.10 (Jan. 1963).

[19] J. Lindhard, V. Nielsen, and M. Scharff. *Approximation Method in Classical Scattering by Screened Coulomb Fields: Notes on Atomic Collisions, 1*. Matematisk-fysiske meddelelser. Munksgaard, 1968.

[20] D. Barker and D.-M. Mei. "Germanium detector response to nuclear recoils in searching for dark matter". *Astroparticle Physics* 38 (2012), pp. 1 –6. ISSN: 0927-6505.

[21] Glenn F. Knoll. *Radiation Detection and Measurement, 3rd ed.* 3rd edition. New York: John Wiley and Sons, 2000. ISBN: 978-0-471-07338-3, 978-0-471-07338-3.

[22] W.-Z. Wei and D.-M. Mei. "Average energy expended per e-h pair for germanium-based dark matter experiments". *Journal of Instrumentation* 12.04 (Apr. 2017), P04022–P04022.

[23] A. Benoit et al. "Measurement of the response of heat-and-ionization germanium detectors to nuclear recoils". *Nuclear Instruments and Methods in Physics Research Section A: Accelerators, Spectrometers, Detectors and Associated Equipment* 577.3 (2007), pp. 558 –568. ISSN: 0168-9002.

[24] R. Agnese et al. "Projected sensitivity of the SuperCDMS SNOLAB experiment". *Phys. Rev. D* 95 (8 Apr. 2017), p. 082002.

[25] R. C. Mobley and R. A. Laubenstein. "Photo-Neutron Thresholds of Beryllium and Deuterium". *Phys. Rev.* 80 (3 Nov. 1950), pp. 309–314.

[26] A. Wattenberg. "Photo-Neutron Sources and the Energy of the Photo-Neutrons". *Phys. Rev.* 71 (8 Apr. 1947), pp. 497–507.

[27] SuperCDMS. *SuperCDMS public documentation page.* https://www.slac.stanford.edu/exp/cdms/pubdocs_pending_approval/photoneutron_CDMSlite/v3/PublicDocumentation_PNv3.html.

[28] Berkeley. *Super Cryogenic Dark Matter Search.* http://cdms.berkeley.edu/gallery.html.

[29]   Berkeley. *Super Cryogenic Dark Matter Search*. http://cdms.berkeley.edu/experiment.html.

[30]   R. Agnese et al. "Demonstration of Surface Electron Rejection with Interleaved Germanium Detectors for Dark Matter Searches". *Appl. Phys. Lett.* 103 (2013), p. 164105. arXiv: 1305.2405 [physics.ins-det].

[31]   R. Agnese et al. "Search for Low-Mass Weakly Interacting Massive Particles Using Voltage-Assisted Calorimetric Ionization Detection in the SuperCDMS Experiment". *Phys. Rev. Lett.* 112 (4 Jan. 2014), p. 041302.

[32]   Sunil Ramanlal Golwala. "Exclusion limits on the WIMP nucleon elastic scattering cross-section from the Cryogenic Dark Matter Search". PhD thesis. Jan. 2000.

[33]   R. Agnese et al. "Low-mass dark matter search with CDMSlite". *Phys. Rev. D* 97 (2 Jan. 2018), p. 022002.

[34]   W. Hampel and L. P. Remsberg. "Half-life of ^{71}Ge". *Phys. Rev. C* 31 (2 Feb. 1985), pp. 666–667.

[35]   J. A. BEARDEN and A. F. BURR. "Reevaluation of X-Ray Atomic Energy Levels". *Rev. Mod. Phys.* 39 (1 Jan. 1967), pp. 125–142.

[36]   J. Allison et al. "Recent developments in Geant4". *Nuclear Instruments and Methods in Physics Research Section A: Accelerators, Spectrometers, Detectors and Associated Equipment* 835 (2016), pp. 186 –225. ISSN: 0168-9002.

[37]   T. Koi. "NeutronHP, Hadronic Framework". In: *18th GEANT4 collaboration meeting*. 2013.

[38]   P.N. Luke et al. "Calorimetric ionization detector". *Nucl. Instrum. Meth. A* 289 (1990), pp. 406–409.

[39]   B.S. Neganov et al. "Application of ionization to heat conversion to the light absorption spectra measurement in silicon at 1 K through adiabatic calorimetry". *J Low Temp Phys* 93 (1993), pp. 417–422.

[40]   S.O.W. Antman and all. "Measurements of the Fano factor and the energy per hole-electron pair in germanium". *Nuclear Instruments and Methods* 40.2 (1966), pp. 272 –276. ISSN: 0029-554X.

[41] R.H. Pehl et al. "Accurate determination of the ionization energy in semiconductor detectors". *Nuclear Instruments and Methods* 59.1 (1968), pp. 45 –55. ISSN: 0029-554X.

[42] F. E. Emery and T. A. Rabson. "Average Energy Expended Per Ionized Electron-Hole Pair in Silicon and Germanium as a Function of Temperature". *Phys. Rev.* 140 (6A Dec. 1965), A2089–A2093.

[43] Abraham. Savitzky and M. J. E. Golay. "Smoothing and Differentiation of Data by Simplified Least Squares Procedures." *Analytical Chemistry* 36.8 (1964), pp. 1627–1639. eprint: https://doi.org/10.1021/ac60214a047.

[44] E. Schönfeld. "Calculation of fractional electron capture probabilities". *Applied Radiation and Isotopes* 49.9 (1998), pp. 1353 –1357. ISSN: 0969-8043.

[45] F. James and M. Roos. "Minuit - a system for function minimization and analysis of the parameter errors and correlations". *Computer Physics Communications* 10.6 (1975), pp. 343 –367. ISSN: 0010-4655.

[46] A.J. Koning and D. Rochman. "Modern Nuclear Data Evaluation with the TALYS Code System". *Nuclear Data Sheets* 113.12 (2012). Special Issue on Nuclear Reaction Data, pp. 2841 –2934. ISSN: 0090-3752.

[47] GEANT4. *Low Energy Nuclear Data Package*.

[48] Brian L. Dougherty. "Measurements of ionization produced in silicon crystals by low-energy silicon atoms". *Phys. Rev. A* 45 (3 Feb. 1992), pp. 2104–2107.

Chapter 4

Backgrounds in low mass dark matter search experiments

When a particle interacts with a detector, it deposits some energy, creating an event. In direct dark matter search experiments, there are two quantities one can obtain, (i) recoil energy from an interaction, and (iii) event rate of particle interactions. The events of interest are from dark matter (DM) particles elastically scattering of the nuclei in the detector. These are called as signal events. Events arising from any other source like gammas or neutrons are undesired, and are called background events. The observed event rate comprises of both signal and background events. The DM-nucleon interaction cross sections are very low. For DM with a mass above 1 GeV, most experiments have ruled out the possibility of finding a DM with a nucleon interaction cross section higher than 10^{-40} cm^2 [1]. This makes finding DM a rare event search. Moreover, for low mass dark matter (LMDM), the nuclear recoil energy signals are weak (i.e. < 1 keV) [2]. Hence it is a challenge to

distinguish these rare and weak signals from backgrounds in a LMDM search experiment. A good understanding of the background sources is needed to either reject or reduce the background counts in an experiment. In this chapter, the sources of backgrounds in the SuperCDMS SNOLAB DM search experiment are discussed in Sec. 4.1, followed by the results on the measurements of some comsogenically activated backgrounds in Sec. 4.2, and finally the summary and conclusion of this chapter is given in Sec. 4.3.

4.1 Backgrounds in SuperCDMS SNOLAB

The SuperCDMS SNOLAB is a direct DM search experiment situated in Sudbury, Ontario, Canada [3]. SuperCDMS SNOLAB will look for LMDM using germanium (Ge) and silicon (Si) detectors. The detectors of each material will be of two types, high voltage (HV), and iZIP [3]. The experiment site is $\sim$ 2100 m underground. The layers of rock between the Earth's surface and the experiment site provides natural shielding from the high energy cosmic rays coming through the Earth's atmosphere. An overview of the various sources of backgrounds for the experiment will be discussed in Sec. 4.1.1. The effect of two major background sources, ^{3}H and ^{32}Si on the projected sensitivity curve by SuperCDMS SNOLAB is discussed in Sec. 4.1.2. The section will conclude with a discussion in Sec, 4.1.3 on the need to have dedicated measurements of the backgrounds in the experiment.

4.1.1 Sources of backgrounds

The expected backgrounds can be broadly divided into three categories, (i) Detector contamination, (ii) Compton scatter from gamma rays, and (iii) Cosmogenic and radiogenic neutrons. A brief description of each of the aforementioned categories is given below.

1. Detector Contamination

Radioactive impurities arising from within the detector material is termed as detector contamination. Some of the dominant backgrounds expected in the SuperCDMS SNOLAB detectors are from inherent impurities. The main contaminants are discussed below.

Tritium: For the duration between extraction, fabrication and transport to a clean room facility, detectors can be exposed to high energy cosmic ray secondaries like protons, neutrons and muons. The transfer of energy from these cosmic ray secondaries to the nucleus of the detector material can lead to neutrons, protons or a cluster of nucleons to escape from the nucleus [4]. One such nuclear cluster that is known to be ejected from the nucleus of the detector material is tritium (^{3}H). Tritium is known to beta-decay with an endpoint energy of 18.6 keV. It has a half life of 12.3 years [5]. For LMDM searches, the electron recoils (ER) created from these low energy beta particles could bury a signal from LMDM. The HV detectors which are developed for LMDM searches cannot discriminate between electron recoils from ^{3}H and nuclear recoils from LMDM. Tritium beta-decay background is expected in both Ge and Si detectors.

^{32}**Si:** The radioactive ^{32}Si isotope is produced when cosmic ray secondaries break up ^{40}Ar in the Earth's atmosphere [6]. It then makes its way to terrestrial environment through precipitation and accumulates with other Si deposits from where they are mined. The ^{32}Si isotopes settle in to the Si detectors at the time of fabrication and will beta-decay with an endpoint energy of 227 keV. It has a half life of 153 years [7]. For Si HV detectors, the ERs from ^{32}Si is a source of background for the DM searches.

Ge activation lines: The interaction of cosmic ray secondaries with the nucleus of the detector material can induce an electron capture (EC) process. Photons are released depending on the shell from which the electron is captured. Germanium has five naturally

occurring isotopes i.e. ^{70}Ge, ^{72}Ge, ^{73}Ge, ^{74}Ge. and ^{76}Ge [8]. The Ge detector contains 'natural Ge' or 'nat. Ge', which is a mixture of all these isotopes. Natural Ge also contain several isotopes with atomic number (A) less than 76 due to spallation by cosmic rays. Several EC processes occurring due to interaction of cosmic ray secondaries with nat Ge have been observed and they have half lives varying from a few seconds to several years [9]. A few of the long lived isotopes in nat Ge are ^{68}Ge, ^{65}Zn, ^{73}As, ^{57}Co, ^{55}Fe, ^{54}Mn and ^{49}V [10]. For Ge HV detectors, the photons from EC processes in these isotopes are a source of ER backgrounds.

2. Compton scatter from gamma rays

The surrounding environment at the experiment site will contain commonly existing radioactive impurities like ^{238}U and ^{232}Th and their daughter products and ^{40}K. These impurities will also be present in materials that make up the detector hardware, cryostats, and other parts of the experimental setup. These impurities produce gammas that undergo Compton scatterring in the detector [3]. The energy deposited in the detector due to these Compton scatters are a source of background in DM searches.

3. Cosmogenic and radiogenic neutrons

Cosmic ray secondaries can produce neutrons from the cavern wall at the experiment site. Cosmic ray induced neutrons can also be emitted from the shielding materials during various experimental operations. Neutrons in the cavern environment can also be produced from isotopes in the U and Th decay chains. These neutrons can create NRs in the detector that can mimic DM signals.

Figure 4.1 shows a comparison among the different sources of backgrounds expected at SuperCDMS SNOLAB [3]. The event rate in units of events/(kg·yr·keV) or differential
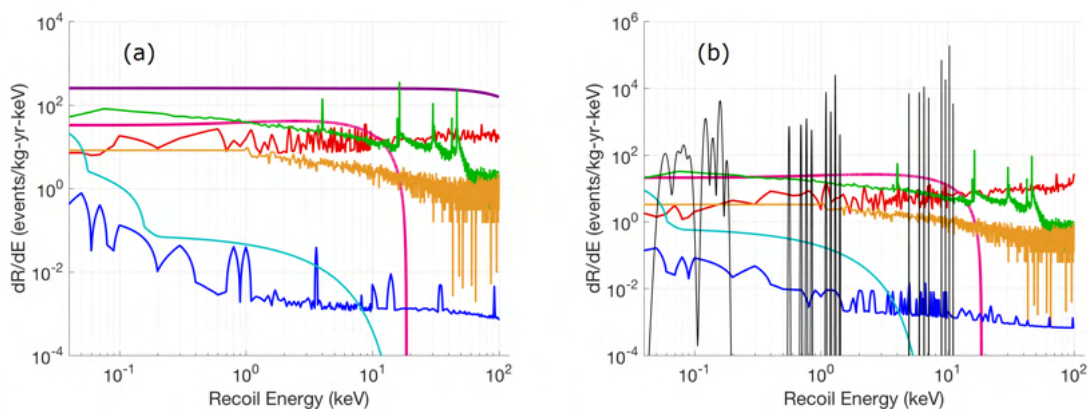
FIGURE 4.1: The background rate of each source in units of events/(kg·yr·keV) (or DRU) is shown as a function of recoil energy. Panel (a) is for a Si HV detector and panel (b) is for a Ge HV detector. The ^{32}Si is shown in purple, ^{3}H in pink, Compton scatters from gammas are shown in red, surface betas are shown in green, surface alphas are shown in orange, neutrons are shown in blue, and CEνNS background is shown in cyan. The black lines correspond to activation lines in Ge due to electron capture process [3].

rate units (DRU) for each background source is shown as a function of recoil energy. From Fig. 4.1 (a), we see that the maximum contribution in backgrounds for a Si HV detector at low recoil energies (< 10 keV) come from ^{32}Si and ^{3}H. There is also considerable background being produced by surface alphas and betas which arise primarily from daughters of ^{222}Rn in the air within the experimental setup. The decay products of ^{222}Rn, like ^{210}Pb get implanted only on the surface and the events caused by them can be rejected during data analysis by defining a fiducial volume of the detector. The next biggest contribution comes from Compton scatters by gamma rays. At very low recoil energies, we see the event rate of neutron background increases. If the detector becomes sensitive enough to neutrinos, then the coherent elastic neutrino nucleus scattering (CEνNS) will also be a background for the experiment [11]. We see a similar trend of background contribution from various components in Fig. 4.1 (b) in a Ge HV detector. The exception being the absence of the ^{32}Si background. The activation lines in nat. Ge can also be seen as a major source of

background in Ge detectors.

4.1.2   Effect of backgrounds on low mass dark matter search
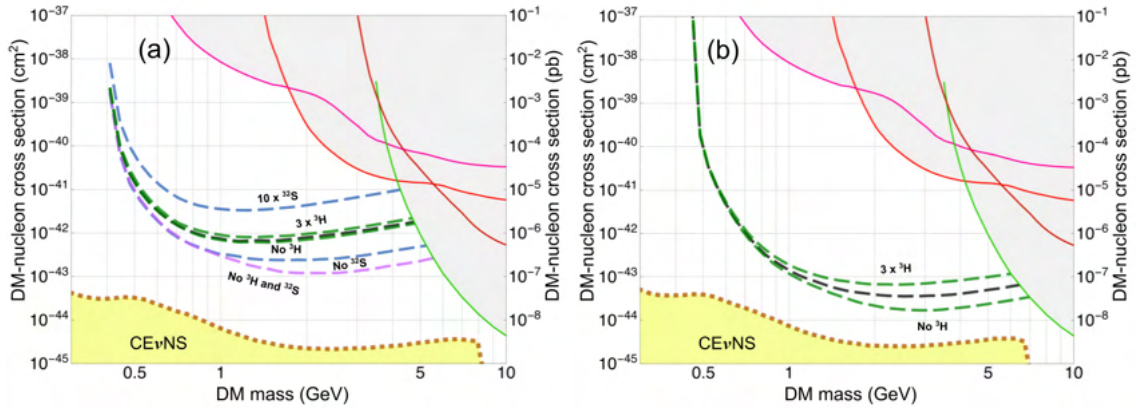
FIGURE 4.2: The projected sensitivity curves of the SuperCDMS SNOLAB experiment in the DM-
nucleon cross section vs DM mass parameter space. (a) The sensitivity expected using
nominal values of ^{32}Si and ^{3}H in Si from literature is shown in black dashed line. The
blue dashed lines correspond to the sensitivity by varying the level of ^{32}Si in Si HV,
from ten times its nominal value to zero. Likewise the green dashed lines correspond
to sensitivity by varying level of ^{3}H in Si from three times its nominal value to zero.
(b) The projected sensitivity of the SuperCDMS SNOLAB experiment in nat Ge HV
detector and the effect of varying the ^{3}H background on it from three times its nominal
value to zero. The solid lines in both the panels represent existing exclusion limits by
various experiments [3].

From Sec. 4.1.1 it can be seen that the two most dominant background sources in

the Si HV and Ge HV detectors are ^{32}Si and ^{3}H respectively. In Fig. 4.2, the effect of

varying the ^{32}Si and ^{3}H backgrounds on the projected SuperCDMS SNOLAB sensitivity

with the Si and Ge detectors are shown. The black dashed line in Fig. 4.2 (a) correspond

to the expected sensitivity of the Si HV detector at SNOLAB [3] in the DM-nucleon cross

section vs the DM mass parameter space. This was computed assuming the available

production rates in literature for ^{32}Si and ^{3}H in Si. The blue dashed curve above the

expected sensitivity projection represents the sensitivity curve if we assume the production

of ^{32}Si to be ten times its nominal value in literature [12]. The blue dashed curve below the expected sensitivity projection represents the sensitivity of the Si detector if there was no ^{32}Si background. Likewise the green dashed lines show the effect of varying ^{3}H levels in Si detectors from three times its nominal value (represented by the upper green curve) to no ^{3}H in Si (represented by the lower green curve). The purple dashed line shows the projected sensitivity assuming neither ^{32}Si nor ^{3}H background in Si. Figure 4.2 (b) likewise shows the effect of varying the ^{3}H production rates in nat Ge from three times its nominal value to zero. It can be seen from Fig. 4.2 that having a precise understanding of the background rate in the experiment has a direct impact on its sensitivity to DM search.

4.1.3 Need for dedicated background measurements

The effect of varying the highest background contributors in Si and Ge is shown in Fig. 4.2. For ^{3}H production rates in Ge, only one experimental measurement exits till date, which is by EDELWEISS reporting a rate of 82±21 atoms/(kg·day) [13]. All other literature work on ^{3}H production rates come from theoretical calculations that depend on the nuclear models used. In Ge, they vary from a production rate as low as ~23 atoms/(kg·day) in Ref. [14] to a rate as high as 178 atoms/(kg·day) in Ref. [15]. Similarly, the only experimentally measured rate of ^{32}Si in Si come from DAMIC which reports a value of 80^{+110}_{-65} decays/(kg·day) [12]. This measurement has a large spread in its uncertainty. However, another measurement by the same experiment gives a much lower concentration of ^{32}Si in Si at 11 ± 2.4 decays/(kg·day) [16]. The concentration of ^{32}Si can vary depending upon the ore from which the Si was extracted. The lack of sufficient experimental measurements, and varying levels of contamination reported by the existing measurements motivate a precise understanding of the dominant backgrounds arising from the inherent impurities in the detector material. In the next section, a measurement of ^{3}H production in Ge along

with a few other cosmogenically produced contaminants is discussed using the CDMS low ionization threshold experiment (CDMSlite).

4.2 Measurement of detector contamination from CDMSlite

SuperCDMS has made a measurement of the ^{3}H production level and a few other cosmogenically activated contaminants. The measurement was done in Ge using the CDMS low ionization threshold experiment (CDMSlite) dark matter search data taken at Soudan mines, Minnesota, USA [17]. The analysis makes use of a likelihood method to extract the production rate of the contaminants in germanium. A summary of the analysis is given in the following subsections.

4.2.1 Analysis flowchart
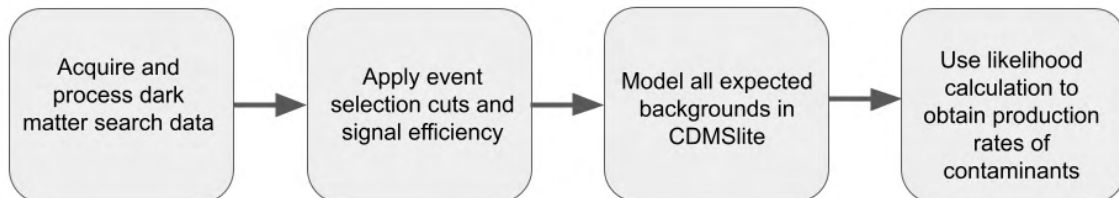
FIGURE 4.3: A flowchart of the analysis to extract production rate of cosmogenically activated contaminants in the CDMSlite Ge detectors.

Figure 4.3 gives a flowchart of the analysis to extract the ^{3}H production rate in Ge. The DM search data is vetted by applying several event selection cuts to remove undesired events. Then the overall signal efficiency which comprises of the trigger and analysis cut efficiencies are calculated as a function of energy. A probability distribution function (PDF) is modelled for all expected backgrounds in the CDMSlite data. These include the

cosmogenically activated detector contaminants. Using a negative log likelihood function, the number of events from each background source contributing to the total background energy distribution is obtained. The number of events by each background is then converted to units of atoms/(kg·day) and the production rate of contaminants at the start of the CDMSlite run is derived.

4.2.2 Experiment and Datasets

The SuperCDMS Soudan detectors and experimental setup is the same as that shown in Fig. 3.4 and Fig. 3.3 in Chapter 3. The only difference being the layers of lead above the icebox and the photo-neutron source holder shown in Fig. 3.3 (a) that were included exclusively for the photo-neutron runs, are not part of this DM search setup. The setup had five towers of Ge detectors. Each tower comprised of 3 detectors, totalling up to 15 Ge detectors. The detector labelled T5Z2 in Fig. 3.3 (b), i.e. the second detector in the fifth tower, was operated in the CDMSlite mode during the DM search run. The DM search data was taken for a total of 279 days with this CDMSlite detector from February, 2014 to December, 2014 with a break in August, 2014.

4.2.3 Data selection criteria and signal efficiency

Data selection criteria

Several event selection cuts were applied on the data to remove spurious events to improve data quality. The cuts were directly adopted from the CDMSlite dark matter search analysis. The cuts can be broadly divided into two categories like in Chapter 3, (i) basic cuts and, (ii) quality cuts. The basic cuts ensure a consistency in the run conditions and are applied directly on the value of a related variable after the data is processed. The basic cuts include bias flashtime, base temperature, voltage bias, leakage current, bad series, and a prepulse

baseline standard deviation. These cuts serve the same purpose as those described in Sec. 3.3.1. Quality cuts require further analysis and optimization techniques to improve data quality. The quality cut comprise of the phonon OF χ^2, charge OF χ^2, glitch, $\delta\chi^2$ LFN, and a phonon radial cut. These cuts serve the same purpose and follow similar optimization techniques as those described in Sec. 3.3.2. Since there is a large overlap between the cuts used in this analysis and those described in Chapter 3, the cut descriptions have been limited to only those which are unique to this analysis. The detailed description of the cuts developed for the CDMSlite DM search analysis can also be found in Ref [17, 18]. There is only one additional cut, the phonon radial cut, that is unique of this analysis compared to the photo-neutron data analysis. The phonon radial cut has been described below.
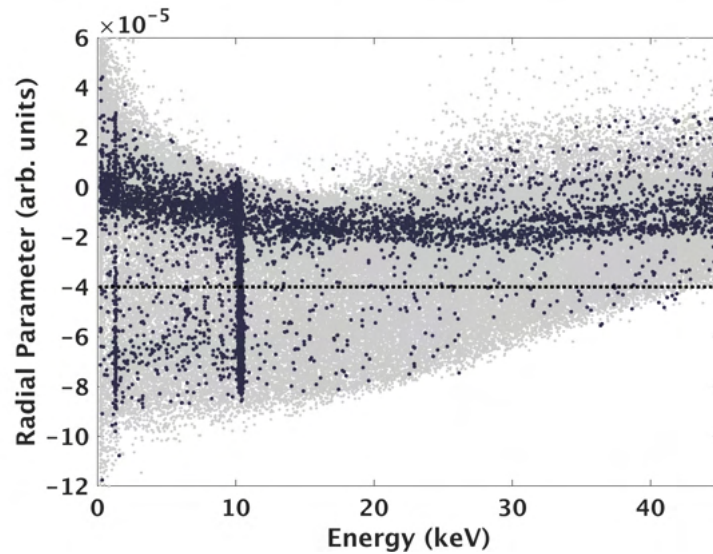
FIGURE 4.4: The radial parameter as a function of recoil energy. The dashed line shows the selection criteria for discarding radially outward events. Negative values of the radial parameter indicate inner events [19]

Phonon radial cut: Ideally the electric field should be uniform within the detector. However in practice, due to fringe effects caused by the proximity to copper housing, the

electric field lines are non-uniform at the outer edges of the detector. The phonon energy gain achieved through the Neganov-Trofimov-Luke [20, 21] effect would be different at the outer edges of the detector when compared to the bulk, thus distorting the total phonon energy distribution. The fringe effect and how exactly it changes the electric field lines is not fully understood. Hence events occurring at the outer edges of the detector are removed from the analysis. This is done by first defining a radial parameter which gives the radial position of an event with the center of the detector as the origin. The radial parameter was constructed by the CDMSlite dark matter search analysis group, and the method for obtaining it is beyond the scope of this thesis. A detailed explanation of the radial parameter can be found in Ref. [18]. Figure 4.4 shows the radial parameter as a function of energy. The region below the dashed line represent inner events. All events above the dashed lines are removed.

4.2.4 Signal efficiency

The trigger efficiency and the analysis cut efficiency are calculated using the method described in Sec. 3.3.1 and Sec. 3.3.3. The combined trigger and analysis cut efficiency as a function of energy is shown in Fig. 4.5. The signal efficiency is roughly around 50% in the analysis region of interest i.e. for recoil energies below 20 keV. The biggest contributor towards the reduction of the signal efficiency comes from the phonon radial cut.

4.2.5 Background model

The CDMSlite energy distribution from the dark matter search data is expected to have the following background components, (i) ^{3}H beta decay, (ii) Compton steps, and (iii) EC peaks from various isotopes in Ge. The method for modeling each of these components is discussed below

Tritium beta decay

From the Fermi theory of beta decay, the tritium beta decay function is given by,

$$N(T_e) = C\sqrt{T_e^2 + 2T_e m_e c^2}(Q - T_e)^2(T_e + m_e c^2)F(Z, T_e), \tag{4.1}$$

where C is a normalization constant, T_e is the kinetic energy of the emitted beta particle i.e electron, m_e is the mass of an electron, c is the speed of light, Q is the end point energy (18.6 keV), $F(Z, T_e)$ is the relativistic Fermi function, and Z is the atomic number of the daughter nuclei. The relativistic Fermi function is given by,

$$F(Z, T_e) = \frac{2\pi\eta}{1 - e^{-2\pi\eta}}, \tag{4.2}$$

where $\eta = \alpha Z \frac{c}{v}$. Here α is the fine structure constant, and v is the velocity of the
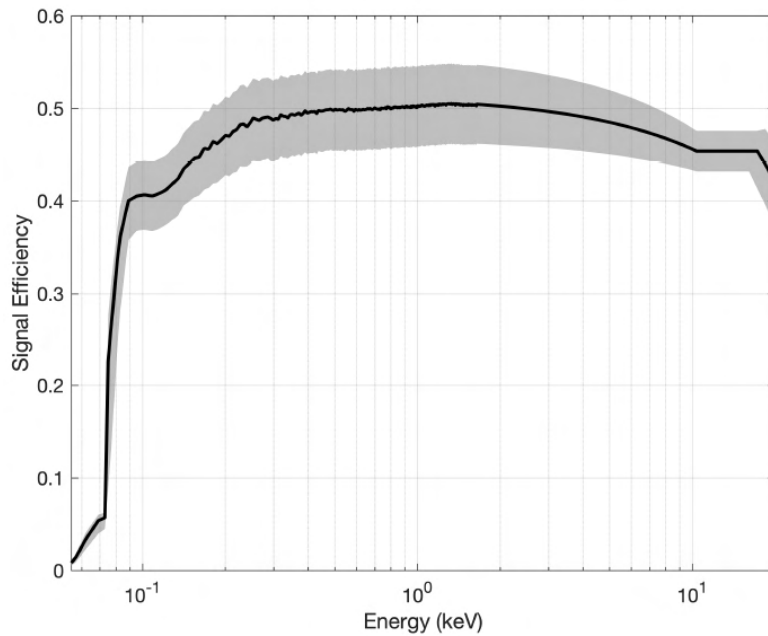
FIGURE 4.5: The signal efficiency as a function of energy. The 1σ uncertainty on the efficiency is shown by the shaded region [19].

electron. Figure 4.6 shows the PDF of the ^{3}H beta decay spectrum.

Compton background

The Compton steps appear at the K, L, and M shell binding energies in Ge as fewer electrons are available for the scattering process. The Compton steps are modeled using the method described by Eq. 3.17 in Sec. 3.5.2. The PDF of the Compton model is shown in Fig. 4.6.

Electron capture peak

The EC peaks for K, L and M shells in Ge by various radioactive isotopes present in it are modelled as Gaussian functions. The detector energy resolution at the central values of the EC peaks are set as the standard deviation of these Gaussians. The detector resolution is determined by the model described in Sec. 3.5.1. The relative amplitudes of the peaks between the K, L and M shells are set according to their branching ratios. Table 4.1 documents the central peak energy values of the K, L and M shells of all the radioactive
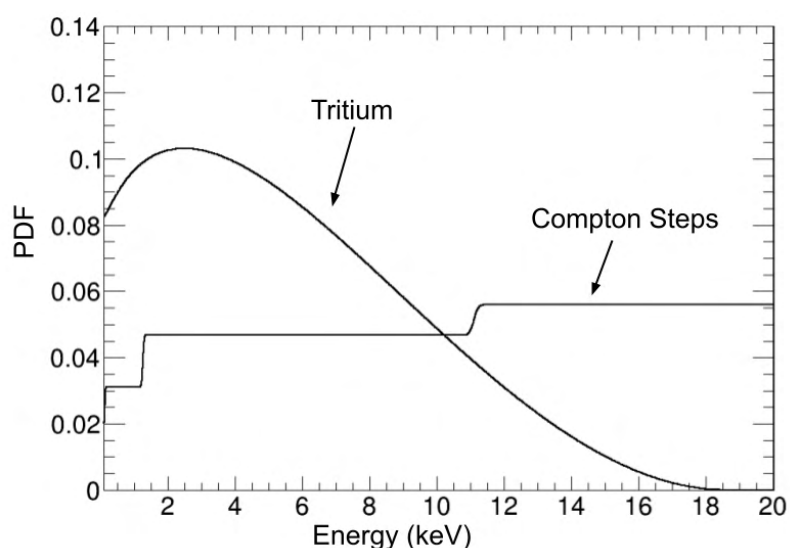
FIGURE 4.6: A PDF of the ^{3}H beta decay and the Compton step model.

isotopes expected to decay via the EC process. The table also provides the detector energy

resolution at the peak values and their branching ratios.

TABLE 4.1: A list of all the radioactive isotopes which decay via electron capture in Ge. The central
value of the electron capture peak (K, L or M) energy for an isotope is given under
column E, the energy resolution of the detector at that central peak energy is given by
σ, and the branching ratios of the K, L and M shells are given under the column BR [17,
22]

Isotope	K			L			M		
	E (keV)	σ (eV)	BR	E (keV)	σ (eV)	BR	E (keV)	σ (eV)	BR
^{71}Ge	10.37	101	87.6 %	1.30	31.2	10.5 %	0.160	14.0	1.8 %
^{68}Ge	10.37	101	86.5 %	1.30	31.2	11.5 %	0.160	14.0	1.78 %
^{68}Ga	9.66	96.3	88.6 %	1.20	30.0	9.8 %	0.140	13.1	1.6 %
^{65}Zn	8.98	91.8	88.6 %	1.10	28.8	9.8 %	0.122	13.1	1.6 %
^{57}Co	7.11	79.2	88.8 %	0.84	25.5	9.6 %	0.091	12.3	1.5 %
^{55}Fe	6.54	75.2	88.6 %	0.77	24.4	9.8 %	0.082	12.1	1.6 %
^{54}Mn	5.99	71.3	89.6 %	0.70	23.4	9.0 %	0.066	11.7	1.4 %
^{49}V	4.97	63.7	89.3 %	0.56	21.3	9.3 %	0.059	11.5	1.4 %

The electron capture peaks for K, L and M shell from an isotope are modelled as,

$$f_E C(E) = \frac{P_K}{\sqrt{2\pi}\sigma_K} exp\left(-\frac{(E - E_K)^2}{2\sigma_K^2}\right) + \frac{P_L}{\sqrt{2\pi}\sigma_L} exp\left(-\frac{(E - E_L)^2}{2\sigma_L^2}\right)$$
$$+ \frac{P_M}{\sqrt{2\pi}\sigma_M} exp\left(-\frac{(E - E_M)^2}{2\sigma_M^2}\right),$$

(4.3)

where P_X is the probability an EC from the X-shell, σ_X is the detector's energy

resolution at E_X. The values of E_X, σ_X, and P_X can be found in Table 4.1.

4.2.6 Likelihood method

The energy dependent signal efficiency shown in Fig. 4.5 is applied to the PDFs. A negative log likelihood (NLL) method is used to determine the number of events that each background source contributes to the total energy distribution. The NLL method is given as [23],

$$-\ln \mathcal{L} = \sum_b n_b - \sum_{i=1}^{N} \ln(\sum_b n_b f_b(E_i)), \tag{4.4}$$

where n_b is the number of events that each background contributes to the total energy distribution, $f_b(E_i)$ are the PDFs of each background source. The best fit value of n_b when the likelihood function is minimized is taken as the number of events from that background source. The results of the likelihood fit are shown in Fig 4.7.
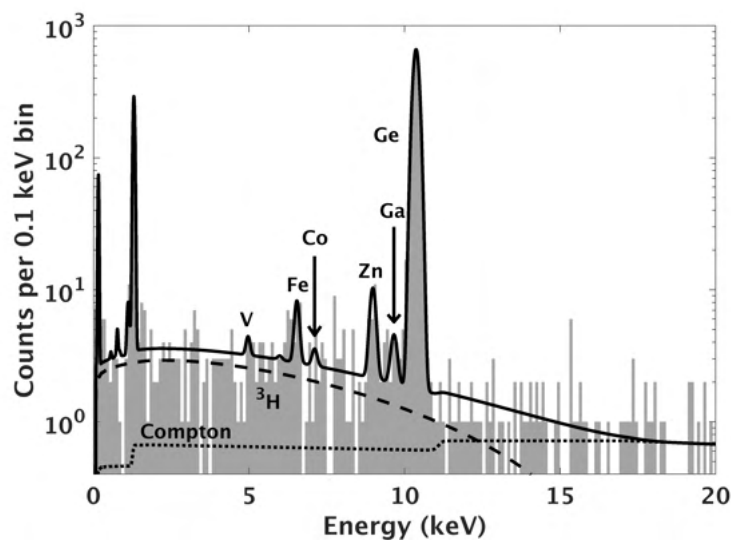
FIGURE 4.7: The best fit result for each background source to the CDMSlite energy distribution using the negative log likelihood method. The dashed line shows the ^{3}H PDF fit result using NLL. The dotted line shows the best fit for the compton steps. The solid line shows the best fit PDF for all the EC peaks in Ge [19].

The uncertainty on the number of events is obtained via a Monte Carlo method. For a

given background, the maximum likelihood is calculated by keeping its number of events constant while allowing values of the remaining backgrounds to float. This process is performed over a large range of values for the fixed background. This results in a PDF of the likelihood as a function of the number of events for a given background. The PDF can be converted into a cumulative distribution function (CDF). From the CDF, the confidence intervals are found. The uncertainty is taken at the 68% confidence level. Table 4.2 shows the results of the likelihood fits along with their uncertainties. It can be seen that the lower limit on the confidence intervals of ^{58,57,56}Co, ^{54}Mn and ^{49}V give negative values. Hence their presence in the CDMSlite data can be considered as zero.

TABLE 4.2: The best fit values of the number of events contributing to the measured CDMSlite energy distribution by each background component as determined by the NLL fit. The lower limit (LL) and the upper limit (UL) are for 68%, 90%, and 95% confidence level (CL) are shown. The negative lower limits on the confidence intervals for the isotopes in the last three rows indicate their absence in the CDMSlite data.

Component	# Events	Uncertainty Range					
		95 % CL		90 % CL		68 % CL	
		LL	UL	LL	UL	LL	UL
^{68,71}Ge	1932	1893	1967	1899	1962	1912	1949
^{68}Ga	7.2	0.9	18.0	1.8	16.1	3.9	12.6
^{65}Zn	21.5	11.9	35.1	13.4	32.8	16.6	28.3
^{55}Fe	11.5	3.8	23.6	5.0	21.6	7.7	17.7
^{3}H	270	222	318	230	310	245	294
Compton	131	95	175	101	168	113	153
^{58,57,56}Co	2.0	−2.7	11.2	−2.0	9.6	−0.3	6.7
^{54}Mn	0.4	−3.7	9.2	−3.1	7.7	−1.7	4.9
^{49}V	2.2	−2.2	10.7	−1.5	9.2	0.2	6.5
Total	2378						

4.2.7 Production rates of the contaminants

From the NLL estimates, the number of events that a background contributes to the CDMSlite energy distribution is determined. The production rate is given in units of atoms/(kg·day). To convert from the number of events to units of atoms/(kg·day) is a two step process. In the first step, the number of events are converted to the total number of decays. From Fig. 4.5, we see that the signal efficiency is at ∼ 50%. The best fit results from NLL must be corrected to represent the total number of decays that occurred during the CDMSlite run. For this purpose, an appropriate efficiency factor, R_{eff}, which is the inverse of the signal efficiency is multiplied to the best fit result from NLL for each background. Furthermore, not all decay modes of a given radioactive isotope are considered in the NLL fit. Hence the branching ratio of the decay mode considered in the NLL (BR_{XNLL}) has to be factored in to determine the total number of decays. If N_X is the total number of decays by an element X, then it can be calculated from the best fit value of N_{XNLL} from the NLL as,

$$N_X = \frac{N_{XNLL} \cdot R_{eff}}{BR_{XNLL}} \tag{4.5}$$

The next step is to convert the total number of decays to atoms/(kg·day). At any given time t (in days), the number of atoms of a given radioactive isotope in the detector is $N_0 e^{-\lambda t}$. Here N_0 is the number of atoms at the start of the CDMSlite run, and λ is the decay constant of that isotope. The exposure of the CDMSlite run is known i.e. the mass of the active detectors times the effective livetime of the run. Then dividing the number of atoms at the start of the run by the exposure gives the production rate of the isotope in atoms/(kg·day). Table 4.3 gives the production rates of each of the isotopes at the start of the run based on their NLL best fit values. The half life of ^{67}Ga is only 68 mins. Also

its branching ratio for an EC process is very low [13]. Its production rate in Ge is hence almost zero and excluded from the results shown in Table 4.3.

TABLE 4.3: Production rates at the start of the CDMSlite run and 1σ uncertainties i.e. at 68% confidence interval from the NLL for different isotopes in nat Ge.

Isotope	Cosmogenic Production Rate [atoms/(kg·day)]
^{3}H	74 ± 9
^{55}Fe	1.5 ± 0.7
^{65}Zn	17 ± 5
^{68}Ge	30 ± 18

4.3 Summary and conclusion

The major backgrounds in any underground direct LMDM search experiments that make use of Si detectors are ^{32}Si and ^{3}H, and ^{3}H for Ge semiconductor detectors. These background sources are created by cosmogenic activatation and are an inherent impurity in the detector material. Very little experimental measurements exist on these backgrounds. The sensitivity of a LMDM search experiment is affected by the understanding of the backgrounds. The better an experiment can exclude a background, either through shielding or through analysis techniques, the more sensitive it becomes to detecting a DM. SuperCDMS has made a measurement of the ^{3}H production rate in its Ge detectors from the CDMSlite data. The results reported are 74 ± 9 atoms/(kg·day). This result is more precise than the previously existing value reported by EDELWIESS of 82 ± 21) atoms/(kg·day). Super-CDMS made use of Si detectors during its previous run between 2008-2012, which was called CDMS-II. There are plans of obtaining the ^{32}Si production rate from the CDMS-II dark matter search data with Si detectors [24]. As an outlook, SuperCDMS plans to

carry out analysis similar to the ^{3}H measurements shown in this chapter at the Cryogenic Underground Test Experiment (CUTE) at SNOLAB.

Bibliography

[1] P. A. Zyla et al. "Review of Particle Physics". *PTEP* 2020.8 (2020), p. 083C01.

[2] J.D. Lewin and P.F. Smith. "Review of mathematics, numerical factors, and corrections for dark matter experiments based on elastic nuclear recoil". *Astroparticle Physics* 6.1 (1996), pp. 87–112. ISSN: 0927-6505.

[3] R. Agnese et al. "Projected sensitivity of the SuperCDMS SNOLAB experiment". *Phys. Rev. D* 95 (8 Apr. 2017), p. 082002.

[4] D. Lal and B. Peters. "Cosmic Ray Produced Radioactivity on the Earth". In: *Kosmische Strahlung II / Cosmic Rays II*. Ed. by K. Sitte. Berlin, Heidelberg: Springer Berlin Heidelberg, 1967, pp. 551–612. ISBN: 978-3-642-46079-1.

[5] W. Z Wei, D. M Mei, and C. Zhang. "Cosmogenic Activation of Germanium Used for Tonne-Scale Rare Event Search Experiments". *Astropart. Phys.* 96 (2017), pp. 24–31. arXiv: 1706.05324 [nucl-ex].

[6] John L. Orrell et al. "Naturally occurring ^{32}Si and low-background silicon dark matter detectors". *Astropart. Phys.* 99 (2018), pp. 9–20. arXiv: 1708.00110 [physics.ins-det].

[7] Christian Ouellet and Balraj Singh. "Nuclear Data Sheets for A = 32". *Nucl. Data Sheets* 112 (2011), pp. 2199–2355.

[8] W.C. Butterman and U.S. Geological Survey John D. Jorgenson. *Mineral Commodity Profiles: Germanium*. https://pubs.usgs.gov/of/2004/1218/2004-1218.pdf.

[9] M. B. Chadwick et al. "ENDF/B-VII.1 Nuclear Data for Science and Technology: Cross Sections, Covariances, Fission Product Yields and Decay Data". *Nucl. Data Sheets* 112.12 (2011), pp. 2887–2996.

[10] C. E. Aalseth et al. "Results from a Search for Light-Mass Dark Matter with a P-type Point Contact Germanium Detector". *Phys. Rev. Lett.* 106 (2011), p. 131301. arXiv: 1002.4703 [astro-ph.CO].

[11] Daniel Z. Freedman. "Coherent Effects of a Weak Neutral Current". *Phys. Rev. D* 9 (1974), pp. 1389–1392.

[12] A. Aguilar-Arevalo et al. "Measurement of radioactive contamination in the high-resistivity silicon CCDs of the DAMIC experiment". *JINST* 10.08 (2015), P08014. arXiv: 1506.02562 [astro-ph.IM].

[13] E. Armengaud et al. "Measurement of the cosmogenic activation of germanium detectors in EDELWEISS-III". *Astropart. Phys.* 91 (2017), pp. 51–64. arXiv: 1607.04560 [astro-ph.CO].

[14] J. L. Ma et al. "Study on cosmogenic activation in germanium detectors for future tonne-scale CDEX experiment". *Sci. China Phys. Mech. Astron.* 62.1 (2019), p. 11011. arXiv: 1802.09327 [physics.ins-det].

[15] F. T. Avignone et al. "Theoretical and experimental investigation of cosmogenic radioisotope production in germanium". *Nucl. Phys. B Proc. Suppl.* 28 (1992). Ed. by A. Morales, J. Morales, and J. A. Villar, pp. 280–285.

[16] Grayson C. Rich. *Status and plans for the DAMIC Experiment at SNOLAB and Modane*. https://indico.cern.ch/event/699961/contributions/3043431/attachments/1694413/2726984/2018-07-27_G.C.Rich_damic.pdf.

[17] R. Agnese et al. "Low-mass dark matter search with CDMSlite". *Phys. Rev. D* 97 (2 Jan. 2018), p. 022002.

[18] Mark David Pepin. "Low-Mass Dark Matter Search Results and Radiogenic Backgrounds for the Cryogenic Dark Matter Search". PhD thesis. Minnesota U., 2016.

[19] R. Agnese et al. "Production rate measurement of Tritium and other cosmogenic isotopes in Germanium with CDMSlite". *Astroparticle Physics* 104 (2019), pp. 1–12. ISSN: 0927-6505.

[20] B.S. Neganov et al. "Application of ionization to heat conversion to the light absorption spectra measurement in silicon at 1 K through adiabatic calorimetry". *J Low Temp Phys* 93 (1993), pp. 417–422.

[21] P.N. Luke et al. "Calorimetric ionization detector". *Nucl. Instrum. Meth. A* 289 (1990), pp. 406–409.

[22] E. Schönfeld. "Calculation of fractional electron capture probabilities". *Applied Radiation and Isotopes* 49.9 (1998), pp. 1353 –1357. ISSN: 0969-8043.

[23] Philip R. Bevington and D. Keith Robinson. *Data reduction and error analysis for the physical sciences*. 2003.

[24] Rik Bhattacharyya. "Si-32 and P-32 Background Estimate in CDMS II Silicon Detectors". In: *XXIII DAE High Energy Physics Symposium*. Ed. by Prafulla Kumar Behera et al. Singapore: Springer Singapore, 2021, pp. 827–831. ISBN: 978-981-33-4408-2.

Chapter 5

Conclusion and outlook

The identity of dark matter (DM), is one of the biggest mysteries in physics. The motivation to search for low mass dark matter (LMDM) particles was discussed in Chapter 1. The work presented in this thesis covers three key aspects related to LMDM search experiments, (i) development of a semiconductor detector with low recoil energy threshold, (ii) ionization yield measurement at low recoil energies, and (iii) understanding important backgrounds in a LMDM experiment.

5.1 Development of a semiconductor detector for low mass dark matter searches

In this thesis, we learn that for LMDM searches, semiconductors, especially silicon, due to its light atomic mass number, is a popular choice of detector material. The main requirement to explore the DM nucleon cross section vs DM mass parameter space is

a large mass detector with low energy threshold and good energy resolution. Although experiments like DAMIC, and SuperCDMS have high energy resolution detectors that are capable of single electron measurements, they are limited to very small mass detector modules (< 10 g). In this thesis, results were presented from a 100 g phonon-mediated Si detector with a novel contact free interface between the semiconductor detector and metal electrode on one side. The contact free interface delayed the onset of the leakage current contribution to the noise with bias voltage. The effect of the leakage current on the signal to noise (S/N) can be observed beyond 240 V bias voltage. The linearity in the phonon signal gain due to the Neganov-Trofimov-Luke (NTL) effect was also seen up to 240 V. The lowest baseline resolution achieved with this detector is of $\sim 1e^-/h^+$ pair at 240 V. The ability to bias the detector up to 240 V before seeing any degradation in the S/N is an improvement over previous detectors of similar mass and dimensions, like the SuperCDMS/CDMS-II Soudan Ge and Si detectors, that showed breakdown at voltages beyond 75 V. The leakage current in this detector is on the order of 10^{-16} A which is an order of magnitude better to previous Ge prototypes of this contact free design. The leakage current is also a few orders lower than previous CDMS detectors made of Si.

The improved S/N enables the detector to operate at a low energy threshold which is beneficial for LMDM searches. The detector is also an ideal candidate to measure coherent elastic neutrino nucleus scattering (CEνNS). This detector is already in use at the Mitchell Institute Neutrino Experiment at Reactor (MINER) at Texas A&M, USA to measure CEνNS from reactor neutrinos. With advancements in detector technology, alternative direct DM search methods, like detection of MeV scale LMDM signals due to inelastic scattering with electrons in the detector medium are being proposed. As the quantum excitation (i.e. band gap energy) in silicon detectors are very small (~ 1.12 eV), and with a baseline resolution of ~ 1 eV, this detector would also be sensitive to detect signals from LMDM particles

interacting directly with the valence electrons. Sensitivity to single e^-/h^+ pair excitation offers the unique opportunity for experiments to discriminate backgrounds in directional DM searches.

5.2 Ionization yield measurement at low recoil energies

In this thesis we understand that for semiconductor detectors, any uncertainty in the ionization yield of the detector gets propagated to the uncertainty in the recoil energy measured by the detector. This in turn affects the uncertainty in the limit curve for an experiment in the DM-nucleon cross section vs DM mass parameter space. Detectors that exploit the NTL effect cannot directly measure the ionization yield on an event by event basis. In such circumstances, an ionization yield model is used. The most widely used yield model is given by Lindhard et. al.. However this model is known to have limited accuracy at low recoil energies. Additionally the model does not consider the effect of temperature on the ionization yield in a material. The work presented in this thesis is related to the measurement of ionization yield at low recoil energies in the germanium SuperCDMS detectors that were operated at temperatures < 55 mK in the CDMSlite mode. The study involved measuring the recoil energy distribution from photo-neutrons of known energy, and using a likelihood analysis to obtain the ionization yield of the SuperCDMS germanium detectors. The yield model used in this study is a modified Lindhard model with the k parameter considered as a linear combination of two components, k_{low} and k_{high}, with a dependence on recoil energy. The likelihood analysis return a best fit value of $k_{\text{low}} = 0.040 \pm 0.013$ and $k_{\text{high}} = 0.142 \pm 0.029$. The results from this study showed deviations from the ionization yield predicted by the standard Lindhard model. The ionization yield obtained for in Ge CDMSlite detector goes from 0.06 to 0.19 between recoil energies of 1 keV and 7 keV.

Previously, SuperCDMS would calculate the uncertainty related to ionization yield in their results by computing it using the classic single k parameter Lindhard model, with k=0.1 to get the lower limit, and then with k=0.2 to get the upper limit on the uncertainty in yield. The 2-k parameter yield model adopted in this work in place of the single k parameter Lindhard model, and the reduced uncertainties on the k parameters will be useful in reducing the uncertainty in SuperCDMS SNOLAB results arising from the ionization yield.

There is a study that showed the Fano factor (i.e. the term associated with the variation in the number of e^-/h^+ pairs produced for a given incident photon energy) for nuclear recoils could be significantly higher than that for electron recoils. Apart from the CDMSlite mode, SuperCDMS also took photo-neutron data in the iZIP mode. There are plans to analyze the iZIP photo-neutron data to document the differences in Fano factors between electron recoils and nuclear recoils. SuperCDMS also plans on doing more dedicated ionization yield measurement runs at Fermilab with the silicon and germanium high voltage detectors. The experiment will use a deuteron-deuteron generator as a neutron source. The neutrons will elastically scatter of the detector. An array of neutron detectors around the SuperCDMS detector will help in obtaining the angle of neutron scatter. Through various data analysis techniques, the ionization yield for recoil energies as low as 100 eV can be obtained in Ge and Si detectors.

5.3   Understanding backgrounds for low mass dark matter search experiments

In this thesis, we learn that the background rate affects the total event rate in an direct DM search experiment, which in turn affects any limit calculated on the DM-nucleon cross section for a given DM mass. Understanding the backgrounds in a direct DM search

experiment is important as lower the background rate, more sensitive the experiment can be to a DM particle. In this thesis, the beta-decay backgrounds from cosmogenically activated isotopes of ^{3}H, ^{55}Fe, ^{65}Zn and ^{68}Ge in the SuperCDMS germanium detectors are discussed. The production rate in atoms/(kg·day) from the CDMSlite data was deduced to be 74 ± 9 for ^{3}H, 1.5 ± 0.7 for ^{55}Fe, 17 ± 5 for ^{65}Zn, and 30 ± 18 for ^{68}Ge using a likelihood analysis. Tritium is expected to be a major background for the SuperCDMS experiment at SNOLAB. The ^{3}H production rate reported in this work of 74 ± 9 atoms/(kg·day) is lower and more precise than the most recent measurement available by EDELWEISS with a production rate of 82 ±21 atoms/(kg·day). The production rate of the remaining isotopes in germanium, i.e. ^{55}Fe, ^{65}Zn and ^{68}Ge are also lower than those measured previously. Another important background expected at SNOLAB by SuperCDMS in their silicon detectors is from ^{32}Si which settles in at the time of silicon extraction. The ^{32}Si beta decays into ^{32}P before finding stability as ^{32}S. At present SuperCDMS uses the concentration of ^{32}Si in their detectors as 80^{+100}_{-65} decays/kg·day based on a measurement by DAMIC for calculations related to obtaining DM sensitivity in their experiment. The large uncertainty on this measurement by DAMIC, and coupled with a lack of measurements on this background by any other experiment, makes it important to have a dedicated study of the ^{32}Si concentration level for SuperCDMS in their silicon detectors. Work is ongoing to deduce the production rates of ^{32}Si and ^{32}P from the CDMS-II data that used silicon detectors. There are future plans of performing similar measurements of ^{3}H and ^{32}Si backgrounds in SuperCDMS HV detectors (germanium and silicon) at the Cryogenic Underground Test Experiment (CUTE) in SNOLAB.

Figure 5.1 highlights the potential of the new contact free Si HV detector for LMDM searches. The figure compares the sensitivity curves for the SuperCDMS SNOLAB Si HV detector, and the contact free Si HV detector. The curves were made assuming the
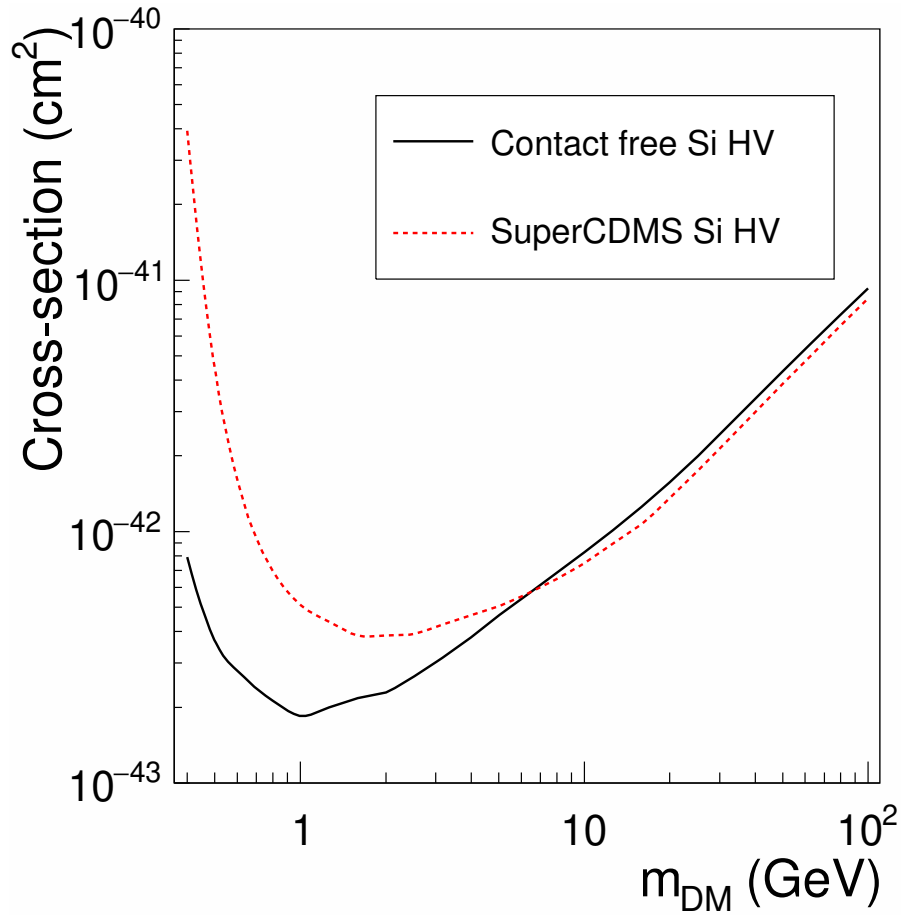
FIGURE 5.1: A comparison of the sensitivity curves between the SuperCDMS SNOLAB Si HV
detectors (red dashed line), and the contact free Si HV detectors (solid black line)
discussed in this thesis. The curves were made assuming the ^{3}H contamination levels
discussed in this thesis.

^{3}H contamination level reported in this thesis, and a similar payload, at the SuperCDMS

SNOLAB experiment site. The lower energy threshold achieved by improving the S/N in

the contact free Si HV detector provides better sensitivity to LMDM. The SuperCDMS

SNOLAB Si HV detector has a larger fiducial volume than the contact free Si HV detector,

resulting in a difference between the two curves above DM masses of 10 GeV.

Appendix A

Relationship between nuclear recoil energy and dark matter mass
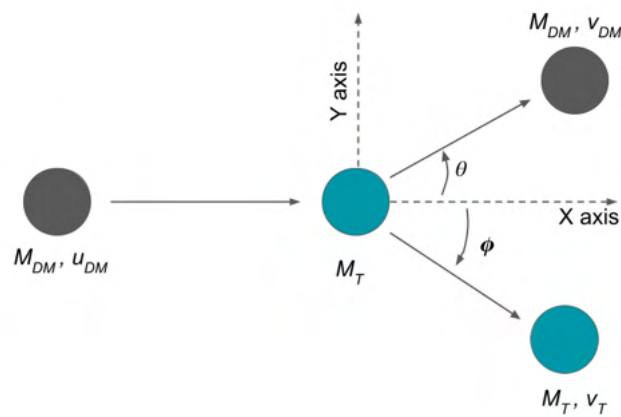

FIGURE A.1: A schematic showing the kinematic of the elastic scatterting process between a dark matter particle and a target nucleus.

Consider a dark matter (DM) particle elastically scatterting of the nucleus of a material which is taken to be at rest. Let the mass of the DM be M_{DM}, mass of the target nucleus be

M_T, velocity of the DM particle before collision be u_{DM}, velocity of DM after collision be v_{DM}, and the velocity of the target nucleus after collision be v_T. As seen in the schematic shown in Fig. A.1, the angle by which the DM scatters with respect to the X axis is taken as θ, and the angle by which the nucleus recoils is taken to be ϕ.

Applying conservation of momentum along X and Y axis we get,

$$M_{DM}u_{DM} - M_T v_T \cos\phi = M_{DM}v_{DM}\cos\theta, \tag{A.1}$$

$$M_T v_T \sin\phi = M_{DM}v_{DM}\sin\theta, \tag{A.2}$$

Squaring and adding Eq. A.1 and Eq. A.2, we get

$$M_{DM}^2 u_{DM}^2 + M_T^2 v_T^2 - 2M_{DM}u_{DM}M_T v_T \cos\phi = M_{DM}^2 v_{DM}^2 \tag{A.3}$$

Using conservation of energy, we get,

$$\frac{1}{2}M_{DM}u_{DM}^2 = \frac{1}{2}M_{DM}v_{DM}^2 + \frac{1}{2}M_T v_T^2 \tag{A.4}$$

Multiplying Eq. A.4 by M_{DM}, then substituting the LHS with the first term in Eq. A.3 and rearranging, we get,

$$\frac{v_T^2}{u_{DM}^2} = \frac{4M_{DM}^2 \cos^2\phi}{(M_T + M_{DM})^2} \tag{A.5}$$

Energy transfer (ϵ) from the incident DM particle to the recoiling target nucleus can be written as :

$$\epsilon = \frac{\text{K.E. of target nucleus after collision}}{\text{K.E. of incident DM particle}} = \frac{\frac{1}{2}M_T v_T^2}{\frac{1}{2}M_{DM}u_{DM}^2} \tag{A.6}$$

Now the K.E. of the target nucleus after collision is also the nuclear recoil energy $E_R = M_T v_T^2$ i.e. numerator of Eq. A.6. Multiplying Eq. A.5 by (M_T/M_{DM}) and substituting in Eq. A.6, we get,

$$E_R = \frac{2M_{DM}^2 M_T u_{DM}^2 \cos\phi}{(M_T + M_{DM})^2} = \frac{2M_{DM}^2 u_{DM}^2 \cos\phi}{M_T \left(1 + \frac{M_{DM}}{M_T}\right)^2} \tag{A.7}$$

Using Taylor series expansion for the denominator,

$$\begin{aligned} E_R &= \frac{2M_{DM}^2 u_{DM}^2 \cos\phi}{M_T} \left(1 - \frac{2M_{DM}}{M_T}\right) \\ &= \frac{2M_{DM}^2 u_{DM}^2 \cos\phi}{M_T} - \frac{4M_{DM}^3 u_{DM}^2 \cos\phi}{M_T^2} \end{aligned} \tag{A.8}$$

If $M_{DM} << M_T$ which is assumption we make for low mass dark matter, then we can neglect the second term in Eq. A.8. Thus,

$$E_R = \frac{2M_{DM}^2 u_{DM}^2 \cos\phi}{M_T} \tag{A.9}$$

From Eq. A.9 we can see that for $M_{DM} << M_T$, $E_R \propto M_{DM}^2$, and $E_R \propto 1/M_T$.

Appendix B

Optimal Filter

The optimal filter (OF) is a fitting method used to determine the amplitude of a signal with the help of a pulse template and a noise power spectral density (PSD). The advantage of using the OF fit is when trying to determine the amplitude of a noisy signal. The OF fit maximizes the signal to noise (S/N) by transforming the signal from a time domain to frequency domain. The noisy parts of the signal are then distinguished from the underlying true signal and the fitting is performed in this region. A brief summary of the OF fit method is given below.

Consider a signal $S(t)$ composed of two components, a pulse template $A(t)$ and Gaussian noise $n(t)$. The signal can be written as,

$$S(t) = aA(t) + n(t), \tag{B.1}$$

here a is the factor by which the template is scaled to obtain the pulse amplitude. The goal is to find the best fit value of a. Using Fourier transformations, one can convert the

signal and its components to frequency space giving us $\tilde{S}(v)$, $\tilde{A}(v)$, and $\tilde{n}(v)$. The term $\tilde{n}(v)$ is the PSD of the noise. In case of Gaussian noise, the PSD evaluates to its variance σ^2. The χ^2 of the pulse template fit to the signal in this frequency domain is given by [1],

$$\chi^2 = \int_{-\infty}^{\infty} \frac{\left| \tilde{S}(v) - a\tilde{A}(v) \right|^2}{\tilde{n}(v)} dv \tag{B.2}$$

The χ^2 is then minimized and the best fit value of a is obtained. It is possible for the start time of the pulse in the signal trace to be different from the start time of the template. In such cases an additional delay term t_0 is included such that the signal is defined as $S(t) = aA(t - t_0) + n(t)$. The delay is then determined by the same χ^2 minimization procedure described above. The method described here is the most basic OF fit. However it is also possible to have OF fits with multiple pulse templates. A detailed description of these fitting procedures can be found in [2, 3].

Bibliography

[1] Philip R. Bevington and D. Keith Robinson. *Data reduction and error analysis for the physical sciences*. 2003.

[2] Ritoban Basu Thakur. "The Cryogenic Dark Matter Search low ionization-threshold experiment". PhD thesis. Illinois U., Chicago, 2014.

[3] Sunil Ramanlal Golwala. "Exclusion limits on the WIMP nucleon elastic scattering cross-section from the Cryogenic Dark Matter Search". PhD thesis. Jan. 2000.

Appendix C

Supplementary Figures

Supplementary figures are provided below related to the discussions in Sec. 2.3.5 and Sec. 2.3.6. Figure C.1 shows the laser energy distribution at all bias voltages. The X-axis scale is in units of OF amplitude units. The uncertainty on the mean can be taken as the standard error. The values of the means and their corresponding errors are used in Fig. 2.13 in Sec. 2.3.5. Figure C.2 shows the noise energy distribution in units of e^-/h^+ pairs at all bias voltages. The Gaussian fit to the noise energy distribution is the baseline resolution of the detector at that voltage. The values of these baseline resolutions are used in Fig. 2.14 in Sec. 2.3.6
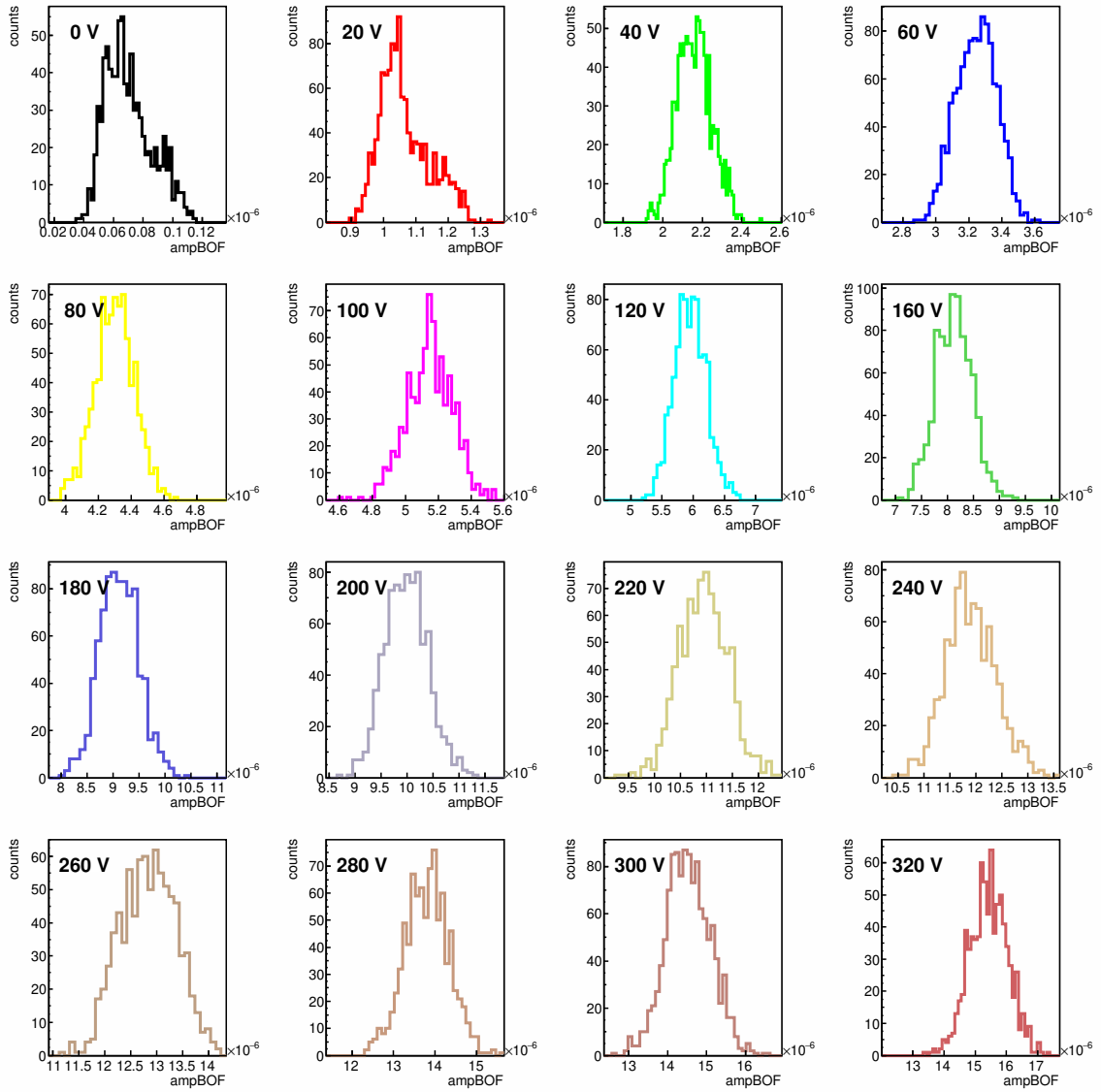
FIGURE C.1: The laser energy distribution in units of OF amplitude from 0 V to 320 V.
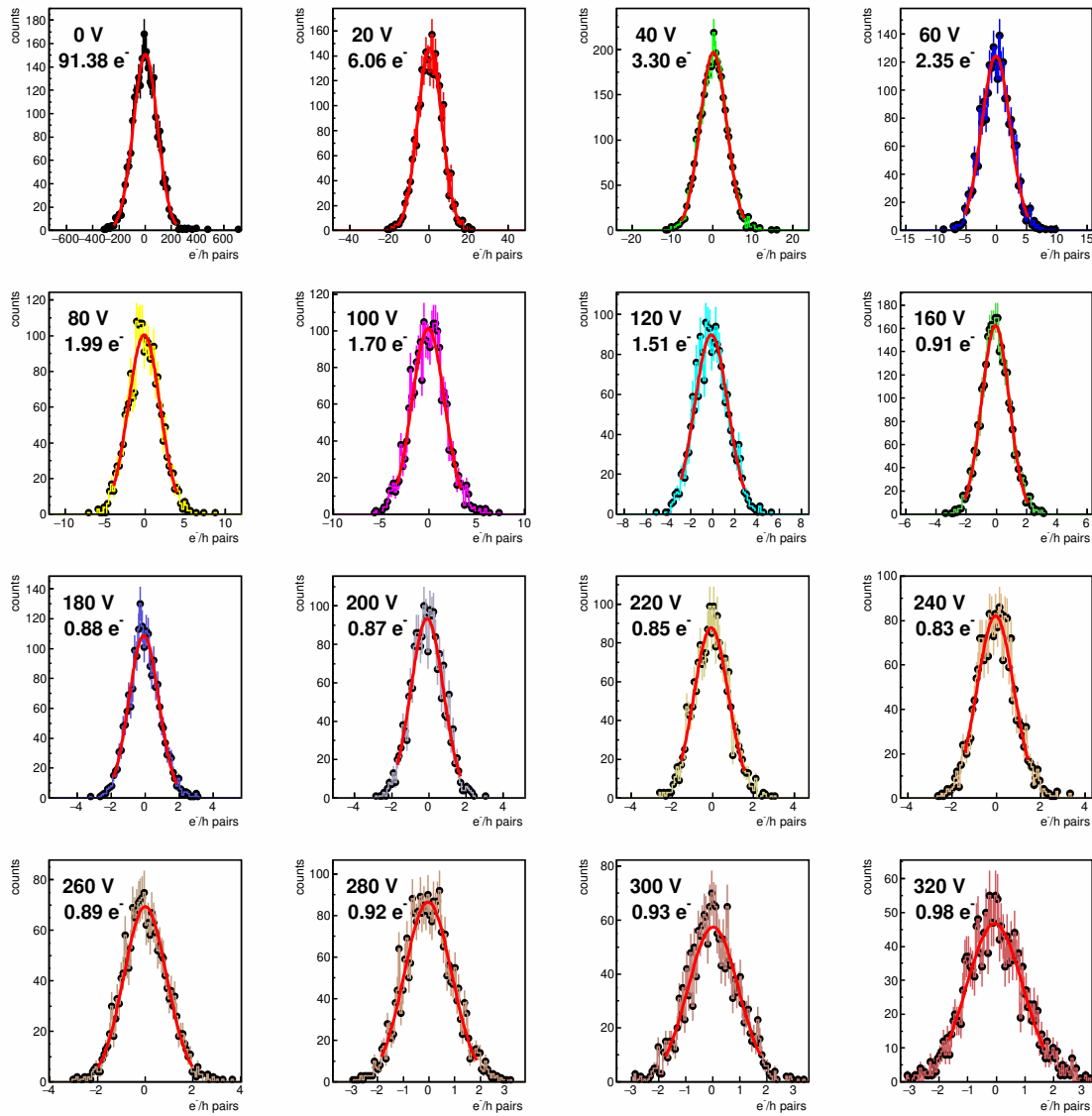
FIGURE C.2: The baseline resolution obtained by fitting a Gaussian (solid red line) to the noise energy distribution (black markers) in units of e⁻/h⁺ pairs from 0 V to 320 V.